The Electronic and Optical Properties of Magnetic Quantum Dots

A thesis submitted for the degree of

Doctor of Philosophy

at the University of Leicester

by

Gary Paul Mallon

Department of Physics and Astronomy

University of Leicester

December 1999

ProQuest LLC
789 East Eisenhower Parkway
P.O. Box 1346
Ann Arbor, MI 48106-1346

The Electronic and Optical Properties of Magnetic Quantum Dots

by

Gary Paul Mallon

Abstract

Advances in lithographic technology have made it possible to fabricate systems in which electrons are confined magnetically. With an inhomogeneous circularly symmetric magnetic field, B_z, that was modulated so as the magnetic field was zero in the centre, electrons could, theoretically, be confined to a disk region. These systems are referred to as magnetic quantum dots, and the purpose of this thesis is to investigate their properties.

The eigenstates of the single electron system are calculated using new methods based on wave function matching. These enable the eigenstates to be determined for all values of B_z. Exact numerical diagonalisation is used to calculate the N-electron eigenstates, and new procedures are derived to evaluate the Coulomb matrix elements. It is shown that a dot is able to confine interacting electrons, and is therefore stable. Numerical results for GaAs and InSb dots indicate the existence of a stability boundary as a function of the dot radius and B_z. The form of this boundary is investigated and an analytic expression for it is obtained. The stability of the system is enhanced in a homogeneous external magnetic field, B_{ext}. Results are also presented for the electron density, the pair distribution, and the pair correlation function.

The response of GaAs and InSb dots to far infrared radiation (FIR) is investigated as a function of B_z and B_{ext}. The FIR response of the one and two electron systems are dissimilar, and this is shown to be a consequence of the interaction. Results for an InSb system with two electrons show a large splitting of the spectrum. This is investigated and an explanation is given. As a function of B_{ext}, the single electron FIR response is similar to that of an electrostatic quantum dot in a magnetic field. The FIR spectrum of the equivalent two electron system is shown to have a rich structure, which should be experimentally verifiable.

Publication List

G. P. Mallon and P. A. Maksym, "*The Stability of Interacting Electrons in a Magnetic Quantum Dot*", *Physica B* **258** (1998) 186.

P. A. Maksym, H. Imamura, G. P. Mallon and H. Aoki, and , "*Molecular Aspects of Electron Correlation in Quantum Dots*", submitted to *J. Phys: Condensed Matter.*

Contents

List of Figures xii

Acknowledgements xiii

1 Introduction 1

1.1 Aims 4

1.2 Synopsis of the Thesis 5

2 Background 8

2.1 Magnetic Structures 9

2.2 Magnetic Quantum Dots 10

2.2.1 Fabrication Techniques 10

2.2.2 Magnetic Field Profile 13

2.2.3 Theoretical Model of a Magnetic Quantum Dot 18

2.3 Numerical Diagonalisation 21

3 Single Electron in a Magnetic Quantum Dot 24

3.1 A System without a Magnetic Field Overshoot 26

3.1.1 Calculation of the Single Electron Matrix Elements 26

3.1.2 Matching Procedure 28

3.1.3 Results 33

3.2 A System with a Magnetic Field Overshoot 38
3.2.1 Calculation of the Single Electron Matrix Elements 38
3.2.2 Matching Procedure 39
3.2.3 Results 43
3.3 Comparison of the Numerical Methods 47

4 Interacting Electrons in a Magnetic Quantum Dot 50
4.1 Previous Work 51
4.2 The Coulomb Matrix Elements 54
4.3 Confining Interacting Electrons in a Magnetic Quantum Dot . . . 60
4.4 Two Interacting Electrons in a Magnetic Quantum Dot 63
4.4.1 Determining the Stability of the System 64
4.4.2 Physics of Stability 68
4.4.3 Stability Results for a GaAs System 71
4.4.4 Stability Results for a InSb System 77
4.5 A System in an External Magnetic Field 80
4.5.1 Calculation of the Single Electron Matrix Elements 81
4.5.2 Results 82
4.6 Towards a More Realistic System 88
4.6.1 Theoretical Treatment 89
4.6.2 Calculation of the Single Electron Matrix Elements 91
4.6.3 Calculation of the Coulomb Matrix Elements 92
4.6.4 Determining the Variational Parameter, b 93
4.6.5 Results 95
4.6.6 Other Effects Expected in a More Realistic System 98
4.7 More Interacting Electrons 99

4.7.1 Results 100

5 Far Infrared Absorption Spectra **108**

5.1 Previous Work 109

5.2 The Generalised Kohn Theorem 111

5.3 Theoretical Treatment 113

5.4 FIR Response as a Function of the Confining Magnetic Field . . . 115

5.4.1 FIR Response of a GaAs Magnetic Quantum Dot 116

5.4.2 FIR Response of an InSb Magnetic Quantum Dot 120

5.5 FIR Response as a Function of an External Magnetic Field 125

5.5.1 FIR Response of an InSb Magnetic Quantum Dot 125

5.5.2 FIR Response of a GaAs Magnetic Quantum Dot 131

5.6 Scope for Future Experiments 134

6 Summary and Conclusions **137**

6.1 Future Work 143

A Calculation of the Coulomb Matrix Elements **145**

List of Figures

2.1 Schematic diagram of a proposed magnetic quantum dot structure fabricated using a ferromagnetic material (top) and a superconducting material (bottom). The vertical arrows indicate the location and direction of the intrinsic magnetic field (top) and the external magnetic field (bottom). 12

2.2 Schematic diagram of the magnetic field profile produced by a ferromagnetic strip (after Peeters [1]). The solid curve is for $z_o = 0.1d$ and the dashed curve is for $z_o = 0.3d$. 14

2.3 Schematic diagram of the magnetic field lines emanating from a ferromagnetic material. The solid horizontal lines indicate the position of the 2DEG, with a separation, z_o, between the 2DEG and ferromagnetic material. 15

2.4 Schematic diagram of a figure from Reijniers *et al* [10], showing the magnetic field profile produced by a superconducting (s/c) disk subject to an external magnetic field. The radius of the s/c disk is denoted by a and B_a is the external magnetic field. The inset shows a schematic diagram of the external magnetic field lines around the s/c disk close to a 2DEG (indicated by thick horizontal line). 16

2.5 Model magnetic field profiles and their corresponding vector potentials. . . . 17

3.1 Energy as a function of angular momentum quantum number, l, for magnetic field , $B_z = 5$ T and $r_o = 10$ nm. The diamonds indicate results calculated using the numerical diagonalisation technique and the crosses indicate results calculated using the matching procedure. 34

3.2 Electron density as a function of radial distance for $B_z = 5$ T, $r_o = 10$ nm, $l = 0$ (solid curve), $l = 1$ (short dashed curve) and $l = 2$ (long dashed curve). The vertical dotted line indicates the position of r_o. 35

3.3 Same as Fig. 3.1 but for a magnetic quantum dot of radius $r_o = 60$ nm. . . . 36

3.4 Energy as a function of magnetic quantum dot radius, r_o, for $B_z = 5$ T, $l = 0$ (solid curve), $l = 1$ (short dashed curve) and $l = 2$ (long dashed curve). . . . 37

3.5 Ratio, R, as a function of argument, y, for $a = -1.5$, $c = 5$ and $r_o = 10$ nm. . 43

3.6 Energy as a function of angular momentum quantum number, l, for magnetic field $B_z = 5$ T and $r_o = 35$ nm. The diamonds indicate results calculated using the numerical diagonalisation method and the crosses indicate results calculated using the matching procedure. 44

3.7 Electron density as a function of radial distance for $B_z = 5$ T, $r_o = 35$ nm, $l = 0$ (solid curve), $l = 3$ (short dashed curve) and $l = 10$ (long dashed curve). The vertical dotted line indicates the position of r_o. 45

3.8 Energy as a function of magnetic quantum dot radius, r_o, for $B_z = 5$ T, $l = 0$ (solid curve), $l = 1$ (short dashed curve) and $l = 2$ (long dashed curve). . . . 47

4.1 The number of Landau levels included in a two electron numerical diagonalisation calculation, as a function of the number of distinct Coulomb matrix elements that must be evaluated, for $J = 0$. The squares indicate results obtained from the numerical diagonalisation calculation and the solid curve is the result of a fit of this data to the expression $ax^4 + bx^3 + cx^2 + dx + e$. 58

4.2 Comparison of the confining potential in an electrostatic quantum dot (dashed curve) and the confining magnetic field in a magnetic quantum dot (solid curve). 61

4.3 A schematic diagram of the available electron configurations, for a magnetic quantum dot containing two interacting electrons. The shaded circles indicate the electrons. 62

4.4 Two electron energy as a function of angular momentum quantum number, for a spin unpolarised, GaAs system without a magnetic field overshoot at r_o (diamonds), and a spin polarised, GaAs system without a magnetic field overshoot at r_o (squares). The magnetic field is $B_z = 5$ T and the magnetic quantum dot radius is $r_o = 40$ nm. The solid lines are to guide the eye. . . . 65

4.5 Stability as a function of the system parameters for a GaAs magnetic quantum dot without a magnetic field overshoot at r_o. The solid curve is the result of a least squares fit to the data. 67

4.6 Stability as a function of the system parameters for a GaAs magnetic quantum dot with and without a magnetic field overshoot at r_o. The solid curves are the result of a least squares fit to the numerical data. 72

4.7 Electron density as a function of the radial distance for a GaAs magnetic quantum dot. The solid curve indicates the results obtained for a system with an overshoot, and the dashed curve indicates the results obtained a system without an overshoot at r_o. The system parameters are $B_z = 9.5$ T and $r_o = 30$ nm. 73

4.8 Pair distribution function as a function of the radial distance for a GaAs magnetic quantum dot. The solid curve indicates the results obtained for a system with an overshoot in the magnetic field at r_o, and the dashed curve indicates the results obtained for a system without a magnetic field overshoot at r_o. The confining magnetic field is $B_z = 9.5$ T and the magnetic quantum dot radius is $r_o = 30$ nm. 74

4.9 Pair correlation function for a GaAs magnetic quantum dot, with (bottom) and without (top) a magnetic field overshoot. The black spot indicates the position of the fixed electron. The confining magnetic field is $B_z = 9.5$ T and the magnetic quantum dot radius is $r_o = 30$ nm. 76

4.10 Stability as a function of the system parameters for a InSb magnetic quantum dot with and without a magnetic field overshoot at r_o. The solid curves are the result of a least squares fit to the numerical data. 78

4.11 Stability as a function of the system parameters for a GaAs magnetic quantum dot with and without an additional external magnetic field of $B_{\text{ext}} = 5$ T. The solid curves are the result of a least squares fit to the numerical data. 83

4.12 Electron density as a function of the radial distance for a GaAs magnetic quantum dot containing two interacting electrons. The solid curve indicates the results obtained for a system with an additional external magnetic field of $B_{\text{ext}} = 5$ T, and the dashed curve indicates the results obtained for a system without an additional external magnetic field. The confining magnetic field is $B_z = 7.5$ T and the magnetic quantum dot radius is $r_o = 30$ nm. 85

4.13 Pair distribution function as a function of the radial distance for a GaAs magnetic quantum dot. The solid curve indicates the results obtained for a system with an additional external magnetic field of $B_{ext} = 5$ T, and the dashed curve indicates the results obtained for a system without an additional external magnetic field. The confining magnetic field is $B_z = 7.5$ T and the magnetic quantum dot radius is $r_o = 30$ nm. 86

4.14 Pair correlation function for a GaAs magnetic quantum dot, with (top) and without (bottom) an additional external magnetic field of $B_{ext} = 5$ T. The black spot indicates the position of the fixed electron. The confining magnetic field is $B_z = 7.5$ T and the magnetic quantum dot radius is $r_o = 30$ nm. . . . 87

4.15 Energy as a function of the variational parameter, b. The solid curve shows the total energy as a function of b, while the dashed curve shows the total energy without the contribution due to the single electron energy perpendicular to the plane as a function of b. 94

4.16 Stability as a function of the system parameters for a GaAs system without a magnetic field overshoot at r_o, with an electron layer of finite thickness. The solid curve is the result of a least squares fit to the data. 95

4.17 Stability as a function of the system parameters for a GaAs magnetic quantum dot without a magnetic field overshoot at r_o, with and without an electron layer of finite thickness. 97

4.18 Electron density as a function of the radial distance for a GaAs magnetic quantum dot without overshoot containing three interacting electrons. The solid curve indicates the results obtained for an unstable system with $B_z = 10$ T and $r_o = 30$ nm, and the dashed curve indicates the results obtained for a stable system with $B_z = 10$ T and $r_o = 50$ nm. 103

4.19 Pair distribution function as a function of the radial distance for a GaAs magnetic quantum dot without overshoot containing three interacting electrons. The solid curve indicates the results obtained for an unstable system with $B_z = 10$ T and $r_o = 30$ nm, and the dashed curve indicates the results obtained for a stable system with $B_z = 10$ T and $r_o = 50$ nm. 104

4.20 Pair correlation function for a GaAs magnetic quantum dot with overshoot containing three interacting electrons. The top frame shows the pair correlation function for an unstable system with $B_z = 10$ T and $r_o = 30$ nm, and the bottom frame shows the pair correlation function for a stable system with $B_z = 10$ T and $r_o = 50$ nm. 106

5.1 Dipole allowed optical absorption energies and intensities of a GaAs magnetic quantum dot with $r_o = 40$ nm. The diameters of the filled circles are proportional to the calculated absorption intensities. 117

5.2 Dipole allowed optical absorption energies and intensities of an InSb magnetic quantum dot with $r_o = 40$ nm, containing one electron (upper frame), and two interacting electrons (lower frame). The diameters of the filled circles are proportional to the calculated absorption intensities. 121

5.3 Dipole allowed optical absorption energies and intensities of an Insb magnetic quantum dot with various r_o. The diameters of the filled circles are proportional to the calculated absorption intensities. 124

5.4 Dipole allowed optical absorption energies and intensities of an InSb magnetic quantum dot with $r_o = 100$ nm and $B_z = 1$ T (upper frame), and an electrostatic quantum dot with confining energy, $\hbar\omega_o = 1$ meV (lower frame), containing one electron. The diameters of the filled circles are proportional to the calculated absorption intensities. 127

5.5 The upper frame shows the dipole allowed optical absorption energies and intensities of an InSb magnetic quantum dot with $r_o = 100$ nm and $B_z = 1$ T, containing two interacting electrons. The diameters of the filled circles are proportional to the calculated absorption intensities. The lower frame shows the ground state total angular momentum quantum number as a function of the external magnetic field 130

5.6 The upper frame shows the dipole allowed optical absorption energies and intensities of a GaAs magnetic quantum dot with $r_o = 50$ nm and $B_z = 5$ T, containing two interacting electrons. The diameters of the filled circles are proportional to the calculated absorption intensities. The inset shows the effect of the spin transition on the calculated data. The lower frame shows the ground state total angular momentum quantum number as a function of the external magnetic field 133

Acknowledgements

I would like to express my thanks to all the members of the theory group at Leicester for making my time here so enjoyable, and to my family for their support throughout my education. Special thanks are due to Dr Peter Maksym for many fruitful discussions, and for his excellent supervision and constant guidance during the course of this work.

Chapter 1

Introduction

The advent of new lithographic techniques have made it possible to couple a spatially inhomogeneous magnetic field, on a length scale of nanometres, to a two dimensional electron gas (2DEG). This technology has enabled novel magnetic structures to be investigated. Many of these structures have been fabricated by depositing magnetic strips near a 2DEG. These strips are generally ferromagnetic, and provide a spatially modulated magnetic field with a rectangular geometry. Alternatively, strips of superconducting material near a 2DEG in an external magnetic field can also be used to achieve this. If the spatially modulated magnetic field was of circular geometry, it would be possible to confine electrons to a disk region, in what is commonly termed a magnetic quantum dot. It has been suggested that such systems could be used as memory elements in future electronic components [1]. Magnetic quantum dots are dissimilar to electrostatic quantum dots in that the form of the confinement is different. It is therefore expected that the physical properties will also be different. Research in to these physical properties is very much in its infancy, and little work has been performed so far to investigate the physics of these novel and potentially fascinating systems. The main aim of this thesis is to redress this.

One of the reasons why these systems are of interest, is the way the inhomogeneous magnetic field affects the motion of the electrons in the system. There are regions of zero and non-zero magnetic field. In the region where the magnetic field is finite, the lowest energy state the electrons can occupy is the zeroth Landau level [2]. This state has an energy that is non-zero. In the region where the magnetic field is zero, the electrons are essentially free and the lowest energy state they can occupy is roughly zero. Therefore electrons moving from the zero magnetic field region will encounter an energy barrier. If the inhomogeneous magnetic field was circularly symmetric (as is the case of the magnetic quantum dot) this inhomogeneity could be used to confine electrons to a disk region.

To the authors knowledge magnetic quantum dots have not been realised experimentally. Other magnetically confined electron systems have been fabricated with a rectangular geometry [3, 4, 5, 6], and interesting physical effects, such as oscillations in the magnetoresistance have already been observed. Magnetic quantum dots have been the subject of some theoretical interest. The work by Solimany and Kramer [7], and independently Ibrahim and Peeters [8], was the first in this field. Solimany and Kramer [7] modelled the confining magnetic field in the magnetic quantum dot as a step function. That is, in the magnetic field free region the magnetic field is exactly zero, and in the region with magnetic field the confining magnetic field is equal to a constant. Although this is a good approximation for the majority of cases, it does not fully take in to account many recent experimental and theoretical findings [9, 10]. These findings show that a step function is not an accurate form for the confining magnetic field, if the ferromagnetic or superconducting material is very close to the 2DEG. In this regime, it is found that the confining magnetic field contains an overshoot at the

point where there is a transition from the magnetic field free region to the region with magnetic field. To take account of possible future experiments, this effect should be included in any theoretical model devised to describe the magnetic quantum dot. In the work performed by Peeters *et al* [9] and later by Reijniers *et al* [10], this effect is fully accounted for.

The most common technique employed to find the eigenstates of a magnetic quantum dot is wave function matching [7, 11, 12]. It is a requirement of quantum mechanics that the wave function of a system, and its derivative must be continuous. This is ensured by matching the wave functions and their derivatives at the discontinuity in the system. In the magnetic quantum dot this is the point at which there is a transition from the magnetic field free region to the region with magnetic field. By matching the wave functions and their derivatives at this transition point, the energy eigenvalues of the single electron system can be obtained.

In this thesis a further method to obtain the eigenstates of a magnetic quantum dot is employed. The method is exact numerical diagonalisation, and this, given infinite computer resources, can be used to determine the energy eigenvalues, not only of the ground state of a magnetic quantum dot but also of excited states. A significant advantage of the numerical diagonalisation over the technique discussed previously, is that the method is readily adapted to calculate the eigenstates of a magnetic quantum dot containing more than one electron. Peeters *et al* [9] and independently Reijniers *et al* [10] have considered a system containing more than one electron, however, these authors neglect the effect of the electron-electron interaction. Using the exact numerical diagonalisation method, the effect of the electron-electron interaction in a magnetic quantum dot is investigated in

this thesis for the first time. The electron-electron interaction is a fundamental property of a many electron system, and due to the scale of these systems, must be accounted for to obtain reliable results that are comparable with any future experimental data.

1.1 Aims

The aim of the present work is to develop a greater understanding of the potentially fascinating physics of magnetic quantum dots, and this goal is largely achieved through the investigation of the electronic and optical properties of this system. The physics of the single electron system is mostly understood, and much of it can be investigated with the techniques that have already been developed, such as numerical diagonalisation and wave function matching. To complete the single electron picture, in this work, the wave function matching method is applied, for the first time, to a magnetic quantum dot with an overshoot in the confining magnetic field. In contrast, the physics of the many electron system is yet to be examined fully, and the little work that has been performed in this field ignores the effect of the electron-electron interaction. This must be accounted for to obtain reliable results, and for the case of the electrostatic quantum dot it has been shown to result in a range of physically observable effects, and structure in the magnetisation and specific heat capacity has already been predicted [13, 14]. Due to the unique form of the confinement in a magnetic quantum dot, it is expected that the electron-electron interaction will strongly affect the electronic and optical properties of this system. For example, in contrast to an electrostatic quantum dot, confinement of interacting electrons is not always possible. Because the form of the confinement is such that it is constant everywhere outside a

magnetic quantum dot, certain energy conditions must be satisfied for interacting electrons to be confined. This unusual characteristic of a magnetic quantum dot is examined in great detail in this thesis, and it is found to have a great influence on the resulting physics of this system.

1.2 Synopsis of the Thesis

To complement the introductory information on magnetic quantum dots given in this chapter, in the following chapter a comprehensive discussion of the relevant background needed for subsequent chapters is given. In particular, fabrication techniques are suggested, and the magnetic field profiles in these proposed systems are described. Model magnetic field profiles are introduced that are based on the real magnetic field profiles. Given these, a simple theoretical model of a magnetic quantum dot is formulated, and this serves as a basis for the work contained in subsequent chapters.

In chapter 3, the theoretical model of a magnetic quantum dot is applied to a system containing one electron. Two different numerical methods are used to obtain the single electron eigenvalues. The first method is a numerical diagonalisation technique, and some details of this method are given in chapter 2. In chapter 3, this technique is developed further. The second method used to obtain the single electron results is a technique based on wave function matching. The matching technique is similar to those described in elementary quantum mechanics texts [15], in which solutions are required for systems with potential steps and potential wells for instance. It is found that severe numerical problems are encountered on applying wave function matching to a system with an overshoot in the confining magnetic field, and ways to overcome these problems

are given. Finally, the results obtained using both methods are compared and a discussion of the advantages and disadvantages associated with each method is given.

The main purpose of chapter 4 is to investigate the effect of the electron-electron interaction in a magnetic quantum dot. To the authors knowledge interaction effects have not been included in any calculations concerning magnetic quantum dots thus far, and therefore the results presented in this chapter are thought to be unique. The results are obtained using exact numerical diagonalisation, and in order to facilitate this the Coulomb matrix elements are required. This calculation is discussed in chapter 4, however, due to its complexity the details are given in appendix A. For a numerical diagonalisation calculation that includes a large number of Landau levels, numerical problems are encountered upon attempting to evaluate these matrix elements. These problems are discussed in detail and ways to overcome them are described. The eigenstates are obtained, firstly, for a system containing two interacting electrons. It is shown that confinement of two interacting electrons is possible, but only if certain energy conditions are satisfied. The effect of a homogeneous external magnetic field throughout the system is also considered. In a real system it is thought that the 2DEG would be of finite thickness, and therefore calculations are performed in order to reflect this. Other effects expected in a realistic system are speculated upon. A system containing three interacting electrons is investigated, and it is shown that it is possible to confine all three electrons in the magnetic quantum dot.

Chapter 5 begins with an overview of far infrared radiation (FIR) experiments, and specifically these experiments applied to electrostatic quantum dots. Subsequently the discussion is extended to include magnetic quantum dots. To

model the interaction of the electromagnetic radiation with the magnetic quantum dot the well known dipole approximation is used, and the dipole matrix elements are calculated. The FIR response of a magnetic quantum dot as a function of the confining magnetic field is calculated for a GaAs and InSb system containing one and two electrons. It is shown that the FIR response of the one and two electron systems is dissimilar and that this is a consequence of the electron-electron interaction in the two electron systems. The FIR response of a InSb magnetic quantum dot containing two interacting electrons is shown to have an unusual structure, and a possible explanation for this is given. The FIR response of a GaAs and InSb magnetic quantum dot is also calculated as a function of an external magnetic field. It is shown that the FIR response of the one electron GaAs system is similar to that of an electrostatic quantum dot. The FIR response of the two electron systems exhibit interesting structure, and this is shown to be a consequence of changes in the ground state quantum numbers as the external magnetic field increases.

Finally, chapter 6 summarises and concludes the work of this thesis. Additionally, suggestions are made for future work.

Chapter 2

Background

In this chapter, a theoretical model of a magnetic quantum dot is introduced. The model is used to determine the single electron hamiltonian of the system, which in turn is used to formulate a many electron hamiltonian. By numerically diagonalising the many electron hamiltonian, the eigenstates of a magnetic quantum dot can be determined. This method is used to obtain the energy eigenvalues of a single electron system in chapter 3, and a system containing up to three electrons in chapter 4. The single electron hamiltonian is also used in chapter 3, where an alternative method, based on a matching procedure, is used to determine the electron energies of a one electron system.

This chapter is organised as follows. First, an overview of existing magnetic structures and their properties is given. The next section is devoted to magnetic quantum dots. A description of two proposed fabrication techniques is presented. The form of the magnetic field profile in a magnetic structure is then investigated, and two model magnetic field profiles are introduced. The model magnetic field profiles are used in the following section, in which the theoretical framework for the description of a magnetic quantum dot is constructed. Finally, the numerical diagonalisation method is discussed.

2.1 Magnetic Structures

Several experimental groups have succeeded in coupling spatially periodic magnetic fields to a two dimensional electron gas (2DEG). H. A. Carmona *et al* [3] deposited an array of superconducting strips on the surface of a GaAs-AlGaAs heterostructure. P. D. Ye *et al* [6] and S. Izawa *et al* [5] achieved magnetic modulation by depositing ferromagnetic strips on top of a GaAs-AlGaAs heterostructure. The groups deposited arrays of strips with periods between 500 nm and 1 μm. In the experiments performed by H. A. Carmona *et al* [3], P. D. Ye *et al* [6] and S. Izawa *et al* [5] the magnetoresistance oscillations predicted by Peeters and Vasilopoulos [16] were observed for the first time. These oscillations are analogous to the Weiss oscillations observed when a 2DEG is subject to a weak periodic electric field [17]. The oscillations result from a commensurability effect between the two characteristic length scales of the system: the classical cyclotron radius and the period of the magnetic modulation. Further experiments have been performed to investigate the magnetoresistance of hybrid ferromagnetic/semiconductor devices. The group at Nottingham [18] have measured the magnetoresistance, and used this to deduce the hysteretic properties of a thin ferromagnetic line on top of a 2DEG. The same group have also investigated the temperature dependence of the magnetoresistance in these devices [19], and found that for a given magnetic field the magnetoresistance decreases with increasing temperature.

Many other magnetic structures have been proposed and have been investigated theoretically. Ibrahim and Peeters [8] have considered several systems in which a periodic magnetic field is present. These include a magnetic Kronig-Penney system in which the magnetic field profile consists of a periodic array of δ

functions with alternating sign, a system with a sawtooth magnetic field profile, a system with a sinusoidal magnetic field profile and a system with a step function magnetic field profile. While the previous work is concerned with periodic magnetic structures, earlier work by Peeters and Matulis [20] includes a theoretical investigation of electrons coupled to a one dimensional magnetic step, magnetic barrier and magnetic well. Further theoretical work has been performed by a number of groups [7, 9, 11, 12], to investigate the properties of a two dimensional magnetic well with cylindrical symmetry. A system with this form is known as a magnetic quantum dot, and its electronic and optical properties form the foundation for the work contained in this thesis.

2.2 Magnetic Quantum Dots

In this section the fabrication techniques employed by H. A. Carmona *et al* [3], P. D. Ye *et al* [6] and S. Izawa *et al* [5] are discussed. It is proposed that the techniques may be adapted to produce a magnetic quantum dot. The form of the magnetic field profile in a magnetic quantum dot is then investigated, and finally a theoretical model of a magnetic quantum dot is developed.

2.2.1 Fabrication Techniques

The system investigated by H. A. Carmona *et al* [3] consists of a 2DEG formed in a standard GaAs-AlGaAs heterostructure. A metallic gold gate, thickness 150 nm, is deposited on the surface of the heterostructure. The purpose of the gold gate is to screen the electric field modulations that are produced by the differential contraction between the superconducting strips and the 2DEG [21]. Insulating germanium of thickness 200 nm is then deposited and finally, superconducting

strips of thickness 100-200 nm are fabricated. P. D. Ye *et al* [6] and S. Izawa *et al* [5] deposited ferromagnetic instead of superconducting strips. P. D. Ye *et al* [6] used a 10 nm NiCr film to screen the electric field modulations, and deposited 200 nm dysprosium strips, while S. Izawa *et al* [5] deposited 150 nm nickel strips and screened the electric field modulations by electrically connecting them, to ensure that all parts of the striped gate were at the same electrical potential.

In this chapter, both methods of fabricating magnetic structures are discussed and it is shown in the next section that the fabrication method affects the magnetic field profile in the structure. To fabricate a magnetic quantum dot, the previous techniques need only a slight modification. Figure 2.1 (top) shows a schematic diagram of a proposed magnetic quantum dot structure that is fabricated by depositing a ferromagnetic film. It is proposed that a thin film of ferromagnetic material, which is magnetised in the growth direction of the structure, is deposited over the area of the device. Using lithography techniques a cylinder of this thin film could be etched away, leaving a volume at the centre of the device devoid of magnetic material. Figure 2.1 (bottom) shows a schematic diagram of a proposed magnetic quantum dot structure that is fabricated by depositing a superconducting material near to a 2DEG. To fabricate this structure, it is proposed that a thin disk of a superconducting material is placed on top of the 2DEG. If the system is subject to an external magnetic field, the superconducting disk would screen the magnetic field directly underneath, a consequence of the Meissner effect. If it is assumed that the structures are of similar dimensions to those used in the experiments performed by H. A. Carmona *et al* [3], P. D. Ye *et al* [6] and S. Izawa *et al* [5], the dimension of the structures in the growth direction is approximately 700 nm.

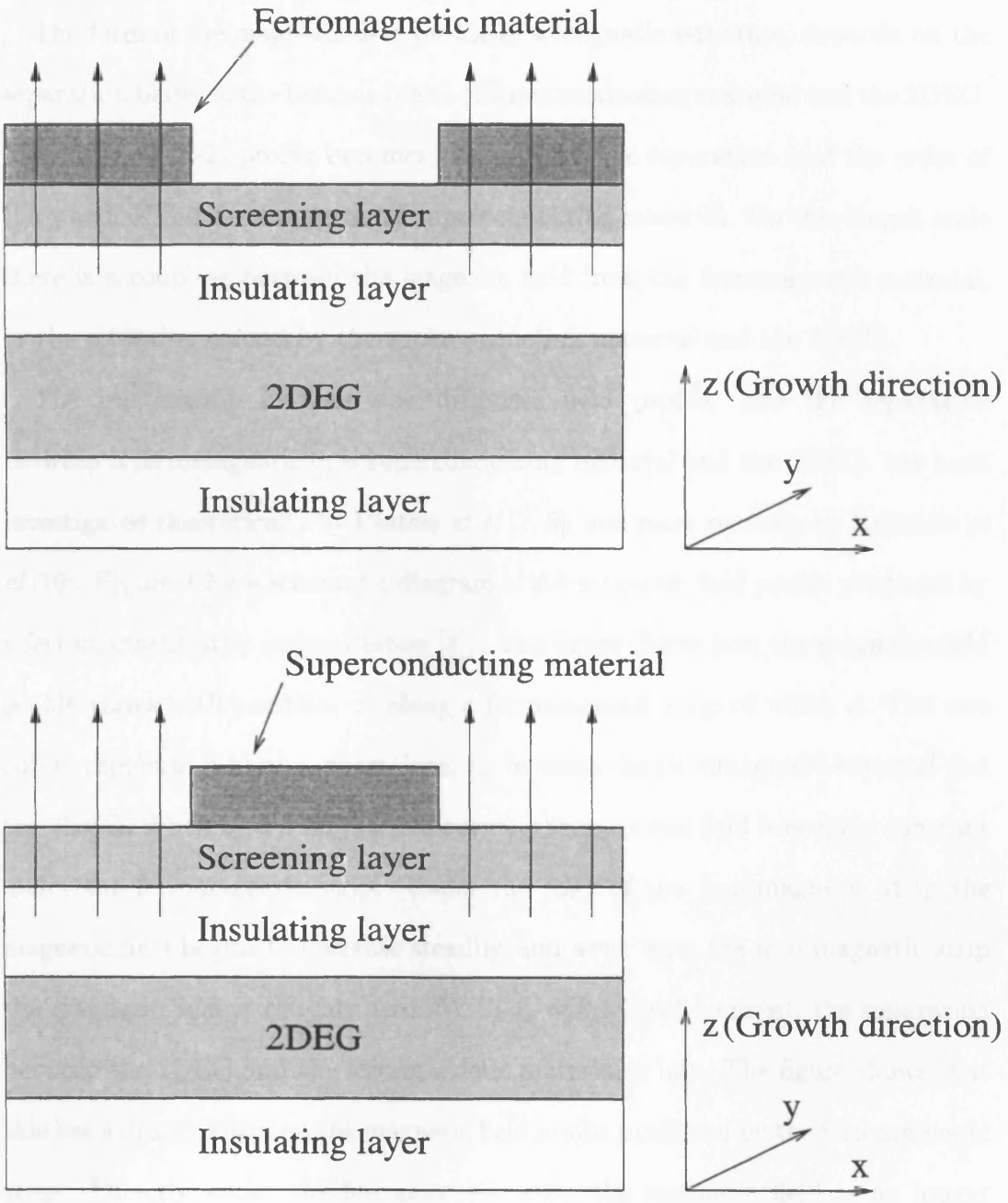

Figure 2.1: Schematic diagram of a proposed magnetic quantum dot structure fabricated using a ferromagnetic material (top) and a superconducting material (bottom). The vertical arrows indicate the location and direction of the intrinsic magnetic field (top) and the external magnetic field (bottom).

2.2.2 Magnetic Field Profile

The form of the magnetic field profile in a magnetic structure, depends on the separation between the ferromagnetic or superconducting material and the 2DEG. The magnetic field profile becomes interesting if the separation is of the order of the width of the ferromagnetic or superconducting material. On this length scale there is a coupling between the magnetic field from the ferromagnetic material, or the screening caused by the superconducting material and the 2DEG.

The relationship between the magnetic field profile, and the separation between a ferromagnetic or a superconducting material and the 2DEG, has been investigated theoretically by Peeters *et al* [1, 9], and more recently by Reijniers *et al* [10]. Figure 2.2 is a schematic diagram of the magnetic field profile produced by a ferromagnetic strip (after Peeters [1]). The figure shows how the magnetic field profile varies with position, x, along a ferromagnetic strip of width d. The two curves represent differing separations, z_o, between the ferromagnetic material and the 2DEG. When $z_o = 0.3d$ (dashed curve), the magnetic field is roughly constant under the ferromagnetic strip. Under the edge of the ferromagnetic strip the magnetic field begins to decrease steadily, and away from the ferromagnetic strip the magnetic field is roughly zero. With $z_o = 0.1d$ (solid curve), the separation between the 2DEG and the ferromagnetic material is less. The figure shows that this has a drastic effect on the magnetic field profile produced by the ferromagnetic strip. Directly under the ferromagnetic strip the magnetic field is no longer constant. At the edge of the ferromagnetic strip the magnetic field decreases sharply and becomes negative, before eventually rising to roughly zero away from the ferromagnetic strip. The differing forms of these two curves can be explained with the aid of figure 2.3. The figure shows a schematic diagram of the magnetic

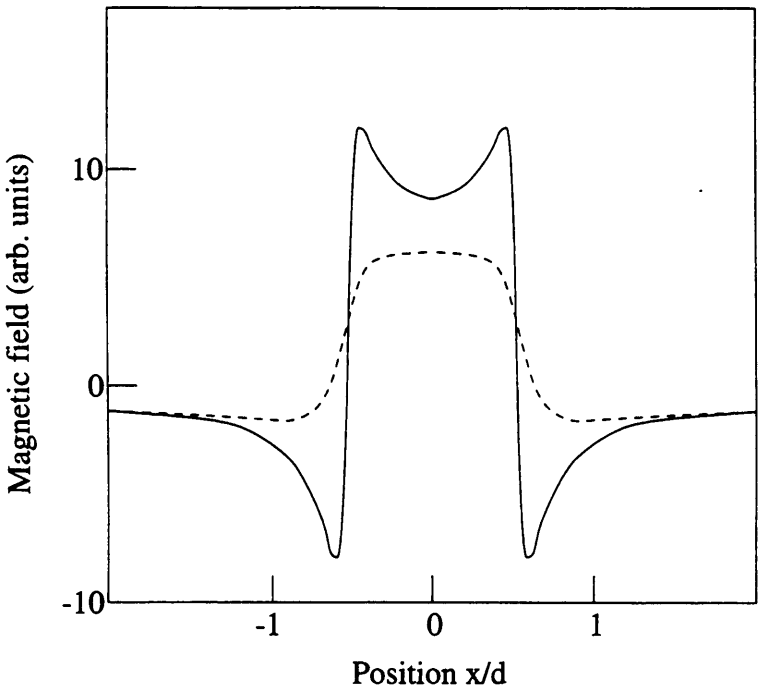

Figure 2.2: Schematic diagram of the magnetic field profile produced by a ferromagnetic strip (after Peeters [1]). The solid curve is for $z_o = 0.1d$ and the dashed curve is for $z_o = 0.3d$.

field lines around a ferromagnetic material close to a 2DEG. When $z_o = 0.1d$, it is seen that all the magnetic field lines penetrate into the 2DEG. The figure shows that the direction of the magnetic field of the inner magnetic field line (closest to the edge of the ferromagnetic strip) is into the 2DEG, this would produce a net negative magnetic field in this region, hence explaining the negative trough present in figure 2.2. Underneath the ferromagnetic strip, the direction of the magnetic field is out of the 2DEG, this results in a net positive magnetic field, hence the positive magnetic field in figure 2.2. When $z_o = 0.3d$, the 2DEG is further away from the ferromagnetic strip. In this case, the inner magnetic field lines would not penetrate into the 2DEG under the edge of the ferromagnetic strip, hence there would be no net negative magnetic field in this region, and the negative trough present in the previous example is no longer present.

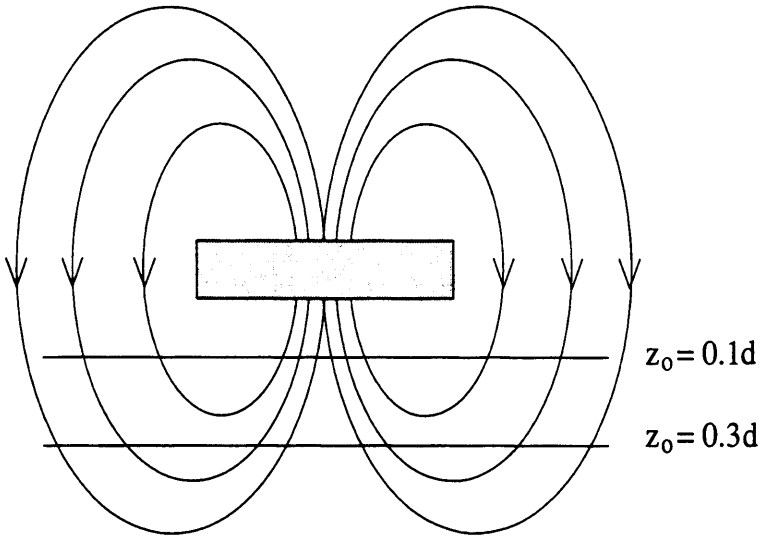

Figure 2.3: Schematic diagram of the magnetic field lines emanating from a ferromagnetic material. The solid horizontal lines indicate the position of the 2DEG, with a separation, z_o, between the 2DEG and ferromagnetic material.

A structure fabricated by depositing a superconducting material near to a 2DEG has a very different magnetic field profile. Reijniers *et al* [10] calculated the magnetic field profile induced in the 2DEG by a very thin superconducting disk subject to an external magnetic field. The results of these calculations are shown in figure 2.4. The figure shows a schematic diagram of a figure from Reijniers *et al* [10]. Magnetic field profiles for two differing separations, z, between the 2DEG and superconducting disk are shown, and all lengths are measured in units of the superconducting disk radius a. It is seen that for both curves, the magnetic field under the superconducting disk (between $r/a = 0$ and $r/a = 1$) is small. This is a consequence of the Meissner effect. The magnetic field far from the disk becomes equal to the external magnetic field B_a. It is the form of the magnetic field under the edge of the superconducting disk that is of interest. The figure shows that for both curves there is an overshoot of the magnetic field.

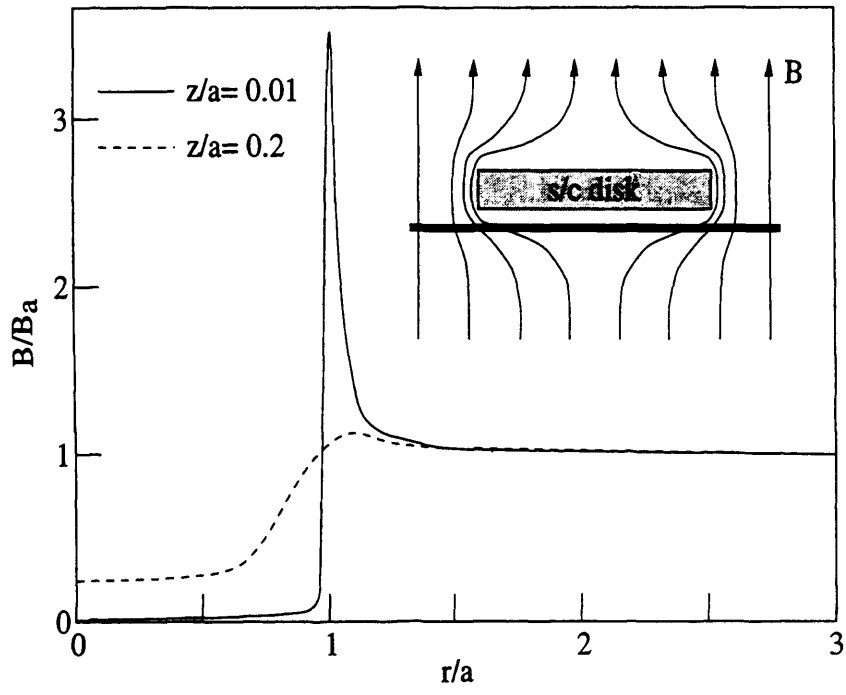

Figure 2.4: Schematic diagram of a figure from Reijniers *et al* [10], showing the magnetic field profile produced by a superconducting (s/c) disk subject to an external magnetic field. The radius of the s/c disk is denoted by a and B_a is the external magnetic field. The inset shows a schematic diagram of the external magnetic field lines around the s/c disk close to a 2DEG (indicated by thick horizontal line).

For $z/a = 0.2$ (dashed curve) this overshoot is only slight, but for $z/a = 0.01$ (solid curve) the magnetic field overshoot is very prominent. The cause of the prominent overshoot is attributed to the dense magnetic field lines around the edge of the superconducting disk (see inset in figure 2.4). When the disk is close to the 2DEG, these dense magnetic field lines penetrate into the 2DEG, this results in a large positive magnetic field in this region. As the disk is moved away from the 2DEG, the magnetic field lines in the 2DEG under the edge of the superconducting disk become less dense, hence the overshoot becomes less prominent.

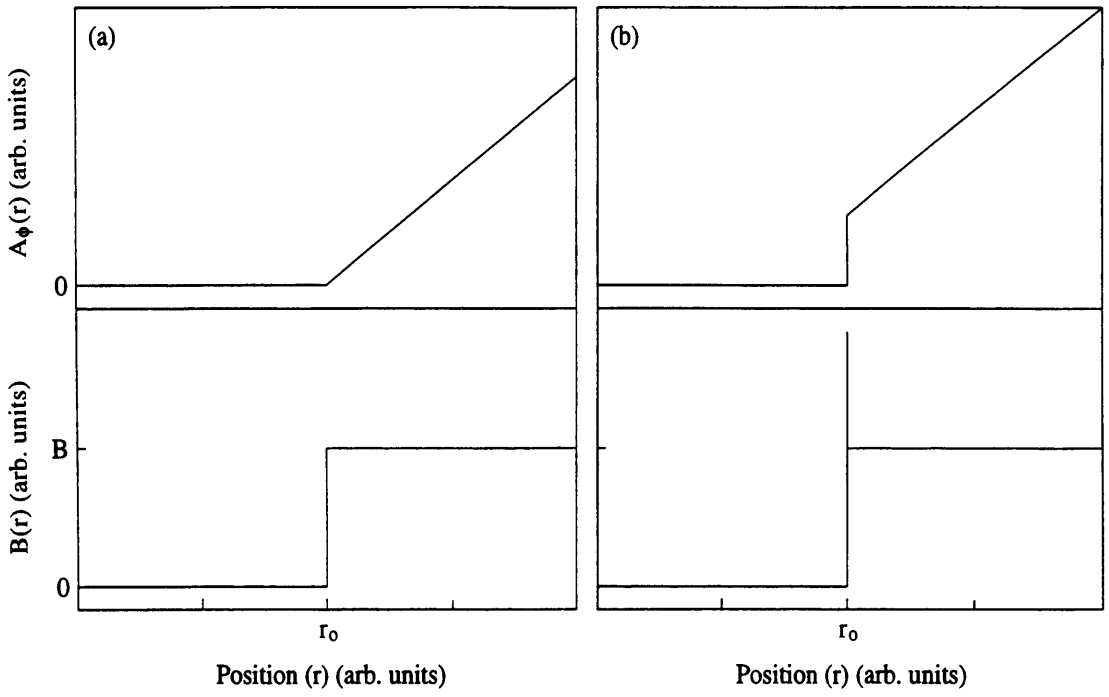

Figure 2.5: Model magnetic field profiles and their corresponding vector potentials.

In order to simplify the theoretical model that is discussed in the next section, two model magnetic field profiles that approximate the real magnetic field profiles shown in figure 2.2 and figure 2.4 are introduced. The model magnetic field profiles that are proposed are shown in figure 2.5, along with their corresponding vector potentials. The magnetic field profile shown in the lower frame of figure 2.5 (a), could represent a real system in which a superconducting disk and 2DEG are separated by roughly $z = 0.2r_o$ (see dashed curve in figure 2.4). The profile could also represent the magnetic field profile produced by a ferromagnetic material when the separation between the ferromagnetic material and 2DEG is roughly $0.3d$ (see dashed curve in figure 2.2). Upon comparing the real magnetic field profiles with the model profile, several small differences are noticed. The model does not account for the slight overshoot of the magnetic field at r_o (dashed curve in figure 2.4), and the non-zero magnetic field in the region directly under

the superconducting disk (dashed curve in figure 2.4) or in the region not directly under the ferromagnetic material (dashed curve in figure 2.2). The lower frame of figure 2.5 (b) shows a second model magnetic field profile. The model represents quite well the real magnetic field profile shown by the solid curve in figure 2.4. The prominent overshoot seen in figure 2.4 is represented in the model by a δ function at r_o.

Reijniers *et al* [10] have calculated the single electron energy spectrum for a magnetic quantum dot, using the model magnetic field profiles and the real magnetic field profile. They found that including the real magnetic field profile in their calculations, produced results which show an intermediate behaviour between the results produced using the two model profiles. The calculation using the real magnetic field profile did not alter their conclusions qualitatively. It is therefore supposed, that the two model magnetic field profiles contain all the essential physics of the system.

2.2.3 Theoretical Model of a Magnetic Quantum Dot

In this section, a simple theoretical model to describe a magnetic quantum dot is developed. A common approximation utilised when modelling quantum dots, and employed here, is to assume that the electrons move in the $x-y$ plane. This is justified because in these devices the confinement in the $x-y$ plane is much weaker than in the growth direction, z. If this is the case then the 2DEG can be treated as a layer of infinitesimally small thickness, and the magnetic quantum dot can essentially be treated as a two dimensional system. In a real system the 2DEG is of finite thickness. A more sophisticated model is introduced in chapter 4 to take account of this.

For a system in which the 2DEG is treated as a layer of infinitesimally small thickness, the model is one in which the electrons move in the $x-y$ plane and are subject to a perpendicular magnetic field, $\mathbf{B} = (0, 0, B_z)$. The device has cylindrical symmetry, and it is assumed that the magnetic field is non-zero except within a cylinder of radius r_o. As with many quantum mechanics problems, the starting point is to write down the hamiltonian that describes the system. For a system that is subject to a magnetic field, it is well known from classical electrodynamics that the hamiltonian is

$$h = \frac{(\mathbf{p} + e\mathbf{A}(\mathbf{r}))^2}{2m^*}, \tag{2.1}$$

where e is the absolute value of the electronic charge, m^* is the effective mass of the electron, $\mathbf{p}$ is the momentum of the electron and $\mathbf{A}(\mathbf{r})$ is the vector potential. Expanding the square on the right hand side of Eq. 2.1, replacing $\mathbf{p}$ by the momentum operator, $-i\hbar\nabla$, and adding a Zeeman energy term gives

$$h = -\frac{\hbar^2}{2m^*}\nabla^2 - \frac{ie\hbar}{m^*}\mathbf{A}(\mathbf{r})\cdot\nabla + \frac{e^2}{2m^*}\mathbf{A}(\mathbf{r})^2 + g^*\mu_B B_z S_z, \tag{2.2}$$

where g^* is the effective g factor, μ_B is the Bohr magneton and S_z is the z component of the electron spin. Due to the inhomogeneity of the magnetic field in the system, the vector potential has the general form defined by

$$\mathbf{A} = \begin{cases} \mathbf{A}(\mathbf{r}) & \text{for } r > r_o, \\ 0 & \text{for } r < r_o, \end{cases} \tag{2.3}$$

where r is the cylindrical radial coordinate. At this point an explicit form for the vector potential is needed.

To obtain a form for the vector potential the relation $\mathbf{B} = \nabla \times \mathbf{A}$ is used. In cylindrical coordinates, the vector potential is $\mathbf{A} = (A_r, A_\phi)$, where A_r is the r component, and A_ϕ is the ϕ component of the vector potential. In this model the

magnetic field is directed along the z axis, and so $A_r = 0$. The magnetic field is then given by

$$B(r) = \frac{1}{r}\frac{\partial}{\partial r}(rA_\phi(r)). \tag{2.4}$$

Using Eq. 2.4 it is possible, given the magnetic field profile, to determine an explicit form for the vector potential in the system. The model magnetic field profiles discussed in the previous section are now utilised. Figure 2.5 (a) (bottom) shows a model magnetic field profile with the form of a step function. Mathematically this may be written as

$$B(r) = B_z\theta(r - r_o), \tag{2.5}$$

where $\theta(r - r_o) = 1$ for $r > r_o$ and $\theta(r - r_o) = 0$ for $r < r_o$ is the step function. The lower frame of figure 2.5 (b) shows a model magnetic field profile also with a step function form, but with a δ function at r_o. This may be written as

$$B(r) = B_z\theta(r - r_o) + B_z r\delta(r - r_o)/2. \tag{2.6}$$

Given the magnetic field profiles, it is now possible to determine the vector potential in each case. To do this, the magnetic field profiles are substituted into Eq. 2.4 and the equation is solved for $A_\phi(r)$. The vector potential corresponding to a magnetic field profile given by Eq. 2.5, is shown in the upper frame of figure 2.5 (b), and can be written as

$$A_\phi(r) = \frac{B_z r}{2}\left[1 - \frac{r_o^2}{r^2}\right]\theta(r - r_o). \tag{2.7}$$

That corresponding to Eq. 2.6 is given by

$$A_\phi(r) = \frac{B_z r}{2}\theta(r - r_o), \tag{2.8}$$

the form of which is shown in the upper frame of figure 2.5 (a). It should be apparent that while these two forms for the vector potential approximate

the vector potentials in the real systems well, they are independent of z, the separation between the ferromagnetic material or superconducting disk and the 2DEG. To avoid repeatedly referring to Eq. 2.7 and Eq. 2.8, in subsequent chapters, a system with a vector potential given by Eq. 2.7 is referred to as a system without a magnetic field overshoot at r_o, and a system with a vector potential given by Eq. 2.8 is referred to as a system with a magnetic field overshoot at r_o. In the following section, the hamiltonian is used to develop a numerical diagonalisation method. In subsequent chapters this method is employed to determine the energy spectrum for the magnetic quantum dot system.

2.3 Numerical Diagonalisation

In this section, a numerical diagonalisation technique is discussed. The method is used to calculate the eigenstates of a single electron system and a system containing up to three interacting electrons in chapter 3 and chapter 4 respectively. The basic idea is to diagonalise an N-electron hamiltonian. This is accomplished by using a many particle basis set, that is a many particle wave function expressed as an infinite sum of Slater determinants. Given infinite computer resources, a calculation of this type would yield the exact energy eigenvalues, not only of the ground state but also of excited states. Obviously the use of an infinite series of Slater determinants is not a viable option, and therefore to make the problem tractable the many particle basis set must be truncated. The choice of the single particle functions from which the Slater determinants are constructed is of course arbitrary. However, to reduce the number of basis states required to achieve a good accuracy in the calculation, it is prudent to choose single particle functions that describe the system as well as possible.

The system consists of N-interacting electrons. As usual, the starting point is to write down the hamiltonian describing the system. This has the form

$$H = \sum_{i=1}^{N} h(\mathbf{r}_i) + \frac{1}{2}\sum_{i=1}^{N}\sum_{\substack{j=1 \\ j\neq i}}^{N} v(\mathbf{r}_i, \mathbf{r}_j), \tag{2.9}$$

where the first term gives the single particle energy of the system and the second term describes the Coulomb interaction between the electrons. To aid computation of the energy eigenvalues, the transformation to an occupation number representation is made. This yields

$$H = \sum_{i,j}\langle i|h|j\rangle c_i^\dagger c_j + \frac{1}{2}\sum_{i,j,k,l}\langle ij|v|kl\rangle c_i^\dagger c_j^\dagger c_l c_k, \tag{2.10}$$

where i, j, k and l are single particle states, $c_i^\dagger$ is a creation operator and c_i is a destruction operator. Explicitly the matrix elements in Eq. 2.10 have the form

$$\langle i|h|j\rangle = \int \psi_i^*(\mathbf{r})h(\mathbf{r})\psi_j(\mathbf{r})d\mathbf{r} \tag{2.11}$$

and

$$\langle ij|v|kl\rangle = \int\int \psi_i^*(\mathbf{r}_1)\psi_j^*(\mathbf{r}_2)v(\mathbf{r}_1,\mathbf{r}_2)\psi_k(\mathbf{r}_1)\psi_l(\mathbf{r}_2)d\mathbf{r}_1 d\mathbf{r}_2. \tag{2.12}$$

To determine the energy eigenvalues of the system, the N-electron hamiltonian given by Eq. 2.10, is diagonalised. There exist many algorithms to accomplish this. To obtain the results shown in this thesis a standard "Black Box" routine from the NAG library is used. A routine of this form is capable of diagonalising matrices with an order equal to several thousand. The largest hamiltonian matrix utilised in this work is typically 1000×1000.

To construct the Slater determinants, the single particle functions are chosen to be the well known Fock-Darwin states [22, 23]. These states form the exact solution of a system with one electron in a homogeneous magnetic field, and are

given by

$$\psi_{\text{FD}}(r,\phi) = N_{nl} e^{-r^2/2l_B^2} \left(\frac{r^2}{2l_B^2}\right)^{\frac{|l|}{2}} L_n^{|l|}\left(\frac{r^2}{2l_B^2}\right) e^{-il\phi}, \tag{2.13}$$

where

$$N_{nl} = \frac{1}{l_B\sqrt{2\pi}}\sqrt{\frac{n!}{(n+|l|)!}} \tag{2.14}$$

is a normalisation constant, $l_B = \sqrt{\hbar/eB}$ is the magnetic length, n is the radial quantum number, l is the angular momentum quantum number and $L_n^{|l|}(r^2/2l_B^2)$ is an associated Laguerre polynomial. The reason for this choice of single particle function, as opposed to $\psi_i(r,\phi)$, which is an eigenstate of h, becomes apparent on attempting to calculate the Coulomb matrix elements (Eq. 2.12). If the exact eigenstates of h are chosen as the single particle functions, the calculation of the Coulomb matrix elements involves evaluating complicated integrals in two regions, $r > r_o$ and $r < r_o$. With $\psi_{\text{FD}}(r,\phi)$ as the single particle functions, a relatively simple analytic form for the Coulomb matrix elements is obtained, which can be evaluated using existing software [24]. Although $\psi_{\text{FD}}(r,\phi)$ is not an exact eigenstate of h, for a system with a small magnetic quantum dot radius (r_o), accurate values for the energy eigenvalues should be attainable with a reasonable number of basis states. Convergence and numerical issues will be discussed in more detail in subsequent chapters. Given the form of the single particle function it is now possible to calculate explicitly the single electron matrix elements (Eq. 2.11) and the two electron matrix elements (Eq. 2.12). In chapter 3 the details of the single electron matrix element calculations are given. The calculation of the two electron matrix element is rather more complicated and is discussed in chapter 4, and further details are given in appendix A.

Chapter 3

Single Electron in a Magnetic Quantum Dot

In this chapter, the properties of a single electron in a magnetic quantum dot are investigated. The single electron energies of the system are obtained using two methods, the numerical diagonalisation method, which is discussed in chapter 2, and a matching procedure. Essentially the matching procedure involves solving the Schrödinger equation in the regions $r < r_o$ and $r > r_o$, and matching the wave functions at the boundary, r_o. The matching technique has already been applied successfully to a system without a magnetic field overshoot at r_o [7, 11, 12]. However, for a system with a magnetic field overshoot at r_o, the author is unaware of any work in which the matching procedure is used to determine the single electron energies of the system. In this chapter the matching procedure is used to the determine the energies of such a system, and ways to overcome the numerical problems associated with evaluating the energies are given.

A considerable amount of theoretical work has already been performed for a system without a magnetic field overshoot at r_o. An example of such work, is that performed by Solimany and Kramer [7]. They determined the energy spectrum of the system using a matching procedure. The energies they obtained as a function of the angular momentum quantum number, were compared with

the corresponding energies for a system with a single electron in a homogeneous magnetic field (commonly known as Landau levels [2]). Their results show that the single electron energies increase or decrease with angular momentum quantum number, depending on the sign of the angular momentum quantum number, as compared to the Landau levels. The same system has also been investigated by Heung-Sun Sim *et al* [11]. They calculated the classical trajectories of an electron in a magnetic quantum dot and the corresponding probability densities for various eigenstates. They found that if the classical trajectory passes through the origin of the magnetic quantum dot, the state carries no current. A system with a magnetic field overshoot at r_o has been studied by Peeters *et al* [9] and more recently by Reijniers *et al* [10]. To obtain the energies of the system, they solved the Schrödinger equation numerically, using a Newton iteration technique and subjected the solution to the appropriate boundary conditions. Their results show, in contrast to the previous system, that the electron energy is increased when the maximum of the electron wave function is situated near r_o.

This chapter is organised as follows. First, the system without a magnetic field overshoot at r_o is investigated. The single electron matrix elements for the system are calculated. In the next section the matching procedure is described in detail, and finally results calculated using the numerical diagonalisation method and the matching procedure are presented. The results show the energy as a function of angular momentum quantum number and magnetic quantum dot radius. Further results showing the electron density of several systems are also presented. In the second part of the chapter the system with a magnetic field overshoot is investigated. The single electron matrix elements are given. In the next section the matching procedure and the numerical problems encountered

on applying it to this system are described. Finally, results calculated using the numerical diagonalisation method and the matching procedure are presented, and comparisons are made with the results obtained for a system without a magnetic field overshoot at r_o.

3.1 A System without a Magnetic Field Overshoot

3.1.1 Calculation of the Single Electron Matrix Elements

In this section, the single electron matrix elements given by Eq. 2.11 are calculated explicitly. To do this the hamiltonian inside the magnetic quantum dot ($h_{r<r_o}$) and the hamiltonian outside the magnetic quantum dot ($h_{r>r_o}$) are determined. Once the hamiltonians have been found, the integrals in Eq. 2.11 can be evaluated, giving an explicit form for the single electron matrix element.

The hamiltonian for a single electron in the magnetic field free region ($r < r_o$) is the hamiltonian for a free electron and is given by

$$h_{r<r_o} = -\frac{\hbar^2}{2m^*}\nabla^2, \tag{3.1}$$

while in the region with magnetic field ($r > r_o$), the hamiltonian is given by Eq. 2.2. Upon substitution of the vector potential for the system without magnetic field overshoot, which is given by Eq. 2.7, into Eq. 2.2, the second and third terms in the resulting equation take on the form

$$-\frac{ie\hbar}{m^*}\mathbf{A}(\mathbf{r})\cdot\nabla = \frac{e}{2m^*}\left[1-\frac{r_o^2}{r^2}\right]\mathbf{L}\cdot\mathbf{B}, \tag{3.2}$$

and

$$\frac{e^2}{2m^*}\mathbf{A}(\mathbf{r})^2 = \frac{e^2B_z^2r^2}{8m^*} - \frac{e^2B_z^2r_o^2}{4m^*} + \frac{e^2B_z^2r_o^4}{8m^*r^2} \tag{3.3}$$

respectively, where $\mathbf{L} = -\hbar l\hat{\mathbf{z}}$ is the angular momentum. Introducing $\omega_c = eB_z/m^*$, where ω_c is the cyclotron frequency, it follows that

$$\begin{aligned} h_{r>r_o} &= -\frac{\hbar^2}{2m^*}\nabla^2 + \frac{m^*\omega_c^2 r^2}{8} - \frac{\hbar\omega_c l}{2} + \frac{\hbar\omega_c l r_o^2}{2r^2} \\ &- \frac{m^*\omega_c^2 r_o^2}{4} + \frac{m^*\omega_c^2 r_o^4}{8r^2} + g^*\mu_B B_z S_z. \end{aligned} \tag{3.4}$$

where, for the system in question, ∇^2 takes its cylindrical coordinate representation, i.e

$$\nabla^2 = \frac{\partial^2}{\partial r^2} + \frac{1}{r}\frac{\partial}{\partial r} + \frac{1}{r^2}\frac{\partial^2}{\partial \phi^2}, \tag{3.5}$$

with ϕ being the polar angle. At this stage it is possible to calculate the integral in Eq. 2.11. The term containing ∇^2 is present in both Eq. 3.1 and Eq. 2.2, hence this is integrated over all space, i.e from 0 to ∞. The remaining terms, are present in the hamiltonian that describes the region outside the magnetic quantum dot, so these are integrated from r_o to ∞. Thus

$$\begin{aligned} \langle i|h|j\rangle &= \int_0^{2\pi}\int_{r_o}^{\infty} \psi^*_{n'l'}(r,\phi)\left[\frac{m^*\omega_c^2 r^2}{8} - \frac{\hbar\omega_c l}{2} + \frac{\hbar\omega_c l r_o^2}{2r^2} - \frac{m^*\omega_c^2 r_o^2}{4}\right. \\ &+ \left.\frac{m^*\omega_c^2 r_o^4}{8r^2} + g^*\mu_B B_z S_z\right]\psi_{nl}(r,\phi) r dr d\phi \\ &+ \int_0^{2\pi}\int_0^{\infty} \psi^*_{n'l'}(r,\phi)\left[-\frac{\hbar^2}{2m^*}\nabla^2\right]\psi_{nl}(r,\phi) r dr d\phi. \end{aligned} \tag{3.6}$$

Substituting the explicit form for the single particle wave function (Eq. 2.13) into this equation and introducing the dimensionless variable $x = r^2/2l_B^2$ gives

$$\begin{aligned} \langle i|h|j\rangle &= \delta_{ll'}\left\{\left[\frac{\hbar\omega_c}{2}\left((2n+|l|+1)-l\right) - \frac{m^*\omega_c^2 r_o^2}{4} + g^*\mu_B B_z S_z\right]\delta_{nn'}\right. \\ &+ \frac{r_o^2}{l_B^2}\left[\frac{\hbar\omega_c l}{4} + \frac{m^*\omega_c^2 r_o^2}{16}\right]\lambda_n\lambda_{n'}\int_{x_o}^{\infty} e^{-x}x^{|l|-1}L_{n'}^{|l|}(x)L_n^{|l|}(x)dx \\ &+ \left[\frac{\hbar\omega_c l}{2} + \frac{m^*\omega_c^2 r_o^2}{4} - g^*\mu_B B_z S_z\right]\lambda_n\lambda_{n'}\int_0^{x_o} e^{-x}x^{|l|}L_{n'}^{|l|}(x)L_n^{|l|}(x)dx \\ &- \left.\frac{\hbar\omega_c}{4}\lambda_n\lambda_{n'}\int_0^{x_o} e^{-x}x^{|l|+1}L_{n'}^{|l|}(x)L_n^{|l|}(x)dx\right\}, \end{aligned} \tag{3.7}$$

where $\lambda_n = \sqrt{n!/(n+|l|)!}$. There exist many integration routines that can be used to evaluate the integrals in Eq. 3.7, for example, Simpson's rule or the trapezium rule. However, these routines often require the integrand to be evaluated at a large number of points to obtain an accurate result. A more efficient routine, that yields the exact result if the integral is of the form $\int_a^\infty e^{-x}P(x)dx$, where $P(x)$ is a polynomial, and $a \geq 0$, is a modified Gauss-Laguerre integration routine [25]. The routine that is used is from the NAG library, and is exact for an integral with a finite lower limit. By evaluating each of the integrands in Eq. 3.7 at 32 points, integrals are evaluated that are accurate to at least seven decimal places. This accuracy of the results is determined by comparing the results, with those obtained using the computational mathematics software, Maple.

3.1.2 Matching Procedure

In this section, a technique is described to obtain the single electron energies of an electron in a magnetic quantum dot. The method that is described is similar to that used when solving the potential step problem encountered in elementary quantum mechanics, and involves the matching of solutions at a discontinuous boundary. To obtain the single electron energies of the system, the Schrödinger equation is solved for the two regions, inside the magnetic quantum dot ($r < r_o$) and outside the magnetic quantum dot ($r > r_o$). The energies are obtained by matching the wave functions and their derivatives at the boundary r_o.

For the region $r < r_o$, the Schrödinger equation is given by $h_{r<r_o}\psi_{r<r_o}(r,\phi) = E\psi_{r<r_o}(r,\phi)$, where $h_{r<r_o}$ is the hamiltonian for a free electron and is given by

Eq. 3.1. On substituting Eq. 3.5 into Eq. 3.1, the Schrödinger equation becomes

$$-\frac{\hbar^2}{2m^*}\left[\frac{\partial^2}{\partial r^2}+\frac{1}{r}\frac{\partial}{\partial r}+\frac{1}{r^2}\frac{\partial^2}{\partial \phi^2}\right]\psi_{r<r_o}(r,\phi)=E\psi_{r<r_o}(r,\phi). \tag{3.8}$$

Taking advantage of the cylindrical symmetry of the problem allows the wave function to be written in its separable form, $\psi_{r<r_o}(r,\phi) = u_{r<r_o}(r)e^{-il\phi}$. Upon substitution into Eq. 3.8, with $k^2 = 2m^*E/\hbar^2$ and $\rho = kr$ it follows that

$$\rho^2\frac{d^2u}{d\rho^2}+\rho\frac{du}{d\rho}+(\rho^2-l^2)u=0. \tag{3.9}$$

This is Bessel's differential equation, and the solution is a combination of Bessel functions, $J_l(x)$, and Neumann functions, $N_l(x)$. Because of the non-regularity of the Neumann function at $r = 0$, this function is disregarded, and the required solution is

$$u_{\eta<\eta_o}(\eta) = CJ_l(\sqrt{2\varepsilon}\eta), \tag{3.10}$$

where C is a normalisation constant, and the dimensionless quantities, $\varepsilon = E/\hbar\omega_c$ and $\eta = r/l_B$, have been introduced.

In the region $r > r_o$, the Schrödinger equation is given by $h_{r>r_o}\psi_{r>r_o}(r,\phi) = E\psi_{r>r_o}(r,\phi)$, with $h_{r>r_o}$ given by Eq. 3.4. The Zeeman term provides only a small contribution to the total energy of the system, and is neglected in this chapter without affecting the resulting physics. In subsequent chapters Zeeman splitting is taken fully into account. Again, a wave function of separable form $\psi_{r>r_o}(r,\phi) = u_{r>r_o}(r)e^{-il\phi}$, is employed. Upon substitution of $h_{r>r_o}$ and $\psi_{r>r_o}(r,\phi) = u_{r>r_o}(r)e^{-il\phi}$ into the Schrödinger equation and introducing the dimensionless quantities $\varepsilon = E/\hbar\omega_c$ and $\eta = r/l_B$, it follows that

$$\frac{d^2u}{d\eta^2}+\frac{1}{\eta}\frac{du}{d\eta}-\frac{\eta^2}{4}u-\frac{1}{\eta^2}\left(l^2+l\eta_o^2+\frac{\eta_o^4}{4}\right)u+\left(l+\frac{\eta_o^2}{2}+2\varepsilon\right)u=0. \tag{3.11}$$

Introducing the equations $l_{\text{eff}} = l + \eta_o^2/2$, $2\xi = l_{\text{eff}} + 2\varepsilon$ and the substitutions $u(\eta) = \eta^{|l_{\text{eff}}|}e^{-\eta^2/4}G(\eta)$ and $y = \eta^2/2$, the previous equation takes the form of Kummer's differential equation

$$y\frac{d^2G}{dy^2} + [|l_{\text{eff}}| + 1 - y]\frac{dG}{dy} - \left[\frac{1 + |l_{\text{eff}}| - 2\xi}{2}\right]G = 0. \tag{3.12}$$

Using the notation of Magnus *et al* [26], the linearly independent solutions of Kummer's differential equation are given by

$$G^{(1)}(y) = A^{(1)}{}_1F_1(a; c; y) \tag{3.13}$$

and

$$G^{(2)}(y) = A^{(2)}y^{1-c}{}_1F_1(a - c + 1; 2 - c; y), \tag{3.14}$$

where $A^{(1)}$ and $A^{(2)}$ are normalisation constants, ${}_1F_1(a; c; y)$ is a confluent hypergeometric function, $a = 1 + |l_{\text{eff}}| - 2\xi/2$ and $c = |l_{\text{eff}}| + 1$. Eq. 3.13 and Eq. 3.14 are solutions to Kummer's differential equation only if c is not an integer or zero. This holds when $r_o^2/2l_B^2 \neq n$, where n is an integer or zero, and is the case dealt with in this section. It will be shown in the next section that for the special case when $r_o^2/2l_B^2 = n$, the solutions are similar to those obtained for a system with a magnetic field overshoot at r_o. Substituting the explicit form for a and c and using the fact that $u(\eta) = \eta^{|l_{\text{eff}}|}e^{-\eta^2/4}G(\eta)$, the final form for the wave function in the region $r > r_o$ is found to be

$$\begin{aligned} u_{\eta>\eta_o}(\eta) &= \eta^{|l_{\text{eff}}|}e^{-\eta^2/4}\left[A^{(1)}{}_1F_1\left(\frac{1 + |l_{\text{eff}}| - 2\xi}{2}; |l_{\text{eff}}| + 1; \frac{\eta^2}{2}\right)\right. \\ &+ \left. A^{(2)}\left(\frac{2}{\eta^2}\right)^{|l_{\text{eff}}|}{}_1F_1\left(\frac{1 - |l_{\text{eff}}| - 2\xi}{2}; 1 - |l_{\text{eff}}|; \frac{\eta^2}{2}\right)\right]. \end{aligned} \tag{3.15}$$

To determine the single electron energy of the system, the wave functions (given by Eq. 3.10 and Eq. 3.15), and their derivatives are matched at the boundary

($r = r_o$). This ensures that the wave function that describes the system, and its slope, are continuous. The continuity relations are

$$u_{r<r_o}(r)|_{r=r_o} = u_{r>r_o}(r)|_{r=r_o} \tag{3.16}$$

and

$$\frac{d}{dr}u_{r<r_o}(r)\bigg|_{r=r_o} = \frac{d}{dr}u_{r>r_o}(r)\bigg|_{r=r_o}. \tag{3.17}$$

To eliminate the unknown quantities, $A^{(1)}$, $A^{(2)}$ and C, the continuity relations are solved simultaneously. Substituting Eq. 3.10 and Eq. 3.15 into Eq. 3.17, performing the differentiations and dividing the resulting equation by $A^{(1)}$, gives an equation with terms containing $C/A^{(1)}$ and $A^{(2)}/A^{(1)}$. Ultimately this equation is rearranged to give an expression for the single electron energy (see Eq. 3.22), however the unknown quantities, $C/A^{(1)}$ and $A^{(2)}/A^{(1)}$, first must be determined. The ratio $C/A^{(1)}$ is obtained by substituting Eq. 3.10 and Eq. 3.15 into the first continuity relation (Eq. 3.16), giving

$$\begin{aligned}\frac{C}{A^{(1)}} &= \frac{e^{-\eta_o^2/4}}{J_l(\sqrt{2\varepsilon}\eta_o)}\left[\eta_o^{|l_{\text{eff}}|}\,{}_1F_1\left(\frac{1+|l_{\text{eff}}|-2\xi}{2};|l_{\text{eff}}|+1;\frac{\eta_o^2}{2}\right)\right. \\ &+ \left.\frac{A^{(2)}}{A^{(1)}}\left(\frac{2}{\eta_o}\right)^{|l_{\text{eff}}|}\,{}_1F_1\left(\frac{1-|l_{\text{eff}}|-2\xi}{2};1-|l_{\text{eff}}|;\frac{\eta_o^2}{2}\right)\right].\end{aligned} \tag{3.18}$$

An equation for the ratio $A^{(2)}/A^{(1)}$ is obtained by demanding that the wave function given by Eq. 3.15 vanishes for $\eta \to \infty$. In order to fulfill this requirement, the asymptotic form of the confluent hypergeometric function for large η is introduced. From Magnus *et al* [26], the asymptotic form of the confluent hypergeometric function is

$${}_1F_1(a;c;y) = \frac{\Gamma(c)}{\Gamma(a)}e^y y^{a-c}, \tag{3.19}$$

where $\Gamma(a)$ is a gamma function. On substituting this result into Eq. 3.15 it is

found that

$$u_{\eta>\eta_o}(\eta) = \eta^{|l_{\rm eff}|}e^{-\eta^2/4}\left[A^{(1)}\frac{\Gamma(|l_{\rm eff}|+1)}{\Gamma\left(\frac{1+|l_{\rm eff}|-2\xi}{2}\right)}e^{\eta^2/2}\left(\frac{\eta^2}{2}\right)^{-\left(\frac{1+|l_{\rm eff}|+2\xi}{2}\right)}\right.$$
$$\left. + A^{(2)}\left(\frac{2}{\eta^2}\right)^{|l_{\rm eff}|}\frac{\Gamma(1-|l_{\rm eff}|)}{\Gamma\left(\frac{1-|l_{\rm eff}|-2\xi}{2}\right)}e^{\eta^2/2}\left(\frac{\eta^2}{2}\right)^{-\left(\frac{1-|l_{\rm eff}|+2\xi}{2}\right)}\right]. \quad (3.20)$$

To satisfy the condition of the wave function vanishing for a large argument, the right hand side of Eq. 3.20 is set equal to zero. It is found that both terms in the resulting equation diverge as $\eta \to \infty$. The term with factor $A^{(1)}$ diverges to a large positive value and the term with factor $A^{(2)}$ diverges to a large negative value. However, the divergent factors cancel exactly when the ratio of the normalisation constants is

$$\frac{A^{(2)}}{A^{(1)}} = -\frac{\Gamma(|l_{\rm eff}|+1)\Gamma\left(\frac{1-|l_{\rm eff}|-2\xi}{2}\right)}{\Gamma\left(\frac{1+|l_{\rm eff}|-2\xi}{2}\right)\Gamma(1-|l_{\rm eff}|)}. \quad (3.21)$$

The final form of the equation used to determine the single electron energy is obtained as described in the paragraph preceeding Eq. 3.18 and with $a_1 = 1+|l_{\rm eff}|-2\xi/2$, $c_1 = |l_{\rm eff}|+1$, $a_2 = 1-|l_{\rm eff}|-2\xi/2$ and $c_2 = 1-|l_{\rm eff}|$ this is given by

$$\varepsilon = \frac{1}{2}\left(\frac{J_l(\sqrt{2\varepsilon}\eta_o)}{J_{l+1}(\sqrt{2\varepsilon}\eta_o)}\right)^2\left\{\frac{l-|l_{\rm eff}|}{\eta_o}+\frac{\eta_o}{2}\right.$$
$$\left. - \Lambda\left[{}_1F_1\left(a_1;c_1;\frac{\eta_o^2}{2}\right)+\frac{A^{(2)}}{A^{(1)}}\left(\frac{2}{\eta_o^2}\right)^{|l_{\rm eff}|}{}_1F_1\left(a_2;c_2;\frac{\eta_o^2}{2}\right)\right]^{-1}\right\}^2, \quad (3.22)$$

where

$$\Lambda = \frac{a_1\eta_o}{c_1}{}_1F_1\left(a_1+1;c_1+1;\frac{\eta_o^2}{2}\right)+\frac{A^{(2)}}{A^{(1)}}\left(\frac{2}{\eta_o^2}\right)^{|l_{\rm eff}|}$$
$$\times\left[\frac{a_2\eta_o}{c_2}{}_1F_1\left(a_2+1;c_2+1;\frac{\eta_o^2}{2}\right)-\frac{2|l_{\rm eff}|}{\eta_o}{}_1F_1\left(a_2;c_2;\frac{\eta_o^2}{2}\right)\right]. \quad (3.23)$$

Eq. 3.22 is solved using a numerical routine based on a bisection method [25]. A separate routine is used to bracket the root, with the energy value of the initial

end point used as an initial guess at the energy. The bracketed energy range is then bisected until a value of the energy accurate to machine precision (roughly 1×10^{-16}) is obtained. To evaluate the confluent hypergeometric function, the relation

$$ {}_1F_1(a;c;y) = \sum_{n=0}^{\infty} \frac{(a)_n}{(c)_n} \frac{y^n}{n!} \tag{3.24} $$

is used, where $(a)_n = \Gamma(a+n)/\Gamma(a)$ is Pochhammer's symbol. The series is evaluated for up to a maximum of $n = 1000$, and is truncated if the difference between two consecutive terms is less than 1×10^{-20}.

3.1.3 Results

In this section the theoretical methods described in the previous sections are used to determine the single electron energies of a magnetic quantum dot system without a magnetic field overshoot at r_o. There are two main aims of the results presented in this section. The first is to compare the two numerical methods that have been described, and to show that both methods give the same results. The second aim is to illustrate various interesting properties of the system, such as the energy as a function of the angular momentum quantum number and the magnetic quantum dot radius. All the results obtained are for a GaAs system, this material has an effective mass, m^*, of $0.067m_e$, where m_e is the mass of the electron, and a relative permittivity of 12.4.

Figure 3.1 shows the single electron energy as a function of the angular momentum quantum number, l, for a magnetic field, $B_z = 5$ T and a magnetic quantum dot radius, $r_o = 10$ nm. The crosses are the results obtained using the matching procedure, and the diamonds are the results obtained using the numerical diagonalisation method. To calculate the results using the numerical

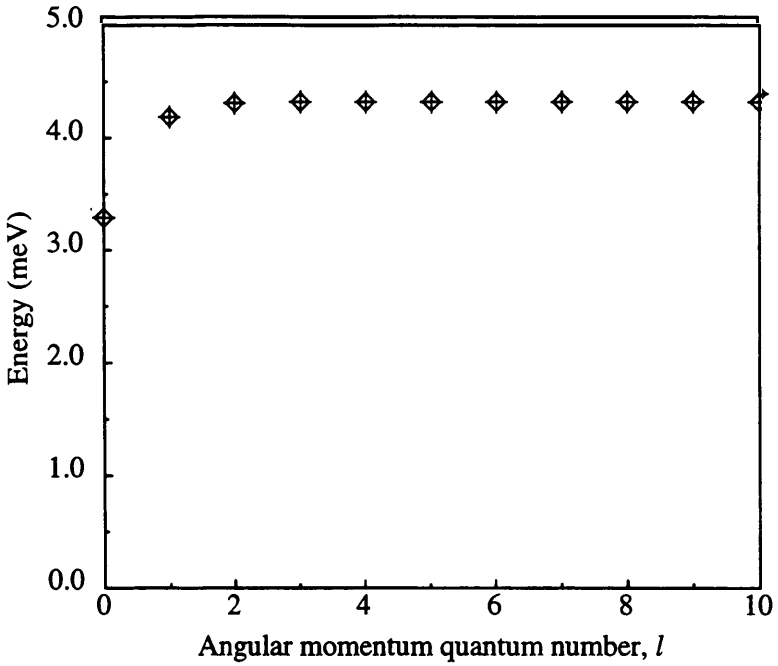

Figure 3.1: Energy as a function of angular momentum quantum number, l, for magnetic field , $B_z = 5$ T and $r_o = 10$ nm. The diamonds indicate results calculated using the numerical diagonalisation technique and the crosses indicate results calculated using the matching procedure.

diagonalisation method, three Landau levels (corresponding to four basis states) are included in the calculation. To ascertain that the energies have converged, the number of Landau levels included in the calculation is increased by one. This is found to shift the energy at $l = 0$ by roughly 0.3×10^{-3} meV, and the energy at $l = 10$ by roughly 4×10^{-5} meV, equivalent to an error of 0.01% and 0.001% respectively. It is clear that the energies obtained using the numerical diagonalisation method and the matching procedure agree very well. Indeed, the points obtained using each method are almost indistinguishable throughout the l range. The figure shows that as l increases, the energy gradually increases to a constant value at roughly $l = 2$ and remains constant as l increases further. The

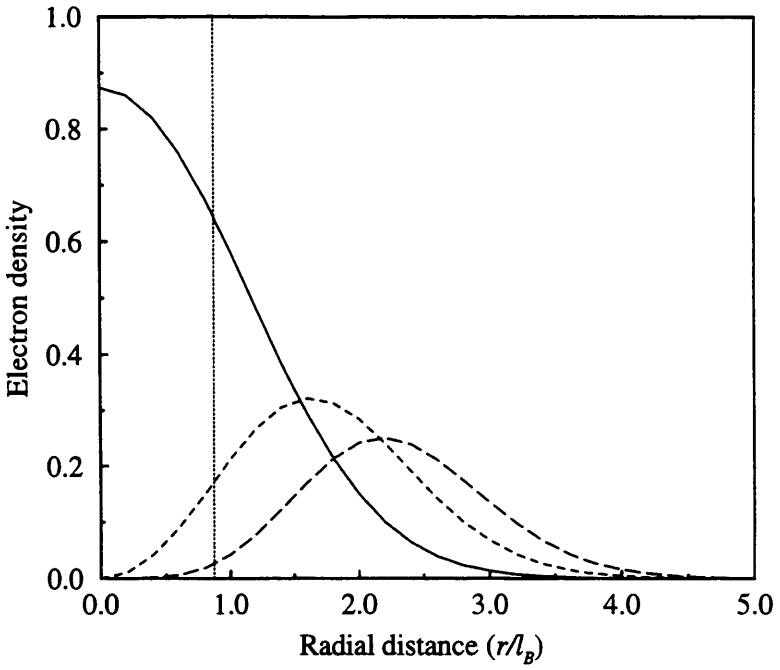

Figure 3.2: Electron density as a function of radial distance for $B_z = 5$ T, $r_o = 10$ nm, $l = 0$ (solid curve), $l = 1$ (short dashed curve) and $l = 2$ (long dashed curve). The vertical dotted line indicates the position of r_o.

reason for the gradual increase in energy as l increases from $l = 0$ to $l = 2$ can be explained by investigating how the electron density varies with increasing l. Figure 3.2 shows how the electron density varies as a function of radial distance for $B_z = 5$ T, $r_o = 10$ nm, $l = 0$ (solid curve), $l = 1$ (short dashed curve) and $l = 2$ (long dashed curve). For $l = 0$ (solid line in the figure) the electron wave function is localised at the centre of the magnetic quantum dot. This is the magnetic field free region and hence the energy of the electron is lower than in the region where a magnetic field is present. If the electron is excited into a higher angular momentum state, its orbital radius correspondingly increases [27] and the electron wave function becomes localised away from the centre of the magnetic quantum dot. The vertical dotted line indicates the position of r_o. It

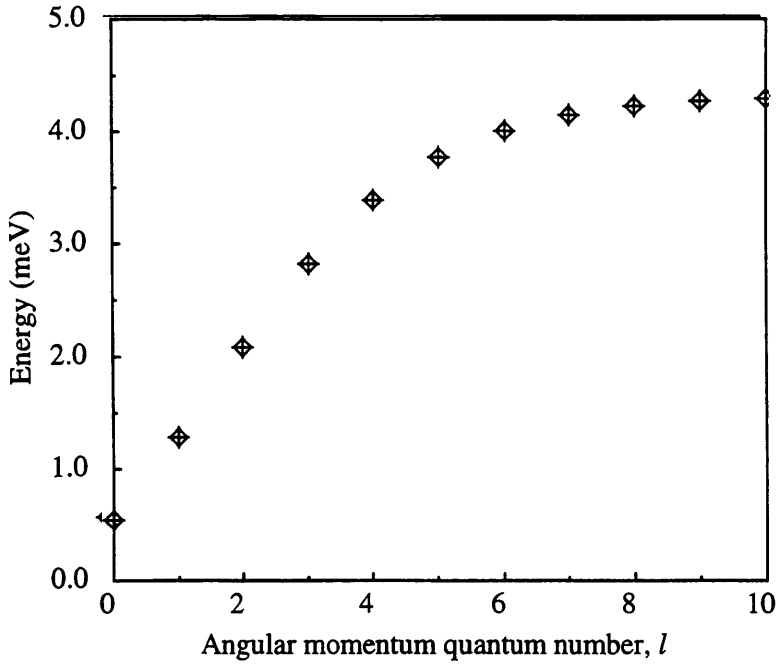

Figure 3.3: Same as Fig. 3.1 but for a magnetic quantum dot of radius $r_o = 60$ nm.

is seen for $l = 1$ and $l = 2$, that most of the electron wave function is localised in the region outside the magnetic quantum dot and so the electron energy increases due to the magnetic field. As l becomes large all of the electron wave function becomes localised outside the magnetic quantum dot, and the energy becomes constant with a value equal to the energy of the zeroth Landau level ($\hbar\omega_c/2$).

The electron energy as a function of l, for $B_z = 5$ T and $r_o = 60$ nm is shown in figure 3.3. The crosses indicate the results obtained using the matching procedure, and the diamonds indicate the results obtained using the numerical diagonalisation method. Seven Landau levels are included in the numerical diagonalisation calculation, to obtain energies that are accurate to roughly 0.0003% for $l = 0$ and roughly 0.0002% for $l = 10$. Again, it is clear that energies obtained using the numerical diagonalisation method and the matching procedure agree well. The figure shows similar features to figure 3.1, in that the

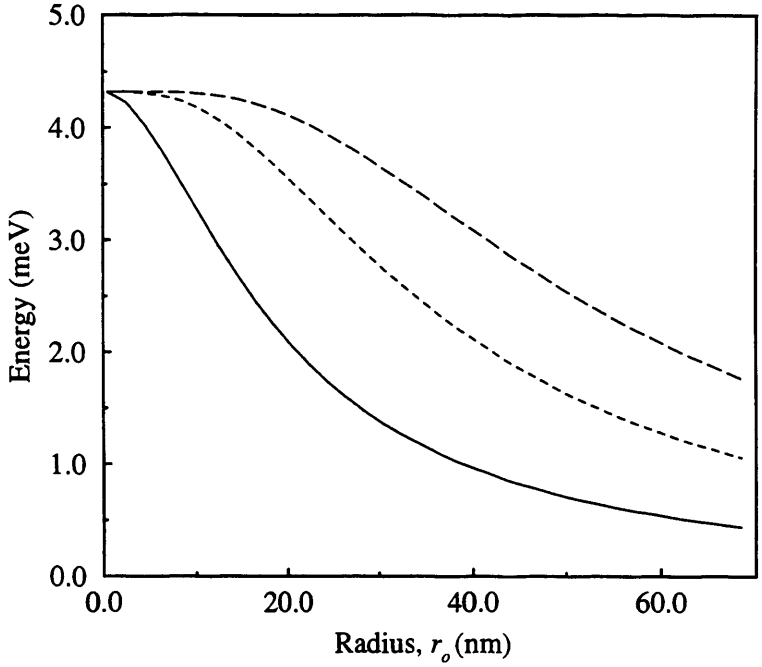

Figure 3.4: Energy as a function of magnetic quantum dot radius, r_o, for $B_z = 5$ T, $l = 0$ (solid curve), $l = 1$ (short dashed curve) and $l = 2$ (long dashed curve).

energy gradually increases to a constant value as l increases. Again, for $l = 0$ the electron wave function is localised at the centre of the magnetic quantum dot. The energy for $l = 0$ is lower for a system with $r_o = 60$ nm as compared to a system with $r_o = 10$ nm because more of the electron wave function is localised in the magnetic field free region. As l increases, the energy increases because gradually more of the electron wave function becomes localised outside of the magnetic quantum dot. When $l > 9$ the energy becomes constant with a value again equal to the energy of the zeroth Landau level, because all of the electron wave function is localised outside the magnetic quantum dot.

Figure 3.4 shows the energy as a function of magnetic quantum dot radius. The results are obtained for a system with $B_z = 5$ T and the energy is calculated using the matching procedure. For $r_o = 0$ nm the system consists of a constant

magnetic field, hence the energy is equal to the energy of the zeroth Landau level for all values of the angular momentum quantum number. As r_o increases, the energy decreases steadily because more of the electron wave function becomes localised in the magnetic field free region, hence the electron energy due to the magnetic field decreases. For large r_o, the energy tends to zero, which is the free electron energy, because all of the electron wave function is localised inside the magnetic quantum dot.

3.2 A System with a Magnetic Field Overshoot

3.2.1 Calculation of the Single Electron Matrix Elements

In this section the single electron matrix elements given by Eq. 2.11 are calculated explicitly for a system with a magnetic field overshoot at r_o. The method used is exactly the same as for the system without a magnetic field overshoot.

The hamiltonian in the magnetic field free region ($r < r_o$) is the same as for the system without a magnetic field overshoot and is given by Eq. 3.1. After substituting the vector potential given by Eq. 2.8 into Eq. 2.2, and again with $\mathbf{L} = -\hbar l$ and $\omega_c = eB_z/m^*$, the hamiltonian for the region with magnetic field ($r > r_o$) is found to be

$$h_{r>r_o} = -\frac{\hbar^2}{2m^*}\nabla^2 + \frac{m^*\omega_c^2 r^2}{8} - \frac{\hbar\omega_c l}{2} + g^*\mu_B B_z S_z. \tag{3.25}$$

All the terms in this equation are also present in Eq. 3.4. This is because the vector potential given by Eq. 2.7, consists of two terms, the first equal to Eq. 2.8. To determine the final form for the single electron matrix elements, the hamiltonian inside the magnetic quantum dot (Eq. 3.1), the hamiltonian outside

the magnetic quantum dot (Eq. 3.25), the single particle wave function (Eq. 2.13) and the dimensionless variable, $x = r^2/2l_B^2$ are substituted into Eq. 2.11. The resulting form for the matrix element is

$$\begin{aligned}\langle i|h|j\rangle &= \delta_{ll'}\left\{\left[\frac{\hbar\omega_c}{2}\left((2n+|l|+1)-l\right)+g^*\mu_B B_z S_z\right]\delta_{nn'}\right. \\ &+ \left[\frac{\hbar\omega_c l}{2}-g^*\mu_B B_z S_z\right]\lambda_n\lambda_{n'}\int_0^{x_o} e^{-x}x^{|l|}L_{n'}^{|l|}(x)L_n^{|l|}(x)dx \\ &- \left.\frac{\hbar\omega_c}{4}\lambda_n\lambda_{n'}\int_0^{x_o} e^{-x}x^{|l|+1}L_{n'}^{|l|}(x)L_n^{|l|}(x)dx\right\}. \qquad (3.26)\end{aligned}$$

The integrals in this equation are evaluated numerically using the modified Gauss-Laguerre integration routine discussed in section 3.1.1, with each of the integrands evaluated at 32 points. Again, the results are verified using Maple, and it is found that the results are accurate to roughly seven decimal places.

3.2.2 Matching Procedure

The procedure followed in this section is similar to that described for a system without a magnetic field overshoot at r_o. For the region $r < r_o$, the hamiltonian is given, as in the previous case, by Eq. 3.1, so the wave function in this region is given by Eq. 3.10. The hamiltonian in the region $r > r_o$ is now given by Eq. 3.25. Neglecting the Zeeman energy term, substituting Eq. 3.25, $\psi_{r>r_o}(r,\phi) = u_{r>r_o}e^{-il\phi}$, and the dimensionless quantities $\varepsilon = E/\hbar\omega_c$ and $\eta = r/l_B$ into the Schrödinger equation gives

$$\frac{d^2u}{d\eta^2}+\frac{1}{\eta}\frac{du}{d\eta}-\frac{\eta^2}{4}u-\frac{l^2}{\eta^2}u+2\xi u=0, \qquad (3.27)$$

where $2\xi = l + 2\varepsilon$. The form of this equation is very similar to Eq. 3.11. The difference between the two equations is that in Eq. 3.11, l_{eff} replaces l, other than this the equations are identical. Substituting $u(\eta) = \eta^{|l|}e^{-\eta^2/4}G(\eta)$ and $y = \eta^2/2$

into the previous equation gives Kummer's differential equation

$$y\frac{d^2G}{dy^2} + [|l| + 1 - y]\frac{dG}{dy} - \left[\frac{1 + |l| - 2\xi}{2}\right]G = 0. \tag{3.28}$$

It is at this point which the two methods for obtaining the energies become dissimilar. The solution to the Eq. 3.28 is no longer given by Eq. 3.13 and Eq. 3.14, because l is an integer. If l is an integer then either $G^{(1)}(y) = G^{(2)}(y)$, with $G^{(1)}(y)$ given by Eq. 3.13 and $G^{(2)}(y)$ given by Eq. 3.14, or one of these solutions is not defined [28]. This is also the case for a system without a magnetic field overshoot at r_o when $r_o^2/2l_B^2 = n$, in this case l_{eff} is an integer. In order to give a general solution to the differential equation it is necessary to find another linearly independent solution. Luke [28] gives a third linearly independent solution as

$$G^{(3)}(y) = A^{(3)}U(a; c; y), \tag{3.29}$$

where $A^{(3)}$ is a normalisation constant, $a = 1 + |l| - 2\xi/2$ and $c = |l| + 1$. The general solution to Eq. 3.28 is then given by

$$u_{\eta>\eta_o}(\eta) = \eta^{|l|}e^{-\eta^2/4}\left[A^{(1)}{}_1F_1(a; c; y) + A^{(3)}U(a; c; y)\right]. \tag{3.30}$$

The wave function given by Eq. 3.30 is required to vanish as $\eta \to \infty$. Because the confluent hypergeometric function diverges as $\eta \to \infty$, $A^{(1)}$ is set to zero. The asymptotic form of the second term is $U(a; c; y) = y^{-a}$ [26], so provided a is positive, this term converges. The required solution for the region $r > r_o$ is then given by

$$u_{\eta>\eta_o}(\eta) = \eta^{|l|}e^{-\eta^2/4}A^{(3)}U\left(\frac{1 + |l| - 2\xi}{2}; |l| + 1; \frac{\eta^2}{2}\right). \tag{3.31}$$

To determine the single electron energies of the system, the continuity relations (Eq. 3.16 and Eq. 3.17) are used. By solving the continuity equations simultaneously, the unknown quantities, $A^{(3)}$ and C can be eliminated, and the

equation used to determine the single electron energies of the system is found to be

$$\varepsilon = \frac{1}{2}\left(\frac{J_l(\sqrt{2\varepsilon}\eta_o)}{J_{l+1}(\sqrt{2\varepsilon}\eta_o)}\right)^2\left[\frac{l-|l|}{\eta_o}+\frac{\eta_o}{2}+a\eta_o\frac{U\left(a+1;c+1;\frac{\eta_o^2}{2}\right)}{U\left(a;c;\frac{\eta_o^2}{2}\right)}\right]^2. \tag{3.32}$$

This equation is solved using the bisection method, that has been discussed previously. In order to evaluate $U(a;c;y)$ numerically, the function is written in its alternative form $y^{-a}{}_2F_0(a;1+a-c;-1/y)$ [29]. To write the hypergeometric function as an infinite series, the generalised hypergeometric series [26] is used

$${}_pF_q(\alpha_1,\alpha_2,\cdots,\alpha_p;\beta_1,\beta_2,\cdots,\beta_q;z) = \sum_{n=0}^{\infty}\frac{(\alpha_1)_n\cdots(\alpha_p)_n}{(\beta_1)_n\cdots(\beta_q)_n}\frac{z^n}{n!}. \tag{3.33}$$

On substituting the parameters $p=2$, $q=0$, $\alpha_1=a$, $\alpha_2=1+a-c$ and $z=-1/y$ into the previous equation it is found that the series diverges for all $z\neq 0$ [26]. Because the series is an infinite power series in $-1/y$, where $y=\eta^2/2$ and $\eta=r/l_B$, the functions $U(a;c;\eta_o^2/2)$ and $U(a+1;c+1;\eta_o^2/2)$ cannot be evaluated for small r_o, by the use of a numerical series. To overcome this problem, the ratio of the functions is calculated. It is conjectured that the divergent factors associated with the individual functions cancel, and therefore the ratio is expected to be well behaved.

To obtain an equation for the ratio $R=U(a+1;c+1;y)/U(a;c;y)$, the following relation, obtained from Magnus [26] is divided by $U(a;c;y)$

$$\frac{d}{dy}U(a;c;y)+aU(a+1;c+1;y)=0, \tag{3.34}$$

giving

$$R=-\frac{1}{aU(a;c;y)}\frac{d}{dy}U(a;c;y). \tag{3.35}$$

By differentiating Eq. 3.35 with respect to y, and substituting the result, along with Eq. 3.35 into Kummers differential equation, an equation for R can be found

and is given by

$$\frac{dR}{dy} + \frac{1}{y} + (c - y)\frac{R}{y} - R^2 a = 0. \tag{3.36}$$

This equation has the form of a Riccati equation [30], and is solved using a Runge-Kutta routine from the NAG library. The initial value of R is calculated using the generalised hypergeometric series for a large argument ($y_{\text{initial}} = 100$). For an argument of this size the hypergeometric series converges, and the series is evaluated in a similar manner to the confluent hypergeometric series. The numerical solution to the Riccati equation is then obtained by a step-by-step calculation, and values of R are calculated at specified intervals between y_{initial} and the desired end point, $y_{\text{end}} = r_o^2/2$. The interval at which R is calculated, is determined by a parameter ($= (y_{\text{end}} - y_{\text{initial}})/n$, where $n = 2000$ is the number of points at which R is evaluated) in the routine. The accuracy of the solution is controlled by a tolerance parameter in the NAG routine. The value of this parameter is set to 1×10^{-8} for all the calculations performed in this chapter, resulting in a solution accurate to at least seven decimal places.

For values of r_o less than approximately 30 nm, it is found that R as a function of the argument, y, contains a number of singularities, depending on the values of the parameters a and c. Figure 3.5 shows how the ratio, R, varies with argument, y, for $a = -1.5$, $c = 5$ and $r_o = 10$ nm. In order to calculate the ratio at y_{end} (~ 0.38 in this case), the routine is required to calculate values of R close to a singularity. The numerical routine used to determine the solution of the differential equation (Eq. 3.36) fails on calculating large positive or large negative values of R. To overcome this problem, if R is large, a differential equation with a solution, $1/R$, is solved. Substituting $R' = 1/R$ into Eq. 3.36, the differential

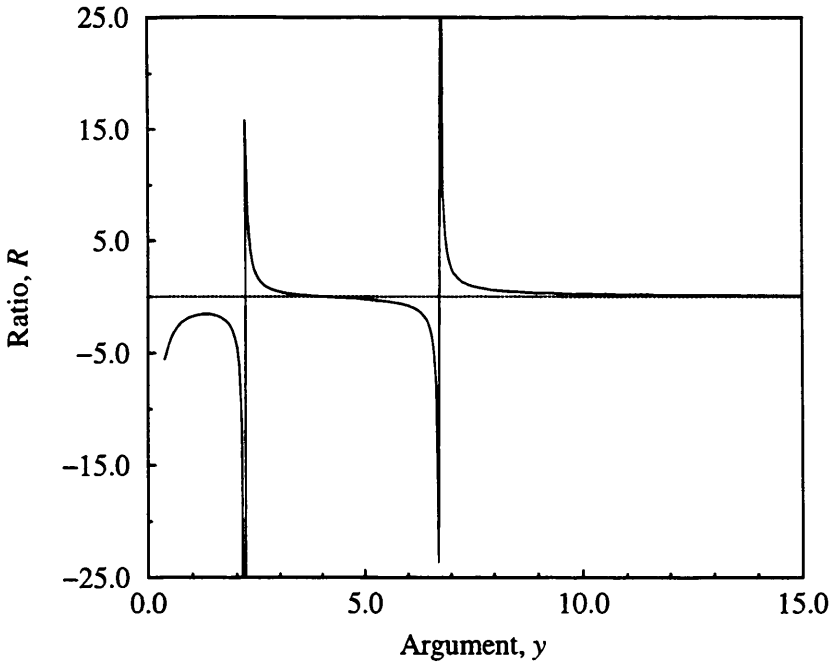

Figure 3.5: Ratio, R, as a function of argument, y, for $a = -1.5$, $c = 5$ and $r_o = 10$ nm.

equation for R' is found to be

$$\frac{dR'}{dy} + a - \frac{R'^2}{y} - (c - y)\frac{R'}{y} = 0. \tag{3.37}$$

As R becomes large, R' becomes small, and the solution of Eq. 3.37 can be determined using the numerical routine. If $|R| \leq 0.08$ Eq. 3.36 is solved for R, otherwise the differential equation given by Eq. 3.37 is solved for R'.

3.2.3 Results

In this section the theoretical methods described in the previous sections are used to determine the single electron energies of a magnetic quantum dot with a magnetic field overshoot at r_o. The results presented are compared with the results obtained for a system without a magnetic field overshoot at r_o, and contrasts are made. Again, all the results calculated are for a GaAs system.

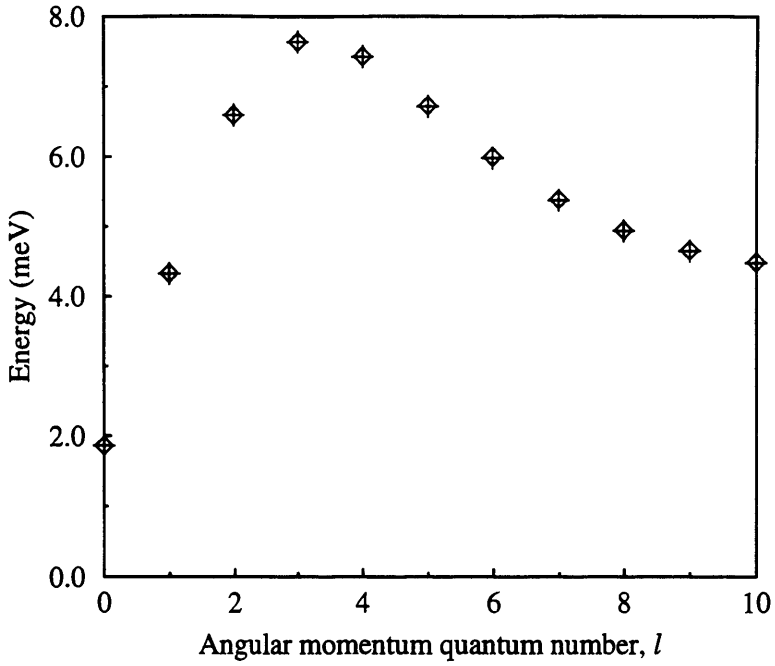

Figure 3.6: Energy as a function of angular momentum quantum number, l, for magnetic field $B_z = 5$ T and $r_o = 35$ nm. The diamonds indicate results calculated using the numerical diagonalisation method and the crosses indicate results calculated using the matching procedure.

Figure 3.6 shows the single electron energy as a function of angular momentum quantum number, l, for a system with a magnetic field overshoot at r_o. The results are for a system in which the magnetic field, $B_z = 5$ T, and the radius, $r_o = 35$ nm. The crosses are the results obtained using the matching procedure, and the diamonds are the results obtained using the numerical diagonalisation method. To obtain converged energy values, six Landau levels are included in the numerical diagonalisation calculation. This gives an accuracy of $\sim 0.017\%$ for $l = 0$ and $\sim 0.08\%$ for $l = 10$. Again, the figure shows a good agreement between the results obtained using the numerical diagonalisation calculation and the results obtained using the matching technique. It is observed that the energy increases steadily with increasing angular momentum quantum number. As l

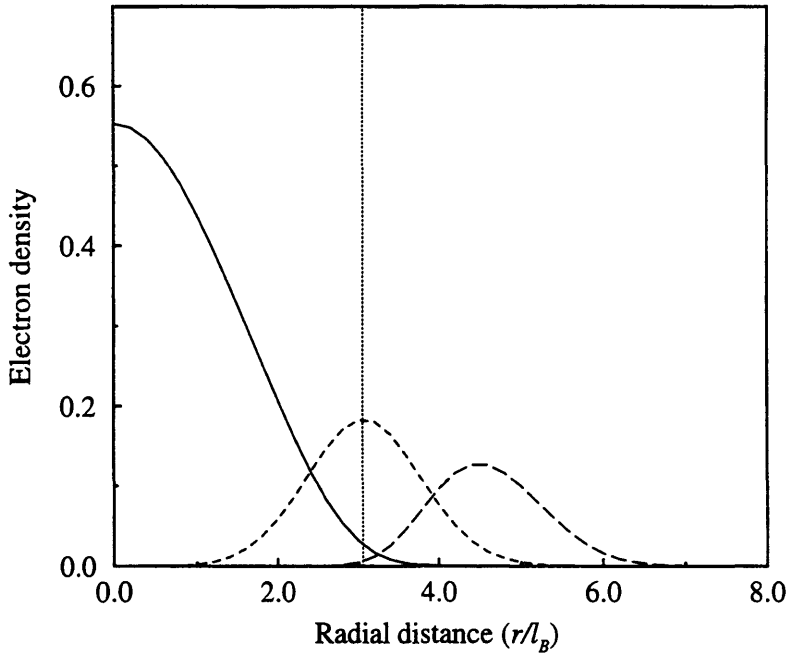

Figure 3.7: Electron density as a function of radial distance for $B_z = 5$ T, $r_o = 35$ nm, $l = 0$ (solid curve), $l = 3$ (short dashed curve) and $l = 10$ (long dashed curve). The vertical dotted line indicates the position of r_o.

increases further, the energy reaches a maximum and then gradually begins to decrease before reaching a constant value. In contrast to the system without a magnetic field overshoot at r_o, there exists a maximum in the electron energy as a function of l. The same effect has also been reported by Peeters *et al* [9] and also by Reijniers *et al* [10]. The cause of the energy maximum is explained in terms of the effective potential of the systems, however, some insight into the effect can be gained by investigating the electron density. Figure 3.7 shows how the electron density varies as a function of radial distance for $B_z = 5$ T, $r_o = 35$ nm, $l = 0$ (solid curve), $l = 3$ (short dashed curve) and $l = 10$ (long dashed curve). As expected for $l = 0$ the electron wave function is localised at the centre of the magnetic quantum dot. It is seen in figure 3.6 that the maximum in the energy,

corresponds to an angular momentum quantum number of $l = 3$. From figure 3.7, it is seen that for $l = 3$ (short dashed curve in the figure), the maximum of the electron wave function is situated a distance very close to the radius, r_o, away from the centre of the magnetic quantum dot (the vertical dotted line indicates the position of r_o). The form of the effective potential of the system at r_o is found from Eq. 3.25 to be $V_{\text{eff}} = m^*\omega_c^2 r^2/8$, hence at $r = r_o$, $V_{\text{eff}} = m^*\omega_c^2 r_o^2/8$. By comparing this effective potential with the effective potential of the system without a magnetic field overshoot at r_o, the reason for the energy increase in figure 3.6 becomes apparent. From Eq. 3.4, the effective potential for the system without a magnetic field overshoot is

$$V_{\text{eff}} = \frac{m^*\omega_c^2 r^2}{8} + \frac{\hbar\omega_c l r_o^2}{2r^2} + \frac{m^*\omega_c^2 r_o^4}{8r^2}, \tag{3.38}$$

therefore at $r = r_o$,

$$V_{\text{eff}} = \frac{m^*\omega_c^2 r_o^2}{4} + \frac{\hbar\omega_c l}{2}. \tag{3.39}$$

The two terms in this equation cancel exactly with existing constants in the hamiltonian (Eq. 3.4), resulting in an energy that is less than the energy for the corresponding system with a magnetic field overshoot, and this explains the energy maximum in figure 3.6. As l increases further, the electron wave function becomes more localised in the region outside the magnetic quantum dot, where the magnetic field is constant, and hence the energy gradually decreases and eventually becomes equal to the energy of the zeroth Landau level.

This effect can also be seen in figure 3.8. The figure shows the energy as a function of magnetic quantum dot radius, r_o, for $B_z = 5$ T, $l = 0$ (solid curve), $l = 1$ (short dashed curve) and $l = 2$ (long dashed curve). The energy is calculated using the numerical diagonalisation method. For $r_o = 0$ nm the system consists of a constant magnetic field, hence the energy is equal to the energy of the zeroth

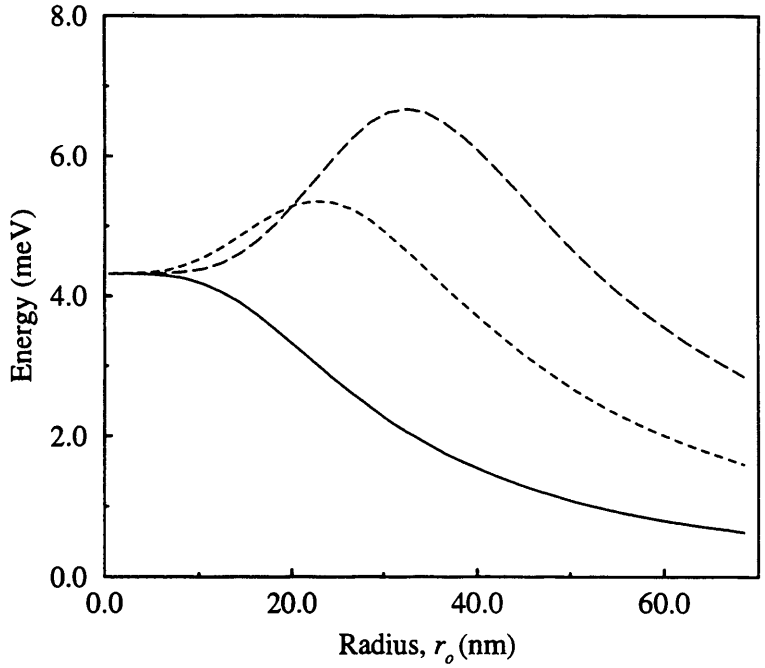

Figure 3.8: Energy as a function of magnetic quantum dot radius, r_o, for $B_z = 5$ T, $l = 0$ (solid curve), $l = 1$ (short dashed curve) and $l = 2$ (long dashed curve).

Landau level for all values of the angular momentum quantum number. For $l > 0$ the energy as a function of r_o exhibits a maximum. Again, the maxima in the energies occur when the maximum of the electron wave function for a given l, is situated a distance very close to the radius, r_o, away from the centre of the magnetic quantum dot. Therefore the energy is increased in the way described previously. As r_o increases further, most of the electron wave function becomes localised in the magnetic field free region, and hence the energy decreases.

3.3 Comparison of the Numerical Methods

In this section the advantages and disadvantages associated with each numerical method are described, and the factors that influence the choice of which numerical routine to use to calculate the single electron energies are discussed.

The computational time required to perform a numerical calculation is a crucial factor that must be considered carefully before undertaking a complex numerical calculation. Fortunately, both the numerical routines used to calculate the results given in this chapter are computationally inexpensive. For instance, the computational time required to obtain the data shown in figure 3.6 is roughly ten seconds using a HP 735 workstation, using the numerical diagonalisation method, while the time to calculate the data using the matching procedure is roughly five minutes. To obtain the data shown in figure 3.1 and figure 3.3, the numerical diagonalisation routine again takes roughly ten seconds, while the time taken to calculate the data using the matching procedure decreases significantly, taking approximately twenty seconds. The increase in CPU time required to calculate the data when the system has a magnetic field overshoot, is attributed to the fact that this routine evaluates a generally more complicated function. It is thought that a significant portion of this time difference is required to the calculate the ratio of the hypergeometric functions, R.

Several other factors also influence the choice of routine to use to calculate the energies of the systems. The accuracy of the calculated results is very important. In the numerical diagonalisation routine this is determined by the number of Landau levels included in the calculation. For a calculation involving one electron, the errors associated with the data shown in figure 3.1 are better than 0.01%. If a more accurate solution is required, the inclusion of more Landau levels in the calculation does not increase the CPU time greatly. The results calculated using the matching procedure are shown to be accurate to roughly machine precision. If greater accuracy is required, the number of bisections the routine performs to obtain a value for the energy can be increased. However, this may increase the

computational time required to perform a calculation.

The final factor that is discussed, is the programming effort that is required to write the individual programs. It is found that the routines based on the matching procedure are the less laborious to write. The length of each of these routines, written using Fortran 77, is roughly 500 lines of code. However, the programming effort necessary for the numerical diagonalisation routine is significantly greater, and the total length of this routine is over 3000 lines of code. Therefore a great amount of effort is required to write the numerical diagonalisation routine. However, this method is readily adapted to include more electrons, a fact that is exploited in subsequent chapters.

Chapter 4

Interacting Electrons in a Magnetic Quantum Dot

In this chapter a magnetic quantum dot containing more than one electron is investigated, and the new physics that arises as a consequence of the electron-electron interaction is discussed. The chapter is organised as follows. First, a review of some of the previous work in this field is given. The Coulomb matrix elements that are needed for the numerical diagonalisation calculation are then determined, and the computational problems encountered on attempting to evaluate them are discussed. In the next section, the possibility of a magnetic quantum dot confining interacting electrons is investigated. A magnetic quantum dot containing two interacting electrons is considered, and the question of how to determine if the magnetic quantum dot is able to confine the electrons is answered. In the following section, results are presented for a magnetic quantum dot containing two interacting electrons, showing regions where confinement of the electrons is possible as a function of the magnetic quantum dot radius and the confining magnetic field. The theoretical model of the system is then modified to account for the three dimensional motion of the electrons in a more

realistic system. The results are compared with the results obtained for the two dimensional system. Finally, the effect of adding a third electron to the system is investigated and the results are compared with the results calculated for the two electron system.

4.1 Previous Work

To date, the author is unaware of any work concerning magnetic quantum dots, in which the electron-electron interaction is included explicitly in calculations. Peeters *et al* [9] and Reijniers *et al* [10] have considered non-interacting electrons in a magnetic quantum dot. Through energy considerations, they conjectured that an electron will only be situated in the magnetic quantum dot, if its energy is lower than in the region outside the magnetic quantum dot ($\hbar\omega_c/2$ if the Zeeman energy is neglected). For a system without a magnetic field overshoot at r_o, their results show that there is an infinite number of states available in the dot, with energy less than $\hbar\omega_c/2$, consequently all the electrons are attracted to the centre of the magnetic quantum dot. For a system with a magnetic field overshoot at r_o, they found that most of the electrons are repelled and forced outside the magnetic quantum dot. Only when the radius of the magnetic quantum dot is sufficiently large, do magnetic quantum dot states become available with energies less than $\hbar\omega_c/2$. From this Peeters *et al* [9] and Reijniers *et al* [10] obtained the electron filling of a magnetic quantum dot, and determined that the number of electrons in the dot increases in discrete steps at particular magnetic quantum dot radii.

Interaction effects in nanostructure boxes were first studied theoretically by Bryant [31]. He investigated electron correlation effects of few-electron systems confined in quasi-zero-dimensional, ultrasmall, quantum well boxes. He found

that the single electron matrix elements scale as $1/L^2$, where L is the linear dimension of the quantum well box, while the Coulomb matrix elements scale as $1/L$. Results show that for small L, the Coulomb interactions are insignificant compared to the single electron level spacing, and the electrons behave as independent, uncorrelated particles. When L is large, the author found that correlation effects become important, and the electrons form a Wigner lattice [32]. More recently, Maksym and Chakraborty [14] studied interacting electrons confined in quantum dots in a magnetic field. Their idealised model consists of a confining potential that is parabolic in form and a 2DEG that is of infinitesimally small thickness. Their results show, for systems containing three and four electrons, that the ground state only occurs at certain "magic" values of the total angular momentum quantum number. As the magnetic field is increased, the ground state angular momentum quantum number increases to a higher "magic" angular momentum quantum number. They suggested that the reason for this is because the magnetic field compresses the wave function of the system and therefore increases the Coulomb energy. At certain critical magnetic fields the system can reduce its energy by making a transition to a new ground state, which has a larger spatial extent and a higher angular momentum quantum number. Pfannkuche *et al* [33] investigated the electronic properties of an idealised quantum dot system containing two interacting electrons. They compared an interacting system with a non-interacting system. For the non-interacting system, it has been known for many years [22, 23] that the energy levels tend to arrange in groups, forming different Landau levels [2]. Pfannkuche *et al* [33] showed that with the interaction, much of the clear structure immanent in the non-interacting spectra is destroyed, and energy level crossings within

each Landau level are observed. The effect of the electron-electron interaction, on the total ground state spin quantum number has been studied by Maksym and Chakraborty [13] and independently by Wagner *et al* [34]. Maksym and Chakraborty [13] investigated the magnetisation of interacting electrons in a parabolic quantum dot. Their results show for systems containing three and four electrons, that the magnetisation as a function of the magnetic field contains a number of discontinuities. These authors showed that the discontinuities are a consequence of changes in the ground state spin and angular momentum quantum numbers as the magnetic field increases. Wagner *et al* [34] investigated the ground state energy of a two electron idealised quantum dot, as a function of magnetic field. Their results show that as the magnetic field is increased, the spin configuration of the electrons oscillates between spin singlet and spin triplet ground states. In further studies, more realistic models of quantum dots have been used. Bruce and Maksym [35] have included three dimensional motion of interacting electrons in their calculations, electron screening effects due to the gate electrodes, and made no assumptions about the form of the confining potential. They compared their results to an idealised two dimensional system and found that the total angular momentum transition of the ground state in the realistic model generally occurs at higher magnetic fields as compared to the idealised two dimensional system.

4.2 The Coulomb Matrix Elements

In this section, the calculation of the Coulomb matrix elements given by Eq. 2.12 is discussed. The explicit details of the calculation are given in appendix A. Here, the numerical and computational issues associated with evaluating the matrix elements are discussed, and new methods to compute the Coulomb matrix elements are given. Three different ways of evaluating the Coulomb matrix elements are investigated.

The evaluation of the Coulomb matrix elements is potentially one of the most CPU intensive aspects of a numerical diagonalisation calculation. For a calculation that includes a large number of Landau levels, it is found that a large number of matrix elements must be evaluated. For example, a two electron calculation with total angular momentum quantum number $J = 0$, including seventeen Landau levels requires 803247 distinct Coulomb matrix elements to be evaluated (see figure 4.1), and this number increases further as J increases. With so many matrix elements to evaluate, it is important to develop highly efficient algorithms to calculate them.

The underlying method by which the Coulomb matrix elements are calculated, is the same for each of the three ways. This method follows from the work of Maksym [14], and involves taking the Fourier transform of $1/|\mathbf{r}|$. The interaction potential, $v(\mathbf{r}_1, \mathbf{r}_2)$, can then be written as

$$\begin{aligned} v(\mathbf{r}_1, \mathbf{r}_2) &= \frac{e^2}{4\pi\epsilon\epsilon_o} \frac{1}{|\mathbf{r}_1 - \mathbf{r}_2|} \\ &= \frac{e^2}{4\pi\epsilon\epsilon_o} \frac{1}{2\pi} \int \frac{e^{i\mathbf{q}\cdot(\mathbf{r}_1 - \mathbf{r}_2)}}{|\mathbf{q}|} d\mathbf{q}. \end{aligned} \tag{4.1}$$

To calculate an explicit form for the Coulomb matrix elements, this expression along with Eq. 2.13 are substituted into Eq. 2.12. The details of the calculation

are given in appendix A, the result being

$$\begin{aligned}\langle ij|v|kl\rangle &= \frac{(2e\pi l_B^2)^2}{4\pi\epsilon\epsilon_o} N_{n_i l_i} N_{n_j l_j} N_{n_k l_k} N_{n_l l_l} \sum_{\alpha=0}^{n_i}\sum_{\beta=0}^{n_l}\sum_{\gamma=0}^{n_j}\sum_{\delta=0}^{n_k} \frac{(-1)^{\alpha+\beta+\gamma+\delta}}{\alpha!\beta!\gamma!\delta!} \\ &\times \binom{n_i+|l_i|}{n_i-\alpha}\binom{n_l+|l_l|}{n_l-\beta}\binom{n_j+|l_j|}{n_j-\gamma}\binom{n_k+|l_k|}{n_k-\delta} A!B! \\ &\times \int_0^\infty e^{-q^2 l_B^2}\left(\frac{q^2 l_B^2}{2}\right)^{|\lambda|} L_A^{|\lambda|}\left(\frac{q^2 l_B^2}{2}\right) L_B^{|\lambda|}\left(\frac{q^2 l_B^2}{2}\right) dq, \end{aligned} \tag{4.2}$$

where

$$A = \left(\alpha+\beta+\frac{1}{2}\left[|l_i|+|l_l|-|\lambda|\right]\right), \tag{4.3}$$

$$B = \left(\gamma+\delta+\frac{1}{2}\left[|l_j|+|l_k|-|\lambda|\right]\right) \tag{4.4}$$

and $\lambda = l_l - l_i = l_j - l_k$. To evaluate the Coulomb matrix elements, the integral over q in Eq. 4.2 can be evaluated in two ways. An analytic form for the integral can be obtained by performing a series expansion of the associated Laguerre polynomials, the resulting expression can then be integrated term by term. This method has been shown to work well [24, 36], for total angular momentum quantum numbers of roughly $J < 60$, when only one Landau level is included in the calculation, and roughly $J < 40$ when four are included. For higher values of the quantum numbers the method is prone to numerical error. The reason for this is the roundoff errors that are accumulated due to the cancellation of successive terms with alternating sign. To overcome this, the integral is evaluated numerically. It is seen that the integral is a product of a Gaussian function and a polynomial, and hence can be evaluated exactly using a standard Gauss-Hermite routine with the integrand evaluated at 64 points. Using this method to evaluate the integral is advantageous in a number of ways. First, it is approximately ten times faster than the analytic method, taking roughly 1 ms on a HP 735 workstation to evaluate one Coulomb matrix element. This method is also more

numerically stable than the analytic method. If one Landau level is included in the calculation, then it is numerically stable for up to roughly $J = 100$. Because the ground state of the system usually has a much lower value of J, this is not a problem. Further, for $J = 0$, calculations including up to the eighth Landau level are possible, before any numerical problems are encountered.

To obtain converged energy eigenvalues for systems with large radii, calculations involving more Landau levels are needed. This is because the Fock-Darwin states are only exact when $r_o = 0$ nm, hence to obtain converged energy eigenvalues, more Landau levels must be included in a numerical diagonalisation calculation. It is therefore necessary to derive a new method to evaluate the Coulomb matrix elements, which is numerically stable for calculations including larger values of the quantum numbers. The method that is used is due to Maksym [24], and again involves substituting Eq. 2.13 and Eq. 4.1 into Eq. 2.12. The details are given in appendix A, the result being

$$\begin{aligned}\langle ij|v|kl\rangle &= \frac{(2e\pi l_B^2)^2}{4\pi\epsilon\epsilon_o} N_{n_i l_i} N_{n_j l_j} N_{n_k l_k} N_{n_l l_l} \int_0^\infty dq\, q^{2\lambda} e^{-2q^2} \\ &\times \int_0^\infty dx_1 e^{-x_1} x_1^{s+\lambda} L_{n_i}^{|l_i|}(x_1) L_{n_l}^{|l_l|}(x_1) \sum_{m=0}^{s+n_i+n_l} \frac{q^{2m} L_m^\lambda(x_1)}{(m+\lambda)!} \\ &\times \int_0^\infty dx_2 e^{-x_2} x_2^{t+\lambda} L_{n_j}^{|l_j|}(x_2) L_{n_k}^{|l_k|}(x_2) \sum_{p=0}^{t+n_j+n_k} \frac{q^{2p} L_p^\lambda(x_2)}{(p+\lambda)!}, \end{aligned} \tag{4.5}$$

where $s = (|l_i|+|l_l|-\lambda)/2$ and $t = (|l_j|+|l_k|-\lambda)/2$. The integrals over q, x_1 and x_2 are evaluated numerically. To evaluate the q integral, the integrand is calculated at 100 points and a Gauss-Hermite routine is used. The x_1 and x_2 integrals are evaluated using a Gauss-Laguerre routine, each with 150 points. Using this method to evaluate the Coulomb matrix elements, up to fifteen Landau levels can be included in a numerical diagonalisation calculation for $J = 0$, before any numerical problems arise. If one Landau level is included in the calculation then

the routine is numerically stable for up to roughly $J = 80$. While this method allows calculations involving a larger number of Landau levels, the computational time to evaluate a Coulomb matrix element is higher, taking roughly 50 ms to evaluate one Coulomb matrix element.

For calculations involving more than fifteen Landau levels, a third method to evaluate the Coulomb matrix elements is used. Again the method involves taking the Fourier transform of the interaction potential, and substituting this along with Eq. 2.13 into Eq. 2.12. The expression that the routine evaluates is given here, and the details of the method are given in appendix A. The routine evaluates the expression

$$\begin{aligned}\langle ij|v|kl\rangle &= \frac{(4e\pi l_B^2)^2}{4\pi\epsilon\epsilon_o} N_{n_i l_i} N_{n_j l_j} N_{n_k l_k} N_{n_l l_l} \int_0^\infty dq \\ &\times \int_0^\infty x_1^{|l_i|+|l_l|+1} e^{-x_1^2} L_{n_i}^{|l_i|}(x_1^2) L_{n_l}^{|l_l|}(x_1^2) J_\lambda(\sqrt{2}qx_1) dx_1 \\ &\times \int_0^\infty x_2^{|l_j|+|l_k|+1} e^{-x_2^2} L_{n_j}^{|l_j|}(x_2^2) L_{n_k}^{|l_k|}(x_2^2) J_\lambda(\sqrt{2}qx_2) dx_2. \qquad (4.6)\end{aligned}$$

To evaluate the integrals over x_1 and x_2, an adaptive integration routine from the NAG library is used. This routine is especially suited to oscillating, non-singular integrands, and calculates an approximation to the integral over a finite interval. Because the exponential functions cause the integrands to decay rapidly, the upper limit of the integral is set to 20. This ensures precision to roughly twelve decimal places. In appendix A it is shown that the analytic form of the integrals over x_1 and x_2 is a Gaussian function multiplied by a polynomial. This allows the integral over q, to be evaluated exactly using a standard Gauss-Hermite routine, with the integrand evaluated at 220 points. The disadvantage of using this method to evaluate the Coulomb matrix elements is that it is extremely slow. To evaluate one Coulomb matrix element, typically takes up to four seconds. However, the method is extremely stable, and no numerical

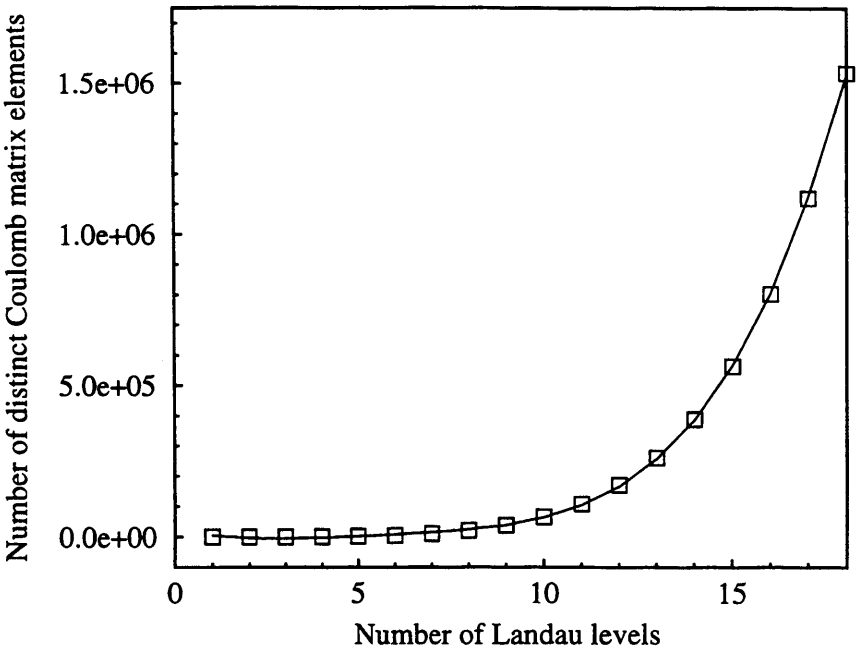

Figure 4.1: The number of Landau levels included in a two electron numerical diagonalisation calculation, as a function of the number of distinct Coulomb matrix elements that must be evaluated, for $J = 0$. The squares indicate results obtained from the numerical diagonalisation calculation and the solid curve is the result of a fit of this data to the expression $ax^4 + bx^3 + cx^2 + dx + e$.

problems are encountered with a calculation for $J = 0$, including up to twenty Landau levels.

The issue of the computational effort required to evaluate the Coulomb matrix elements is now addressed. Figure 4.1 shows the number of Landau levels included in a two electron numerical diagonalisation calculation, as a function of the number of distinct Coulomb matrix elements that must be evaluated, for a total angular momentum quantum number $J = 0$. The squares indicate results obtained from a numerical diagonalisation calculation, and the solid curve is the result of a fit of this data to an expression of the form $ax^4 + bx^3 + cx^2 + dx + e$,

where a, b, c, d and e are constants. The fit is obtained using the plotting package, Xmgr. Obviously fitting the data to expressions of higher degree improves the fit further, however as is seen in the plot, the fit to a quartic expression is excellent throughout the range of Landau level values. From the figure it is seen that for less than approximately six Landau levels, the number of distinct matrix elements that must be evaluated is of the order of a few thousand. This corresponds to roughly five hours of computational time, using the final method described to evaluate the matrix elements. As the number of Landau levels is increased further, the number of distinct matrix elements that must be calculated increases rapidly, with eighteen Landau levels included in a numerical diagonalisation calculation, roughly one and a half million matrix elements need to be calculated. If Eq. 4.6 is used to evaluate the matrix elements, then over sixty days of computational time are needed. Obviously, given finite computing resources, this is far from ideal. To make the calculation tractable for numerical diagonalisation calculations involving such a large number of Landau levels, the fastest routine that is stable is used to evaluate the matrix elements. For calculations including up to the eighth Landau level, Eq. 4.2 is used to evaluate the matrix elements. The matrix elements are evaluated using Eq. 4.5, for calculations including between the eighth and the fifteenth Landau level, otherwise Eq. 4.6 is used.

Several other methods to evaluate the Coulomb matrix elements have been devised. Instead of taking the Fourier transform of $1/|\mathbf{r}|$, Girvin and Jach [37] calculated the Coulomb matrix elements by changing to centre of mass and relative coordinates, and evaluated the matrix elements between the lowest Landau level states. Ultimately an expression involving a triple sum of terms with alternating sign is obtained, and therefore this method is also prone to the

same numerical difficulties discussed previously due to roundoff errors. Another method that avoids such numerical instabilities is due to Stone *et al* [38]. They also calculated the Coulomb matrix elements between the lowest Landau level states, and used a Gaussian integral to represent $1/|\mathbf{r}|$. The resulting formula for the Coulomb matrix elements contains an infinite series of positive terms. Consequently, the roundoff errors that are discussed previously are avoided. The convergence is, however, very slow. The generalisation of this method to include higher Landau levels is not easy [24], and therefore the method is thought to be unsuitable for calculating the electronic properties of magnetic quantum dots.

4.3 Confining Interacting Electrons in a Magnetic Quantum Dot

In this section the possibility of confining interacting electrons in a magnetic quantum dot is discussed. The form of the confining magnetic field in a magnetic quantum dot is compared to the confining potential of the more familiar electrostatic quantum dot, and contrasts are made. It is argued, for a magnetic quantum dot containing two interacting electrons, that confinement is possible, but only if certain energy conditions are satisfied. This argument can also be extended to discuss systems containing more electrons.

In figure 4.2, the confining magnetic field in a magnetic quantum dot (shown by the solid line in the figure) is compared to a typical confining potential in an electrostatic quantum dot (shown by the dashed curve in the figure). The confining potential in an electrostatic quantum dot can be provided by a negatively biased modulated gate fabricated on top of a heterostructure in which a 2DEG is defined [39]. From the figure it is seen that the confining potential in an electrostatic dot, which is usually assumed to be parabolic in

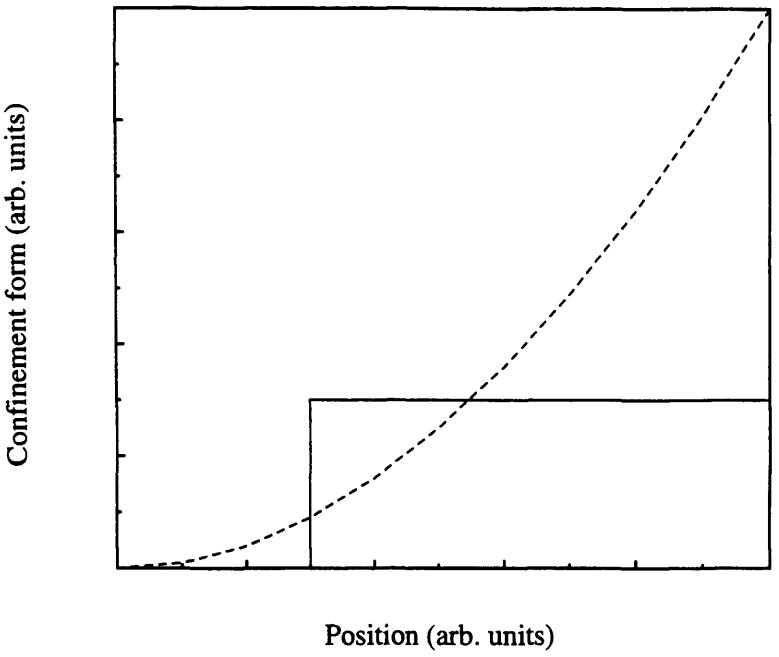

Figure 4.2: Comparison of the confining potential in an electrostatic quantum dot (dashed curve) and the confining magnetic field in a magnetic quantum dot (solid curve).

form, tends to infinity for large distances. Because of this, interacting electrons in an electrostatic quantum dot will always be confined. The form of the confining magnetic field in a magnetic quantum dot, is defined by the spatial variation of the magnetic field in the system, and in turn this is defined by the geometry of the ferromagnetic layer or superconducting disk deposited near the 2DEG. The figure shows a typical confining magnetic field profile in a magnetic quantum dot, and it is seen that the confining magnetic field is constant for large distances. Therefore if the repulsive Coulomb force is large enough, electrons will be forced outside the dot.

In chapter 3 it is shown that the ground state configuration of a magnetic quantum dot containing one electron has an angular momentum quantum number $l = 0$, for all values of the magnetic field and magnetic quantum dot radius.

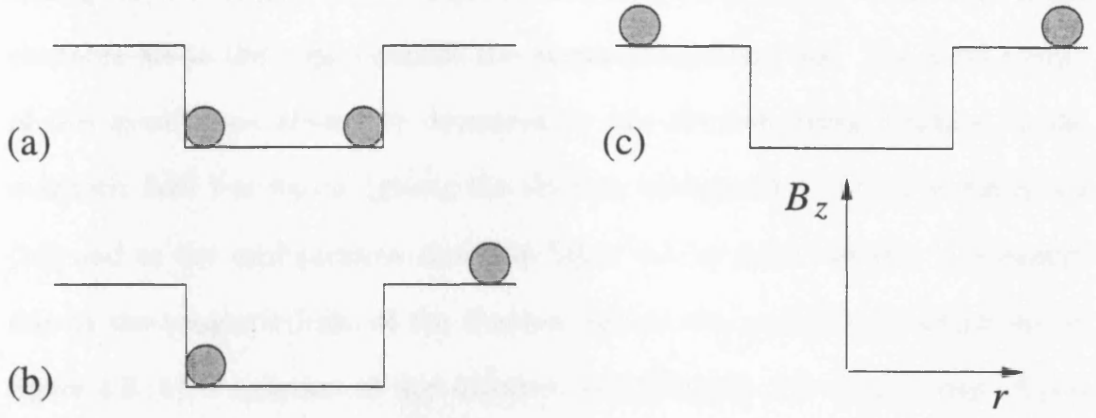

Figure 4.3: A schematic diagram of the available electron configurations, for a magnetic quantum dot containing two interacting electrons. The shaded circles indicate the electrons.

Therefore, the electron is localised at the centre of the magnetic quantum dot (see figure 3.2 for example), and hence is always confined. However, this is not the case if a second electron is added to the system. Due to the repulsive Coulomb force between the two electrons, confinement of both electrons is only possible under certain conditions. For two interacting electrons to be confined in a magnetic quantum dot, the energy of the electrons localised inside the magnetic quantum dot must be less than the energy of any other electron configuration. This can be investigated qualitatively by treating the electrons as particles. Under this premise an electron is either inside or outside the magnetic quantum dot, and figure 4.3 shows a schematic diagram of the possible electron configurations in a two electron system.

In the figure, the wells represent the magnetic field profile in the system, with the magnetic field at the bottom of the well equal to zero, and the electrons are indicated by the shaded circles. Figure 4.3 (a) shows a system in which two interacting electrons are confined in the magnetic quantum dot. In figure 4.3 (b),

one of the electrons is confined in the magnetic quantum dot, and the other is in the region with magnetic field. Figure 4.3 (c) shows a system in which both of the electrons are in the region outside the magnetic quantum dot. The total energy of this system can always be decreased by one electron being localised in the magnetic field free region (giving the electron configuration shown in figure 4.3 (b)) and so the configuration shown in figure 4.3 (c) never occurs. The energy due to the magnetic field, of the electron outside the magnetic quantum dot in figure 4.3 (b) is constant at any distance, and therefore the total energy of this system is decreased by increasing the electron separation, hence the Coulomb energy effectively tends to zero. Therefore if one electron is in the magnetic quantum dot, and the energy to add the second electron is less than the energy due to the magnetic field ($\hbar\omega_c/2 + g^*\mu_B B_z S_z$), the two electrons can be confined and the system is said to be stable.

4.4 Two Interacting Electrons in a Magnetic Quantum Dot

The main aim of this section, is to investigate how the stability of a magnetic quantum dot containing two interacting electrons depends on the confining magnetic field and the magnetic quantum dot radius. First, the question of how to determine if a system is stable is answered and the physics of stability is discussed. Results are presented for a GaAs system with and without a magnetic field overshoot at r_o. For comparison results are also calculated for an InSb system. This enables the effect of the material parameters (effective mass, relative permittivity and effective g factor) on the stability of the system to be investigated. In the next section the results for the GaAs system without a magnetic field overshoot at r_o are compared with those obtained when the system

is in an additional external magnetic field and contrasts between the two sets of results are made. The results are also compared to those calculated for a more realistic system, with an electron layer of finite thickness.

4.4.1 Determining the Stability of the System

To determine whether a system is stable, an investigation of the two electron energy as a function of angular momentum quantum number is undertaken. Energies as a function of angular momentum quantum number, for a spin unpolarised, $S = 0$, where S is the sum of the single electron spin quantum numbers, and a spin polarised, $S = 1$, GaAs system without a magnetic field overshoot at r_o are shown in figure 4.4. The results shown by the diamonds in the figure are for a spin unpolarised system, and the results shown by the squares in the figure are for a spin polarised system. The magnetic field is $B_z = 5$ T, the magnetic quantum dot radius is $r_o = 40$ nm, and the results are calculated using the numerical diagonalisation method with seven Landau levels included in the calculation. This ensures the results are accurate to roughly 0.01% for $J = 0$ and 0.001% for $J = 12$. From the figure it is seen that ground state energy, calculated for the given parameters, coincides with $J = 0$ for a spin unpolarised system and $J = 1$ for a spin polarised system. As J increases, the two electron energy increases to a maximum, and as J increases further, the energy decreases steadily. The energy for the spin polarised system is lower for large J because of the Zeeman energy. The energy begins to decrease steadily for large J, because one of the electrons is in the magnetic field region. By increasing the angular momentum quantum number, J, the separation of the electrons is increased [27], hence decreasing the Coulomb energy, and the total energy of the system.

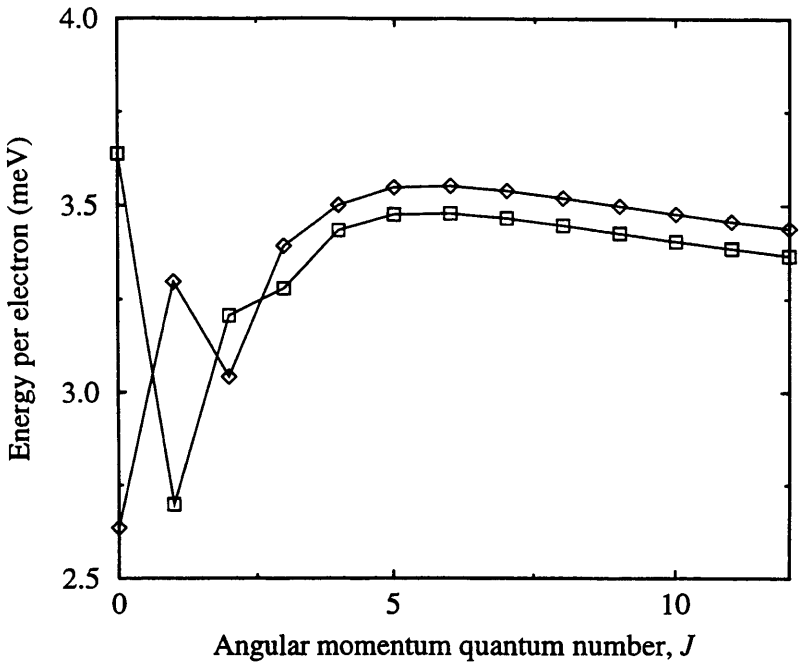

Figure 4.4: Two electron energy as a function of angular momentum quantum number, for a spin unpolarised, GaAs system without a magnetic field overshoot at r_o (diamonds), and a spin polarised, GaAs system without a magnetic field overshoot at r_o (squares). The magnetic field is $B_z = 5$ T and the magnetic quantum dot radius is $r_o = 40$ nm. The solid lines are to guide the eye.

To determine whether this system is stable, the ground state energy of the two electrons localised in the centre of the magnetic quantum dot (energy at $J = 0$ for $S = 0$ or $J = 1$ for $S = 1$), is compared with the total energy of one electron localised in the centre of the magnetic quantum dot and one electron localised at an infinite distance from the centre in the region with a magnetic field (energy at $J = \infty$). The ground state energy for finite J is found from the calculated data, and for the spin unpolarised system the ground state energy coincides with $J = 0$, and is found to be 2.6347 meV. For the spin polarised system the ground state energy coincides with $J = 1$, and is 2.6972 meV. Therefore the ground state

energy at finite J is 2.6347 meV. To determine the energy at $J = \infty$, the energy of the electron localised in the centre of the magnetic quantum dot is calculated using the numerical diagonalisation method, and is found to be 0.9597 meV. The energy of the second electron is the energy due to the magnetic field and is given by $\hbar\omega_c/2 + g^*\mu_B B_z S_z$, where $g^* = -0.44$ is the effective g factor for GaAs and $S_z = 1/2$, hence the energy at $J = \infty$ is found to be 2.6079 meV per electron. Comparing this with the energy per electron at $J = 0$, which is 2.6347 meV, it is found that the energy at $J = \infty$ is the true ground state of the system, and the magnetic quantum dot is unable to confine both electrons, hence this system is unstable.

Repeating this procedure for systems with different confining magnetic fields and magnetic quantum dot radii, it is possible to determine how the stability of a magnetic quantum dot depends on these parameters. Figure 4.5 shows the stability as a function of the system parameters, for a GaAs magnetic quantum dot without a magnetic field overshoot at r_o. The solid curve in the figure is the result of a least squares fit to the data, and this is discussed more thoroughly in section 4.4.2. The region to the right and above the solid curve indicates a system that is stable, while the region to the left and below the solid curve indicates a system that is unstable. The uncertainty in the data, shown by the error bars in the figure, is due to the finite sampling of the confining magnetic field points. The energies are calculated at steps of 0.5 T for the confining magnetic field, and steps of 5 nm for the magnetic quantum dot radius. To obtain the data shown in the figure, seventeen Landau levels are included in the numerical diagonalisation calculation. This enables all the energies for the given parameters to be calculated with an accuracy of better than 4%. As a rough guide to the computational time

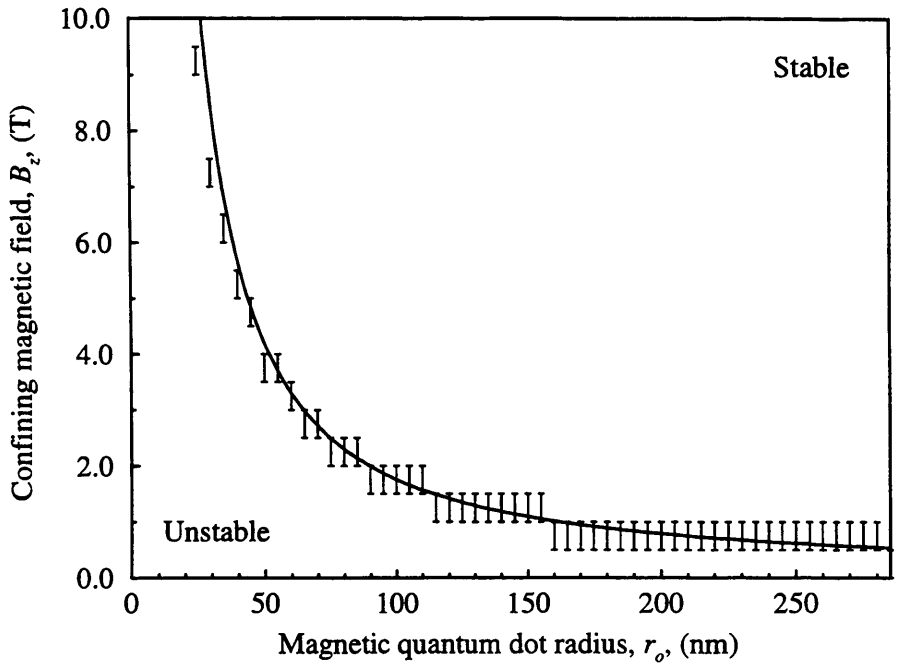

Figure 4.5: Stability as a function of the system parameters for a GaAs magnetic quantum dot without a magnetic field overshoot at r_o. The solid curve is the result of a least squares fit to the data.

required to calculate one stability point, a numerical diagonalisation calculation including seventeen Landau levels requires approximately 50 hours of CPU time on a HP 735 workstation. Roughly all of this time is used to evaluate the Coulomb matrix elements, hence they are stored in a look up table. This enables the remaining stability points to be determined in an additional time of roughly 30 hours.

The figure shows the existence of a stability boundary in the system parameter space. It is seen that the system is stable for relatively small magnetic quantum dot radii, if the magnetic quantum dot has a large confining magnetic field ($B_z \sim 10$ T). This is because the energy due to the magnetic field, outside the magnetic quantum dot is greater than the energy due to the Coulomb repulsion

between the electrons. For systems with a larger magnetic quantum dot radii, the magnetic quantum dot is able to confine the electrons with a smaller confining magnetic field because the electrons are able increase their separation, so that the energy due to the Coulomb repulsion is less than the energy due to the magnetic field outside the magnetic quantum dot. The stability of this system is discussed in greater detail later in this chapter. Also further results showing the stability of other magnetic quantum dot systems are presented. First a theoretical investigation of the two electron system is undertaken and the physics of stability is discussed. Through this discussion, an analytic form for the stability boundary is obtained.

4.4.2 Physics of Stability

To investigate the physics of stability, and to predict the form of the stability boundary as a function of the system parameters (the confining magnetic field and the magnetic quantum dot radius) the energy of the two electron system at finite J and the energy of the two electron system at infinite J are found by dimensional analysis. By equating these energies, an analytic form for the stability boundary is determined.

To obtain an equation for the energy, E, at finite J, the hamiltonian for the system is written as

$$\begin{aligned} H &= \sum_{i=1}^{2} -\frac{\hbar^2\nabla_i^2}{2m^*} + f^2(r_i)\frac{m^*\omega_c^2 r_i^2}{8} + f(r_i)\frac{\hbar\omega_c l}{2} \\ &+ g^*\mu_B B(r_i)S_{zi} + \frac{e^2}{4\pi\epsilon\epsilon_o}\frac{1}{|\mathbf{r}_1 - \mathbf{r}_2|}, \end{aligned} \tag{4.7}$$

where $f(r)$ has the form $(1 - r_o^2/r^2)\theta(r - r_o)$ or $\theta(r - r_o)$ depending on whether the vector potential is given by Eq. 2.7 or Eq. 2.8. Introducing the dimensionless

variable $r' = r/r_o$ and $\hbar^2/2m^*r_o^2$ as the energy unit, the following eigenvalue equation can be obtained

$$\sum_{i=1}^{2}\left[-\nabla_i' + \frac{\beta^2}{4}r_i'^2 f^2(r_i') - \beta l f(r_i')\right]\psi(\alpha,\beta,\gamma,r') + \gamma b(r_i')S_{zi}\psi(\alpha,\beta,\gamma,r') + \frac{\alpha}{|\mathbf{r}'_1 - \mathbf{r}'_2|}\psi(\alpha,\beta,\gamma,r') = \lambda\psi(\alpha,\beta,\gamma,r'), \tag{4.8}$$

where $\alpha = m^*r_o e^2/2\hbar^2\pi\epsilon\epsilon_o$, $\beta = m^*r_o^2\omega_c/\hbar$, $\gamma = 2m^*r_o^2 g^*\mu_B B_z/\hbar^2$, $\lambda = 2m^*r_o^2 E/\hbar^2$ and the substitution $B(r') = B_z b(r')$, where $b(r') = \theta(r'-1)$, has been made. If the form of the wave function, $\psi(\alpha,\beta,\gamma,r')$, is known, λ can be found by taking matrix elements of the dimensionless hamiltonian, hence it is found that

$$\lambda = h_n(\alpha,\beta,\gamma) + \gamma S_z v_n(\alpha,\beta,\gamma) + \alpha g_n(\alpha,\beta,\gamma), \tag{4.9}$$

where $h_n(\alpha,\beta,\gamma)$ is the matrix element of the term in square brackets in Eq. 4.8, $v_n(\alpha,\beta,\gamma)$ is the matrix element of $b(r')$, $g_n(\alpha,\beta,\gamma)$ is the matrix element of $1/|\mathbf{r}'_1 - \mathbf{r}'_2|$ and n is an eigenvalue quantum number. Converting Eq. 4.8 back to standard S.I. units, the final form of the energy, E, at finite J is found to be

$$E = \frac{\hbar^2}{2m^*r_o^2}h_n(\alpha,\beta,\gamma) + g^*\mu_B B_z S_z v_n(\alpha,\beta,\gamma) + \frac{e^2}{4\pi\epsilon\epsilon_o r_o}g_n(\alpha,\beta,\gamma). \tag{4.10}$$

The energy, E_∞, of the system for infinite J, is obtained by a similar argument. The total energy of the system is the energy of one electron localised at the centre of the magnetic quantum dot and the energy of one electron localised an infinite distance from the centre. The energy of one electron localised at the centre of the dot is

$$\frac{\hbar^2}{2m^*r_o^2}h_n'(\beta,\gamma) + g^*\mu_B B_z S_z v_n'(\beta,\gamma), \tag{4.11}$$

where $h_n'(\beta,\gamma)$ and $v_n'(\beta,\gamma)$ are matrix elements that are different from $h_n(\alpha,\beta,\gamma)$ and $v_n(\alpha,\beta,\gamma)$ in Eq. 4.10. The energy of the electron localised an infinite

distance from the centre of the magnetic quantum dot, is the energy due to the magnetic field and is given by $\hbar\omega_c/2$ if the Zeeman term is neglected. Therefore the energy, E_∞, of the system for infinite J is

$$E_\infty = \frac{\hbar^2}{2m^* r_o^2} h'_n(\beta,\gamma) + g^*\mu_B B_z S_z v'_n(\beta,\gamma) + \frac{\hbar\omega_c}{2}. \tag{4.12}$$

For a system to be stable the condition $E < E_\infty$ must be satisfied, hence the stability condition is found by equating Eq. 4.10 and Eq. 4.12, giving

$$\frac{\hbar e B_z}{2m^*} = \frac{\hbar^2}{2m^* r_o^2}(h_0 - h'_0) + g^*\mu_B B_z S_z (v_0 - v'_0) + \frac{e^2}{4\pi\epsilon\epsilon_o r_o} g_0. \tag{4.13}$$

The explicit forms of the matrix elements in this equation are unknown, nevertheless a curve can be fitted to the stability data shown in figure 4.5 by assuming that the matrix elements (h_0, h'_0, v_0, v'_0 and g_0) are constant. By making this assumption, the stability condition becomes $B_z \approx a/r_o^2 + b/r_o$, where a and b are constants, and the solid curve in figure 4.5 is the result of a least squares fit to this form. To obtain the best fit to the numerical data shown in figure 4.5, points on the best curve through the errors bars are input into a standard least squares fitting routine. The values of the constants are then found to be $a = 141 \pm 14$ and $b = 3413 \pm 340$.

From figure 4.5 it is seen that the fit (shown by the solid curve in the figure) is excellent for large magnetic quantum dot radii and small confining magnetic field, but for small magnetic quantum dot radii and large confining magnetic field the fit deviates from the data. The reason for this deviation is that as the confining magnetic field becomes large, the single electron energy of an electron inside the magnetic quantum dot tends to the energy due to the magnetic field, given by $\hbar e B_z/2m^*$, which is independent of r_o. Thus the assumption that h_0 and h'_0 are constant breaks down.

4.4.3 Stability Results for a GaAs System

Figure 4.6 shows the stability boundaries for a GaAs magnetic quantum dot with and without a magnetic field overshoot at r_o, as a function of the system parameters. The dark shaded region indicates a system that is stable, while the unshaded region indicates a system that is unstable. The light shaded region indicates a system that is unstable only in the presence of the magnetic field overshoot at r_o. The stable systems are all spin unpolarised. The solid curves in the figure are the results of a least squares fit to the numerical data. From the figure it is seen that the system with a magnetic field overshoot at r_o is less stable than the corresponding system without a magnetic field overshoot. The reason for this can be determined by comparing the total energy of a stable system, with the total energy of the corresponding unstable system. For the stable system without a magnetic field overshoot, with $B_z = 9.5$ T and $r_o = 30$ nm, the single electron energy is 4.60 meV and the Coulomb energy is 3.74 meV, giving a total energy of 8.34 meV. These system parameters are chosen because the convergence of the energy eigenvalues is good for a calculation including relatively few Landau levels. Seven Landau levels are used to obtain energies accurate to roughly 1%. The single electron energy of the corresponding unstable system with a magnetic field overshoot is found to be 6.93 meV, and the Coulomb energy is 5.13 meV, hence the total energy of the unstable system is 12.06 meV. Therefore the total energy of the two electrons inside the magnetic quantum dot increases in the presence of the magnetic field overshoot, hence the decrease in stability is caused by an increase in the total energy of the system.

To investigate the stable and unstable states of this system further, the electron density, the pair distribution and the pair correlation functions of the stable

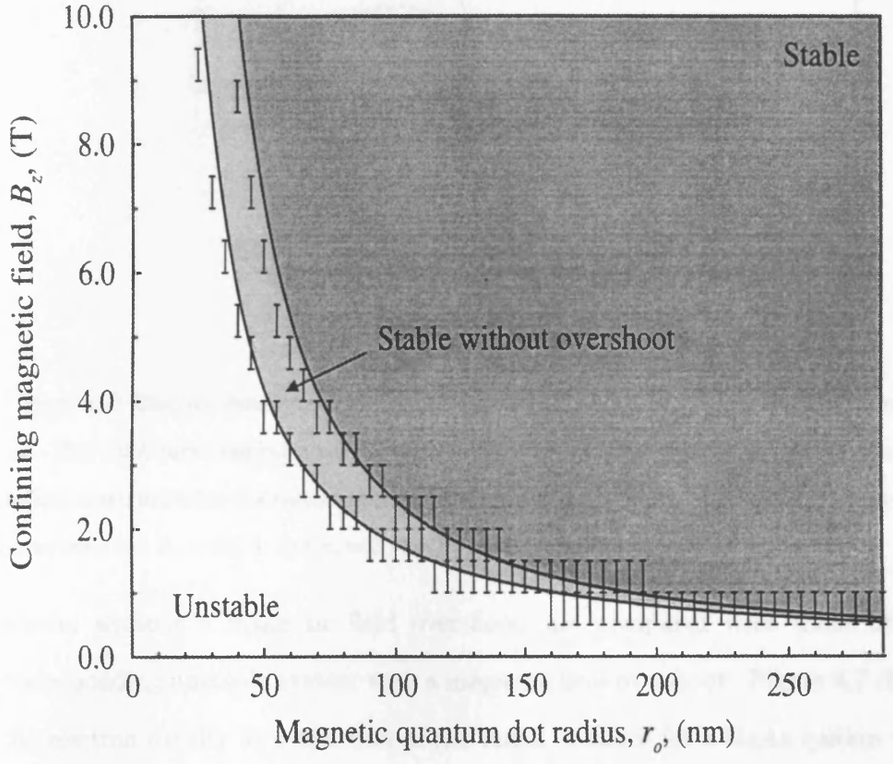

Figure 4.6: Stability as a function of the system parameters for a GaAs magnetic quantum dot with and without a magnetic field overshoot at r_o. The solid curves are the result of a least squares fit to the numerical data.

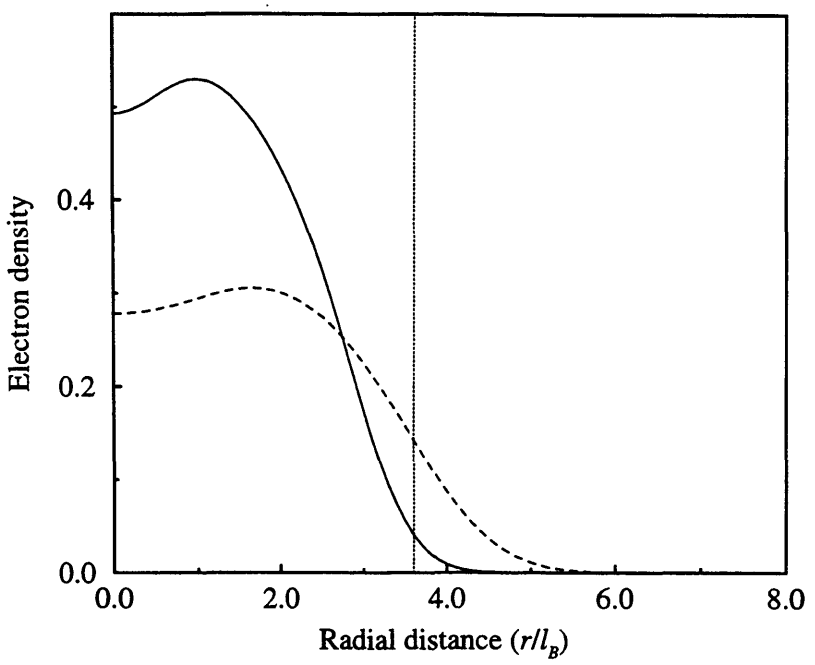

Figure 4.7: Electron density as a function of the radial distance for a GaAs magnetic quantum dot. The solid curve indicates the results obtained for a system with an overshoot, and the dashed curve indicates the results obtained a system without an overshoot at r_o. The system parameters are $B_z = 9.5$ T and $r_o = 30$ nm.

system without a magnetic field overshoot, are compared with those of the corresponding unstable system with a magnetic field overshoot. Figure 4.7 shows the electron density as a function of the radial distance for a GaAs system with and without a magnetic field overshoot at r_o, for $B_z = 9.5$ T and $r_o = 30$ nm. The density is normalised such that $2\pi \int_0^\infty n(x)xdx = N$, where $x = r/l_B$. The solid curve indicates the results obtained for a system with a magnetic field overshoot and the dashed curve indicates the results obtained for a system without a magnetic field overshoot. The figure shows that the effect of the overshoot in the magnetic field, is to localise the electrons more strongly inside the magnetic quantum dot (the vertical dotted line indicates the position of r_o). In chapter

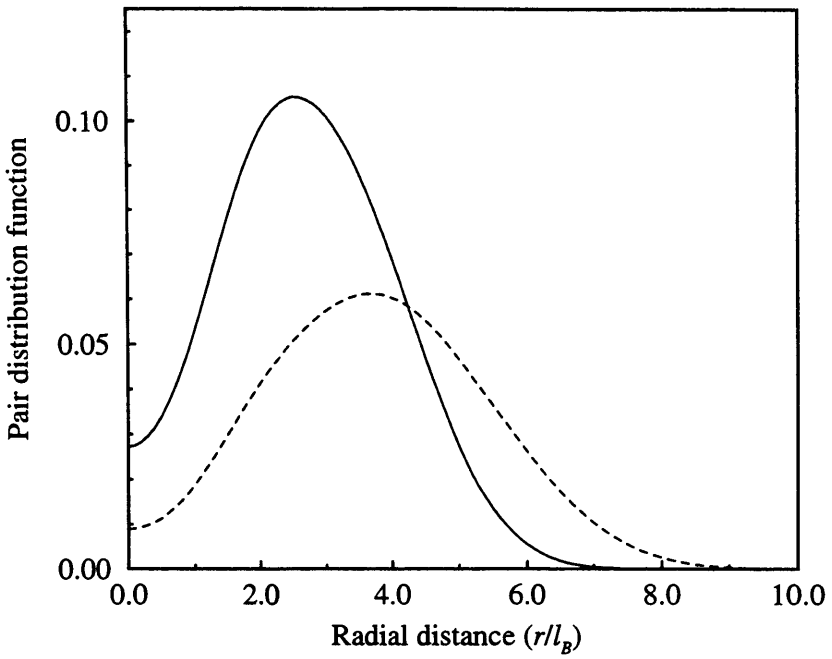

Figure 4.8: Pair distribution function as a function of the radial distance for a GaAs magnetic quantum dot. The solid curve indicates the results obtained for a system with an overshoot in the magnetic field at r_o, and the dashed curve indicates the results obtained for a system without a magnetic field overshoot at r_o. The confining magnetic field is $B_z = 9.5$ T and the magnetic quantum dot radius is $r_o = 30$ nm.

3, the overshoot in the magnetic field is shown to increase the single electron energy of the system. Because the electrons are localised more strongly inside the magnetic quantum dot, the Coulomb energy of the system is also increased. This is consistent with the increase in the calculated Coulomb energy for the stable and unstable systems.

Figure 4.8 shows the pair distribution function as a function of the radial distance for a GaAs system, with and without a magnetic field overshoot at r_o, again for $B_z = 9.5$ T and $r_o = 30$ nm. The definition of the pair distribution

function, $g(\mathbf{r})$, follows the convention used by Maksym [40], and is given by

$$g(\mathbf{r}) = \frac{2\pi l_B^2}{N(N-1)} \left\langle \sum_{i \neq j} \delta\left(\mathbf{r}_i - \mathbf{r}_j + \mathbf{r}\right) \right\rangle, \tag{4.14}$$

where the angular brackets denote the expectation value. Expressing Eq. 4.14 in terms of the dimensionless variable $x = r/l_B$, ensures that $g(x)$ obeys the normalisation condition $\int_0^\infty g(x)xdx = 1$. The pair distribution function gives the distribution of interelectron distances. The figure shows that in the presence of the magnetic field overshoot, the interelectron distance is less than the interelectron distance for the system without a magnetic field overshoot. From the figure it is seen that the pair distribution function is finite for an interelectron distance equal to zero. The reason for this is that the ground state of this system is spin unpolarised ($S = 0$), hence the electrons have different spin quantum numbers.

To visualise the states of a magnetic quantum dot further, the pair correlation function is introduced. The definition of the pair correlation function, $P(\mathbf{r}, \mathbf{r}')$, follows from the convention used by Maksym [40], and is proportional to

$$\left\langle \sum_{i \neq j} \delta\left(\mathbf{r} - \mathbf{r}_i\right) \delta\left(\mathbf{r}' - \mathbf{r}_j\right) \right\rangle. \tag{4.15}$$

The pair correlation function gives the probability of finding an electron at position $\mathbf{r}$, given that there is one at position $\mathbf{r}'$, and is normalised in the way described by Maksym [40]. The position, $\mathbf{r}'$, of the fixed electron is chosen to be the position of the maximum value of the electron density.

The pair correlation function for a GaAs system, with and without a magnetic field overshoot at r_o, for $B_z = 9.5$ T and $r_o = 30$ nm is shown in figure 4.9. The top frame shows the pair correlation function for a system without a magnetic field overshoot at r_o, while the bottom frame shows the pair correlation function for a system with a magnetic field overshoot. The axes for the pair correlation

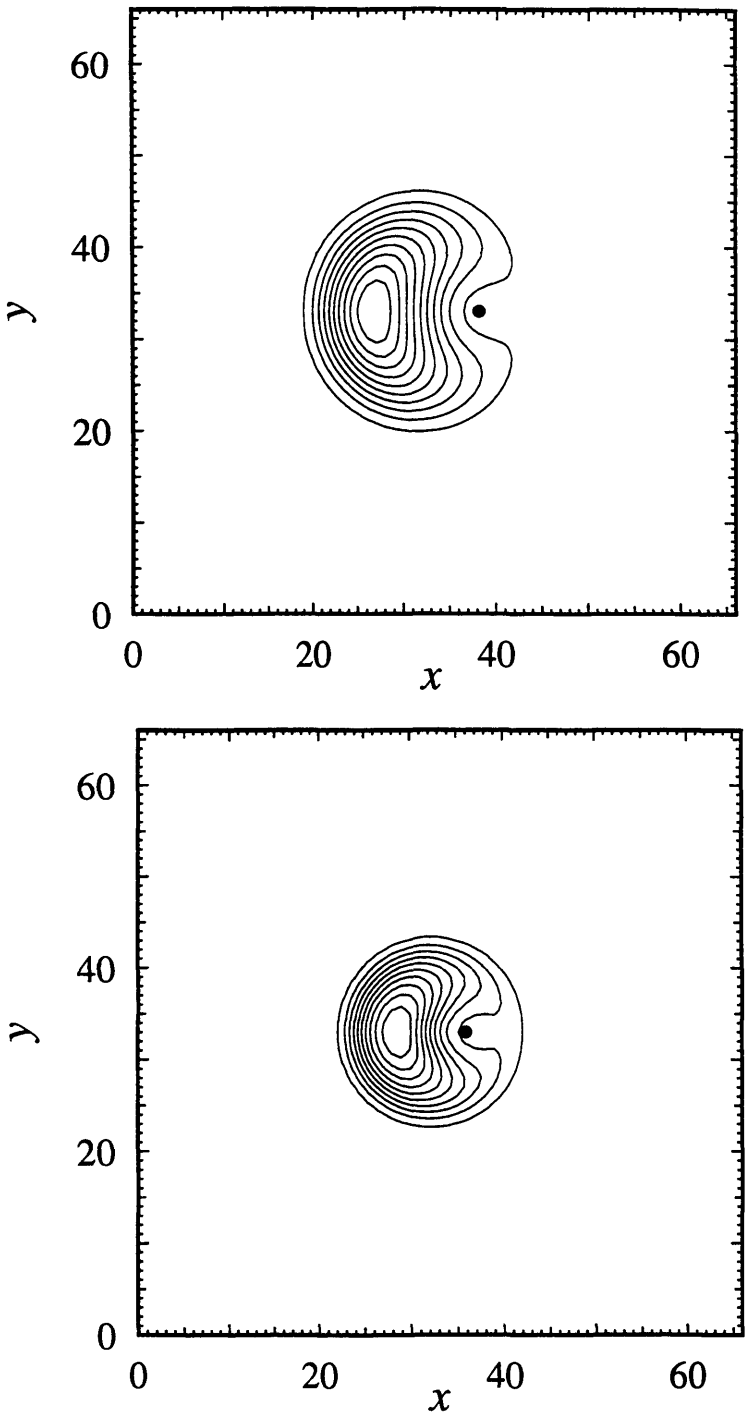

Figure 4.9: Pair correlation function for a GaAs magnetic quantum dot, with (bottom) and without (top) a magnetic field overshoot. The black spot indicates the position of the fixed electron. The confining magnetic field is $B_z = 9.5$ T and the magnetic quantum dot radius is $r_o = 30$ nm.

plots are graduated in steps of length $l_B/3$, with the origin at the centre of each plot. The black spots in the frames indicate the position of the fixed electron, $\mathbf{r}'$. For the system with a magnetic field overshoot at r_o (bottom frame in the figure), it is seen that pair correlation function has a sharp peak. This peak indicates the most probable position of the second electron, and it is seen that the most probable separation between the electrons is relatively small. The structure seen in the top frame of figure 4.9, which is for a system without a magnetic field overshoot at r_o, is less sharp. It is also observed that the most probable electron separation is greater than for the system with a magnetic field overshoot. Again, this verifies the electron density and pair distribution results, and indicates that the electrons are localised more strongly inside the magnetic quantum dot when the magnetic field overshoot at r_o is present.

4.4.4 Stability Results for a InSb System

To determine the effect of the material parameters on the stability of the system, the stability results are recalculated for an InSb magnetic quantum dot. The material parameters are the effective mass, the relative permittivity and effective g factor. InSb has an effective mass, m^*, of $0.014m_e$ and a relative permittivity of 17. For this material the effective g factor is not a constant, but is found to depend on the magnetic field [41]. This dependence is included in the calculation and the form of the dependence is approximated by $g^* = -(51 - 1.7B_z)$. By choosing a material with these parameters values, the energy outside the magnetic quantum dot, due to the magnetic field, will increase due to the smaller effective mass in InSb. Therefore it is expected that the stability of this system will be enhanced. The results are obtained in exactly the same way as for the GaAs system, and

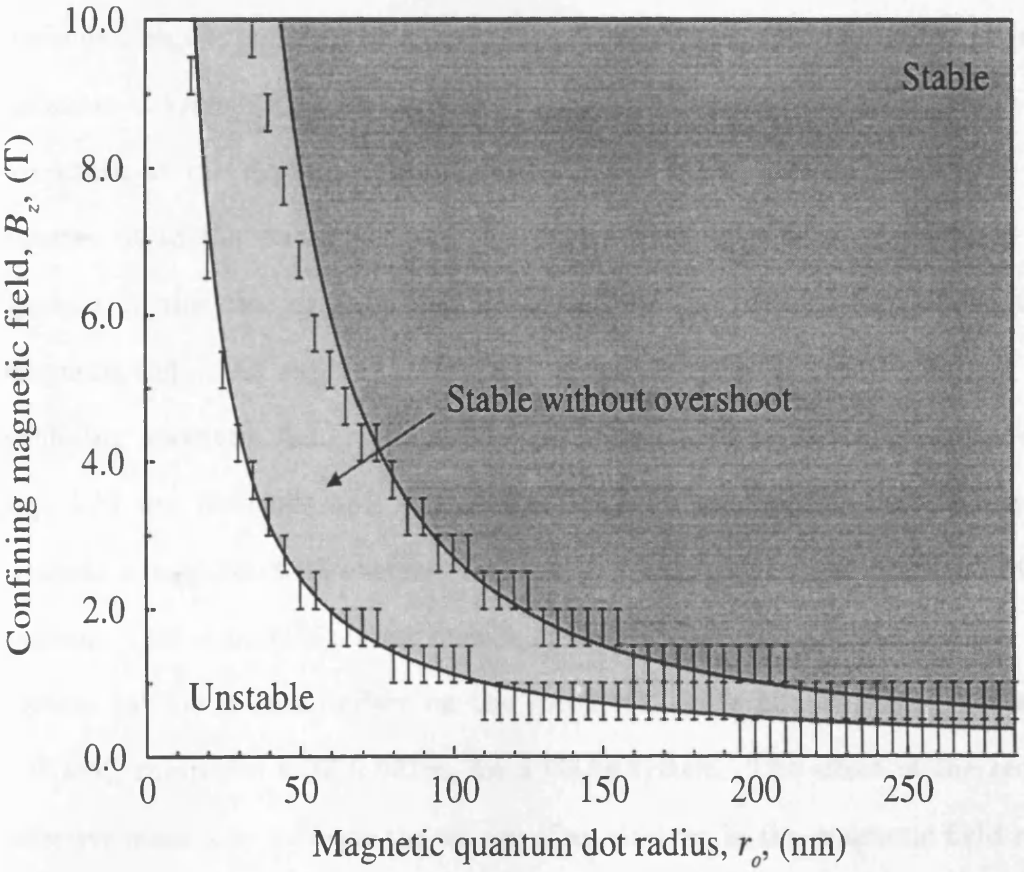

Figure 4.10: Stability as a function of the system parameters for a InSb magnetic quantum dot with and without a magnetic field overshoot at r_o. The solid curves are the result of a least squares fit to the numerical data.

again seventeen Landau levels are included in the calculation, to obtain energies that are accurate to better than 4%.

Figure 4.10 shows the stability boundaries for a InSb magnetic quantum dot, with and without a magnetic field overshoot at r_o, as a function of the system parameters. The dark shaded region indicates a system that is stable, while the unshaded region indicates a system that is unstable. The light shaded region indicates a system that is unstable only in the presence of the magnetic field overshoot at r_o. Again, the solid curves in the figure are the result of a least squares fit to the numerical data. It is seen that the fit is excellent for both systems in the case of large magnetic quantum dot radii and small confining magnetic field. As expected, for small magnetic quantum dot radii and large confining magnetic field, the fit deviates from the data because h_0 and h_0' in Eq. 4.13 are not constant. From the figure it is observed that the system without a magnetic field overshoot at r_o is more stable than the equivalent GaAs system. This is mainly a consequence of the reduced effective mass in the InSb system (g^* has a small effect on the stability). InSb has an effective mass of $0.014m_e$, compared with $0.067m_e$ for a GaAs system. The effect of the reduced effective mass is to increase the energy of an electron in the magnetic field region ($\hbar eB_z/2m^*$). For example, for a system with $B_z = 5$ T, the energy due to the magnetic field increases from 4.32 meV for the GaAs system, to 20.68 meV for the InSb system. Therefore the energy of the system for infinite J, E_∞, increases, thus enhancing the stability of the system.

4.5 A System in an External Magnetic Field

In this section, the effect of adding a homogeneous external magnetic field, B_{ext}, to a GaAs magnetic quantum dot containing two interacting electrons without a magnetic field overshoot at r_o is investigated. The addition of a homogeneous external magnetic field to the system, alters the hamiltonians, for the single electron inside and outside the magnetic quantum dot, therefore a new form for the single particle matrix elements has to be determined. Of course, these matrix elements depend on the form of the single particle function that is used to calculate them, and in turn the single particle functions are a function of the magnetic field via the magnetic length parameter, l_B. The introduction of the external magnetic field, B_{ext}, in the system, raises the question of which magnetic field to choose to represent the magnetic length parameter. Because there are two magnetic fields present in the system, it is possible to express the magnetic length as a function of B_z, as a function of B_{ext}, or as a function of some combination of the two magnetic fields. Therefore there are several possible forms for the single particle function. The single particle function that is used to calculate the single electron matrix elements, is the one that gives the best convergence of the energy eigenvalues. By performing tests to determine the optimum form of single particle function, it is found that the single particle function with magnetic length parameter $l_B = \sqrt{\hbar/e(B_z + B_{\text{ext}})}$ gives the best convergence. For example, the energies of a spin unpolarised, two electron, GaAs magnetic quantum dot with $J = 0$, $r_o = 30$ nm, $B_z = 2$ T, and $B_{\text{ext}} = 5$ T for a calculation including nine Landau levels are accurate to 0.016% with $l_B = \sqrt{\hbar/e(B_z + B_{\text{ext}})}$, 0.025% with $l_B = \sqrt{\hbar/eB_{\text{ext}}}$ and 0.2% with $l_B = \sqrt{\hbar/eB_z}$. Similar accuracies are also obtained for calculations with $B_{\text{ext}} < B_z$.

4.5.1 Calculation of the Single Electron Matrix Elements

To calculate the single electron matrix elements, a method similar to that described in chapter 3 is used. The hamiltonian for a single electron in the region, $r < r_o$ is given by

$$h_{r<r_o} = -\frac{\hbar^2\nabla^2}{2m^*} + \frac{m^*\omega_{\text{ext}}^2 r^2}{8} - \frac{\hbar\omega_{\text{ext}} l}{2} + g^*\mu_B S_z B_{\text{ext}}, \tag{4.16}$$

where $\omega_{\text{ext}} = eB_{\text{ext}}/m^*$. In the region $r > r_o$, the hamiltonian is no longer given by Eq. 2.2, because there is an additional vector potential, $A_{\text{ext}}(r) = B_{\text{ext}}r/2$, as a result of the external magnetic field. The hamiltonian for the region outside the magnetic quantum dot becomes

$$\begin{aligned} h_{r>r_o} &= -\frac{\hbar^2\nabla^2}{2m^*} + \frac{m^* r^2}{8}(\omega_c^2 + \omega_{\text{ext}}^2) - \frac{\hbar l}{2}(\omega_c + \omega_{\text{ext}}) + \frac{\hbar\omega_c l r_o^2}{2r^2} - \frac{m^*\omega_c^2 r_o^2}{4} \\ &+ \frac{m^*\omega_c^2 r_o^4}{8r^2} + \frac{m^*\omega_c\omega_{\text{ext}} r^2}{4} - \frac{m^*\omega_c\omega_{\text{ext}} r_o^2}{4} + g^*\mu_B S_z(B_z + B_{\text{ext}}). \end{aligned} \tag{4.17}$$

The matrix elements are determined by substituting this equation along with Eq. 4.16, the single particle function (Eq. 2.13) and the dimensionless variable $x = r^2/2l_B^2$, where $l_B = \sqrt{\hbar/e(B_z + B_{\text{ext}})}$, into Eq. 2.11, giving

$$\begin{aligned} \langle i|h|j\rangle &= \delta_{ll'}\left\{\frac{\hbar^2}{4m^* l_B^2}\left[(2n + |l| + 1)\delta_{nn'} + \sqrt{n(n+1)}\delta_{n'n-1}\right.\right. \\ &+ \left.\sqrt{(n+1)(n+|l|+1)}\delta_{n'n+1}\right] + \frac{l_B^2 m^*\omega_{\text{ext}}^2}{4}\left[(2n + |l| + 1)\delta_{nn'}\right. \\ &- \left.\sqrt{n(n+1)}\delta_{n'n-1} - \sqrt{(n+1)(n+|l|+1)}\delta_{n'n+1}\right] \\ &- \left[\frac{\hbar\omega_{\text{ext}} l}{2} - g^*\mu_B S_z B_{\text{ext}}\right]\delta_{nn'} + \frac{r_o^2}{l_B^2}\left[\frac{\hbar\omega_c l}{4} + \frac{m^*\omega_c^2 r_o^2}{16}\right]\lambda_n\lambda_{n'}\mathcal{I}_1 \\ &- \left[\frac{\hbar\omega_c l}{2} + \frac{m^*\omega_z^2 r_o^2}{4} + \frac{m^*\omega_c\omega_{\text{ext}} r_o^2}{4} - g^*\mu_B S_z B_z\right]\lambda_n\lambda_{n'}\mathcal{I}_2 \\ &+ \left. l_B^2\left[\frac{m^*\omega_c^2}{4} + \frac{m^*\omega_c\omega_{\text{ext}}}{2}\right]\lambda_n\lambda_{n'}\mathcal{I}_3\right\}, \end{aligned} \tag{4.18}$$

where

$$\mathcal{I}_1 = \int_{x_o}^{\infty} e^{-x} x^{|l|-1} L_{n'}^{|l|}(x) L_n^{|l|}(x) dx,$$

$$\begin{aligned} \mathcal{I}_2 &= \int_{x_o}^{\infty} e^{-x} x^{|l|} L_{n'}^{|l|}(x) L_n^{|l|}(x) dx, \\ \mathcal{I}_3 &= \int_{x_o}^{\infty} e^{-x} x^{|l|+1} L_{n'}^{|l|}(x) L_n^{|l|}(x) dx. \end{aligned} \tag{4.19}$$

The integrals in this equation are evaluated numerically using a routine obtained from the NAG library. The routine, which is also used in chapter 3 to evaluate the single particle matrix elements, is based on a modified Gauss-Laguerre procedure, and is exact for an integral with a finite lower limit. Each of the integrands are evaluated at 32 points, giving results that are accurate to roughly seven decimal places. The accuracy of the results is verified by comparing the obtained results with those calculated with Maple.

4.5.2 Results

The effect of the additional external magnetic field on the stability of a GaAs magnetic quantum dot without a magnetic field overshoot at r_o is shown in figure 4.11. The results are obtained as described in the previous sections, and again seventeen Landau levels are included in the numerical diagonalisation calculation, to obtain energies accurate to at least 4%. The figure shows the stability boundaries for a GaAs magnetic quantum dot without a magnetic field overshoot at r_o, with and without an additional external magnetic field of $B_{\text{ext}} = 5$ T. The dark shaded region indicates a system that is stable, while the unshaded region indicates a system that is unstable. The light shaded region indicates a system that is stable only in the presence of the external magnetic field. The solid curves in the figure are the result of a least squares fit to the numerical data. From the figure it is seen that the system in an external magnetic field is more stable than the corresponding system without an external magnetic field. The reason for this can be explained by referring to the stability condition (Eq. 4.13). First

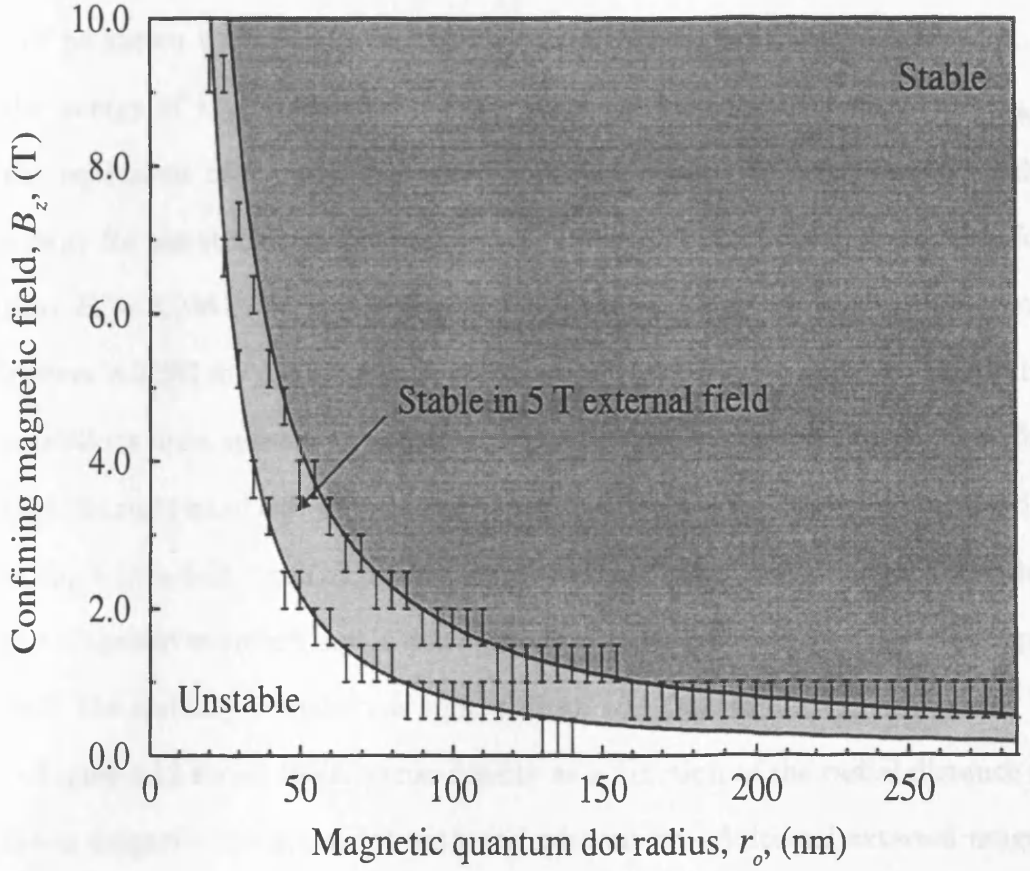

Figure 4.11: Stability as a function of the system parameters for a GaAs magnetic quantum dot with and without an additional external magnetic field of $B_{\text{ext}} = 5$ T. The solid curves are the result of a least squares fit to the numerical data.

the energy of the system at infinite J is determined. In a homogeneous external magnetic field, the energy of the electron inside the magnetic quantum dot tends to $\hbar\omega_{\text{ext}}/2$, and so $E_\infty \sim \hbar\omega_{\text{ext}} + \hbar\omega_c/2$. The energy of the system at finite J is $E \sim \hbar\omega_{\text{ext}} + E_c$, where E_c is the energy due to the Coulomb interaction between the electrons. By equating E and E_∞ the stability condition is obtained, and can be shown to be $\hbar eB_z/2m^* \sim E_c$. Therefore under the approximation that the energy of the electron inside the magnetic quantum dot tends to $\hbar\omega_{\text{ext}}/2$, the equivalent of the first term in Eq. 4.13 cancels. Calculating the Coulomb energy for the stable system $B_{\text{ext}} = 5$ T, $B_z = 7.5$ T and $r_o = 30$ nm, it is found that $E_c = 3.036$ meV, while the Coulomb energy of the corresponding unstable system is 2.282 meV, a change of approximately 25%. By comparing the stability conditions for a system with and without an external magnetic field, it is found that the right hand side of $\hbar eB_z/2m^* \sim E_c$ is 3.036 meV, while the right hand side of Eq. 4.13 is 6.082 meV. Therefore, because the energy of the electrons inside the the magnetic quantum dot is decreased in the presence of the external magnetic field, the stability boundary is shifted down and the stability is enhanced.

Figure 4.12 shows the electron density as a function of the radial distance for a GaAs magnetic quantum dot with and without an additional external magnetic field of $B_{\text{ext}} = 5$ T. The confining magnetic field is $B_z = 7.5$ T and the magnetic quantum dot radius is $r_o = 30$ nm. The solid curve in the figure indicates the results obtained for a system in an additional external magnetic field, while the dashed curve indicates the results obtained for a system without an external magnetic field. From the figure it is seen that the effect of the external magnetic field is to localise the electrons more strongly inside the magnetic quantum dot (the vertical dotted line indicates the position of r_o). The solid curve also shows

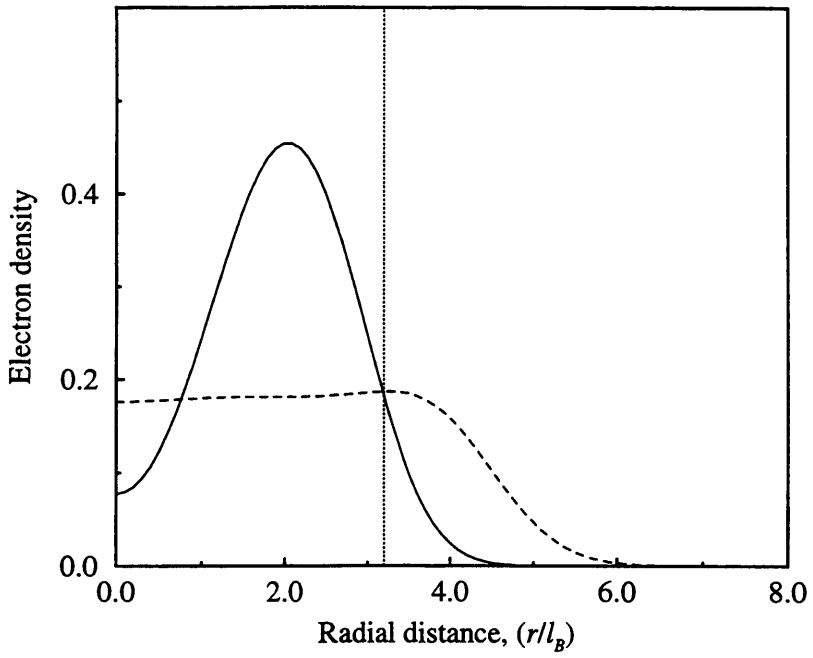

Figure 4.12: Electron density as a function of the radial distance for a GaAs magnetic quantum dot containing two interacting electrons. The solid curve indicates the results obtained for a system with an additional external magnetic field of $B_{\text{ext}} = 5$ T, and the dashed curve indicates the results obtained for a system without an additional external magnetic field. The confining magnetic field is $B_z = 7.5$ T and the magnetic quantum dot radius is $r_o = 30$ nm.

that the electron density has a well defined peak, indicating the most probable radial distance of the two electron wave function. The electron density for the system without an external magnetic is observed from the figure to be roughly constant, with no well defined peak, inside the magnetic quantum dot. As the radial distance increases further, the electron density gradually decreases to zero.

The pair distribution function as a function of the radial distance for a GaAs system without a magnetic field overshoot at r_o, with and without an external magnetic field is shown in figure 4.13. Again, the results are calculated for a stable system with $B_z = 7.5$ T, $r_o = 30$ nm and $B_{\text{ext}} = 5$ T, and an unstable

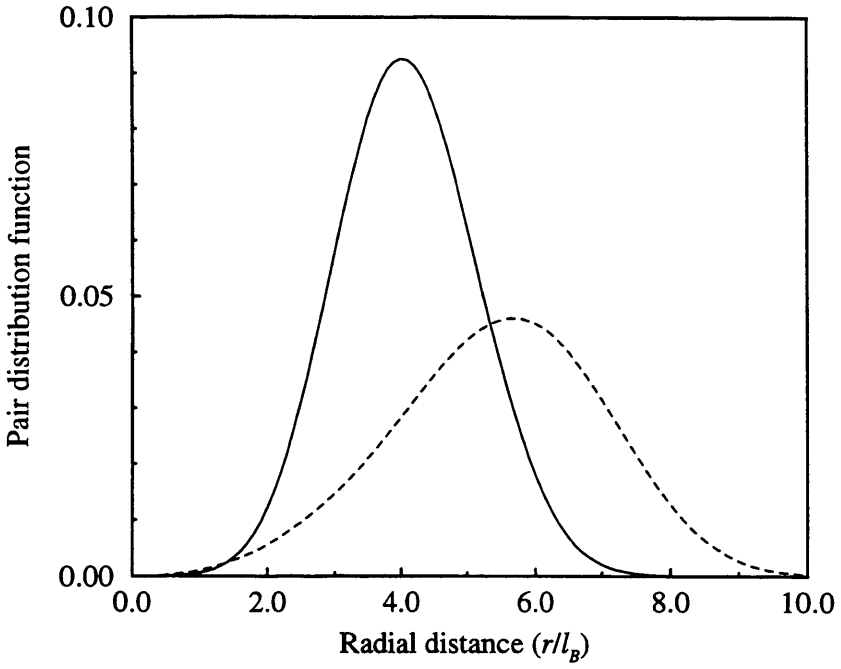

Figure 4.13: Pair distribution function as a function of the radial distance for a GaAs magnetic quantum dot. The solid curve indicates the results obtained for a system with an additional external magnetic field of $B_{\text{ext}} = 5$ T, and the dashed curve indicates the results obtained for a system without an additional external magnetic field. The confining magnetic field is $B_z = 7.5$ T and the magnetic quantum dot radius is $r_o = 30$ nm.

system with $B_z = 7.5$ T, $r_o = 30$ nm and $B_{\text{ext}} = 0$ T. The solid curve in the figure shows the results obtained for a system in an external magnetic field, while the dashed curve shows the results obtained for a system without an external magnetic field. The figure shows that for the system in an external magnetic field, the average interelectron separation is less than for the system without an external magnetic field. It is seen that in the presence of the external magnetic field, the interelectron distance decreases by roughly 25%. This is consistent with the increase in the calculated Coulomb energy for the stable and unstable systems.

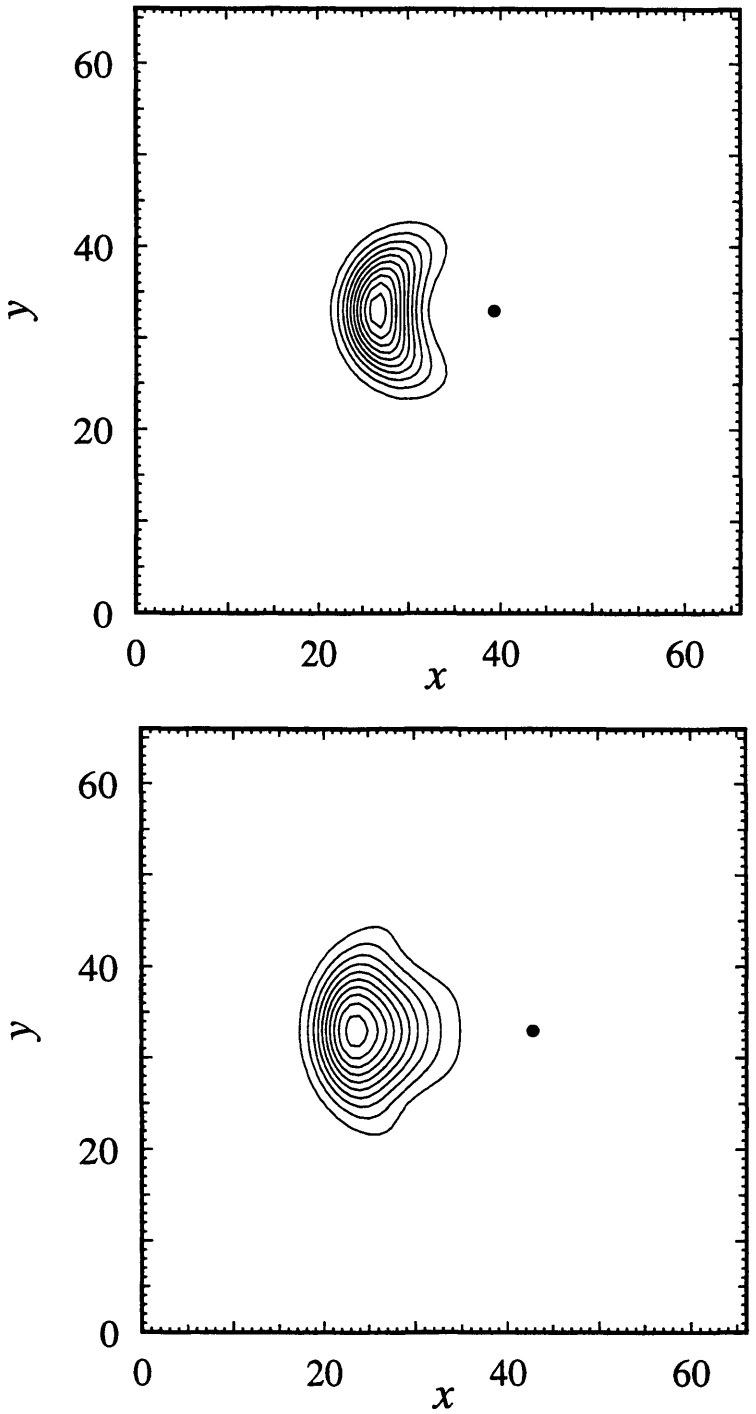

Figure 4.14: Pair correlation function for a GaAs magnetic quantum dot, with (top) and without (bottom) an additional external magnetic field of $B_{\text{ext}} = 5$ T. The black spot indicates the position of the fixed electron. The confining magnetic field is $B_z = 7.5$ T and the magnetic quantum dot radius is $r_o = 30$ nm.

The pair correlation function for a GaAs system without a magnetic field overshoot at r_o, with and without an external magnetic field is shown in figure 4.14. The top frame shows the pair correlation for the stable system with $B_z = 7.5$ T, $r_o = 30$ nm and $B_{\text{ext}} = 5$ T, while the bottom frame shows the corresponding unstable system with $B_{\text{ext}} = 0$ T. The axes for the pair correlation plots are graduated in steps of length $l_B/3$, where $l_B = \sqrt{\hbar/eB_z}$, with the origin at the centre of each plot. The black spots indicate the position of the fixed electron, $\mathbf{r}'$. The position, $\mathbf{r}'$, of the fixed electron is chosen to be the position of the maximum value of the electron density. From the figure it is observed that the pair correlation plot for the system in an external magnetic field has a compact sharp structure. This indicates that the electrons have a fairly well defined separation, and this is confirmed with the solid curve in figure 4.13. The pair correlation function shown for the system without an external magnetic field (bottom frame), has a less compact structure and it is observed that the most probable separation between the two electrons is increased. This again supports the results shown in figure 4.13.

4.6 Towards a More Realistic System

In this section a GaAs magnetic quantum dot without a magnetic field overshoot at r_o, with an electron layer of finite thickness is considered. The model considered is that in which a 2DEG is formed in a standard AlGaAs-GaAs heterostructure. Further, it is assumed that the donors in the AlGaAs layer are fully ionised, and therefore the number of electrons in the 2DEG is equal to the number of donor charges in the AlGaAs layer. To deplete the electrons in the 2DEG it is suggested that a gate is deposited on top of the device. If this

gate is uniform throughout the device, the electron density should be decreased everywhere in the system. Alternatively, a modulated gate that keeps the electron density low in the region of the dot could also be used. It is expected that the stability of such a system will be enhanced due to the extra degree of freedom available to the electrons, as compared to the stability of a GaAs system with an electron layer of infinitely small thickness. This section is organised as follows. First, the necessary modifications to the hamiltonian due to this extra degree of freedom, are made, and a wave function that describes the motion of the electrons in the perpendicular direction is introduced. This allows the single electron matrix elements and the Coulomb matrix elements to be calculated for this system. Given the form of the matrix elements, a numerical diagonalisation calculation is performed and the stability of the system is determined. Finally, a brief discussion of other effects expected in a more realistic system is given, and the consequences that these effects have on the stability of the system are speculated upon.

4.6.1 Theoretical Treatment

With the motion of the electrons not limited to the $x-y$ plane, the hamiltonian for the system is given by

$$H = \sum_{i=1}^{N} h(\mathbf{r}_i, z_i) + \frac{1}{2}\sum_{i=1}^{N}\sum_{\substack{j=1 \\ j\neq i}}^{N} v(\mathbf{r}_i, z_i, \mathbf{r}_j, z_j), \tag{4.20}$$

where z is the co-ordinate in the direction perpendicular to the plane $x-y$. The first term in this equation gives the single particle energy of the system, while the second term describes the Coulomb interaction between the electrons. The transformation to an occupation number representation gives an equation similar

to Eq. 2.10

$$H = \sum_{i,j} \langle i|h|j\rangle c_i^\dagger c_j + \frac{1}{2} \sum_{i,j,k,l} \langle ij|v|kl\rangle c_i^\dagger c_j^\dagger c_l c_k, \tag{4.21}$$

where h and v now depend on z. To obtain the energy eigenvalues of the system, the N-electron hamiltonian, given by this equation, is diagonalised. The explicit form of the matrix elements are given by

$$\langle i|h|j\rangle = \int \psi_i^*(\mathbf{r}, z) h(\mathbf{r}, z) \psi_i(\mathbf{r}, z) d\mathbf{r} dz \tag{4.22}$$

and

$$\begin{aligned} \langle ij|v|kl\rangle &= \int\int \psi_i^*(\mathbf{r}_1, z_1) \psi_j^*(\mathbf{r}_2, z_2) v(\mathbf{r}_1, z_1, \mathbf{r}_2, z_2) \\ &\times \psi_k(\mathbf{r}_1, z_1) \psi_l(\mathbf{r}_2, z_2) d\mathbf{r}_1 dz_1 d\mathbf{r}_2 dz_2. \end{aligned} \tag{4.23}$$

The single particle functions that are required to calculate these matrix elements are chosen to be separable, and are given by

$$\psi_i(\mathbf{r}, z) = \psi_i(\mathbf{r}) \chi_i(z), \tag{4.24}$$

where, again, the in plane functions, $\psi_i(\mathbf{r})$, are chosen to be the Fock-Darwin states, and these are given by Eq. 2.13. The single particle functions, $\chi_i(z)$, that describe the electron motion perpendicular to $\mathbf{r}$, are chosen to be the Fang-Howard states [42, 43]. These states have the form

$$\chi(z) = \left(\frac{b^3}{2}\right)^{\frac{1}{2}} z e^{-bz/2}, \tag{4.25}$$

where b is a variational parameter, that is determined by minimising the energy of the system. Strictly, b is determined by minimising the total energy of the system; this includes the parallel and perpendicular components of the single electron energy and Coulomb energy. However, in section 4.6.4 an analysis of the total energy of the system, and its dependence on b is undertaken, and consequently

a simple approximation is introduced, allowing b to be determined much more easily. Given the form of the single particle functions it is now possible to calculate the matrix elements.

4.6.2 Calculation of the Single Electron Matrix Elements

With the inclusion of a third dimension in the problem, the single electron hamiltonian for the system is written as

$$h(\mathbf{r}, z) = h(\mathbf{r}) + h(z), \tag{4.26}$$

where $h(\mathbf{r})$ is the in plane hamiltonian given by Eq. 3.1 and Eq. 3.4, and $h(z)$ is the hamiltonian describing the electron motion perpendicular to the plane, and is given by

$$h(z) = -\frac{\hbar^2}{2m^*}\frac{\partial^2}{\partial z^2} + U(z). \tag{4.27}$$

The function $U(z)$ in this equation, is the confining potential perpendicular to the plane. The potential is approximated by an infinite barrier for $z < 0$, and by $U(z) = e^2 N_{2\text{DEG}} z/\epsilon\epsilon_o$ [44] for $z > 0$, where $N_{2\text{DEG}}$ is the number of electrons per unit area in the 2DEG. Because the hamiltonian separates, in the way given in Eq. 4.26, the modification to the single electron matrix elements, due to motion of the electrons perpendicular to the plane, is calculated by evaluating the integral

$$\int_0^\infty \chi^*(z)\left[-\frac{\hbar^2}{2m^*}\frac{\partial^2}{\partial z^2} + \frac{e^2 N_{2\text{DEG}} z}{\epsilon\epsilon_o}\right]\chi(z)dz, \tag{4.28}$$

giving the contribution to the single electron matrix elements, due to the perpendicular motion of the electrons as

$$E_\perp = \frac{\hbar^2 b^2}{8m^*} + \frac{3e^2 N_{2\text{DEG}}}{\epsilon\epsilon_o b}. \tag{4.29}$$

The integral over $\mathbf{r}$ in Eq. 4.22 has already been calculated, and the details of this calculation are given in chapter 3.

4.6.3 Calculation of the Coulomb Matrix Elements

The Coulomb interaction between a pair of electrons located at $(\mathbf{r}_1, z_1)$ and $(\mathbf{r}_2, z_2)$ is given by

$$v(\mathbf{r}_1, z_1, \mathbf{r}_2, z_2) = \frac{e^2}{4\pi\epsilon\epsilon_o} \frac{1}{\sqrt{[(\mathbf{r}_1 - \mathbf{r}_2)^2 + (z_1 - z_2)^2]}}. \tag{4.30}$$

The modified Coulomb matrix elements are calculated by taking the Fourier transform of this new interaction potential. By doing this and substituting the result, along with Eq. 4.24 into Eq. 4.23, the Coulomb matrix elements are found to separate into $\mathbf{r}$ and z dependent parts, giving

$$\begin{aligned} \langle ij|v|kl\rangle &= \frac{e^2}{8\pi^2\epsilon\epsilon_o} \int_0^\infty d\mathbf{q} \int_0^\infty \psi_i^*(\mathbf{r}_1)\psi_j^*(\mathbf{r}_2) \frac{e^{i\mathbf{q}\cdot(\mathbf{r}_1-\mathbf{r}_2)}}{|\mathbf{q}|} \psi_k(\mathbf{r}_1)\psi_l(\mathbf{r}_2) d\mathbf{r}_1 d\mathbf{r}_2 \\ &\times \int_0^\infty \chi^*(z_1)\chi^*(z_2) e^{-q|z_1-z_2|} \chi(z_1)\chi(z_2) dz_1 dz_2. \end{aligned} \tag{4.31}$$

The integral over z in this equation is known as the form factor, $F(q)$ [43], and gives the modification to the Coulomb matrix elements, due to the electron motion perpendicular to plane. The form factor has been evaluated by Ando *et al* [43] for a system in which a semiconductor with dielectric constant ϵ_{sc} fills the space $z > 0$, and an insulating medium of dielectric constant ϵ_{ins} fills the space $z < 0$. If it is assumed that the electrons occupy the same material, then $\epsilon_{sc} = \epsilon_{ins}$ and the expression calculated by Ando *et al* [43] reduces to the following

$$F(q) = \frac{1}{8}\left(1 + \frac{q}{b}\right)^{-3}\left(8 + 9\frac{q}{b} + 3\frac{q^2}{b^2}\right). \tag{4.32}$$

Therefore multiplying the existing expressions for the Coulomb matrix elements (Eq. 4.2, Eq. 4.5 and Eq. 4.6) by $F(q)$, the electron motion perpendicular to the plane is taken into account.

4.6.4 Determining the Variational Parameter, b

To determine the variation parameter, b, the total energy of the system is minimised. To achieve this, the total energy of the system is differentiated with respect to b, and the subsequent result is set to zero, allowing the variational parameter to be determined. However, the form factor, $F(q)$, can be shown to result in a modified Coulomb energy that is roughly constant as a function of b. Figure 4.15 shows a typical example of the total energy of the system as a function of the variational parameter b, and the total energy without the contribution due to the single electron energy perpendicular to the plane, $E_\perp$, as a function of b. The solid curve shows the total energy of the system as a function of b, while the dashed curve shows the total energy without the contribution due to the single electron energy perpendicular to the plane as a function of b. The results shown by the dashed curve have been scaled by a factor of ten in order to compare the data more easily. The data is obtained for a two electron system with $J = 0$, $S = 0$, $B_z = 5$ T and $r_o = 30$ nm, using the numerical diagonalisation routine with six Landau levels included in the calculation to obtain energies accurate to roughly 0.01% throughout the b range. The number of electrons per unit area in the 2DEG, N_{2DEG}, is taken to be 3.0×10^{10} cm^{-2} [35]. The solid curve in the figure shows the presence of an energy minimum as a function of the variational parameter, b. The dashed curve, which shows the total energy without the contribution due to the single electron energy perpendicular to the plane, shows no minimum, and is very nearly constant throughout the b range. The only b dependent term present in the energy shown by the dashed curve is the form factor $F(q)$, hence this term is approximated as constant, and is therefore independent of b. Upon making this assumption, b is found by minimising the

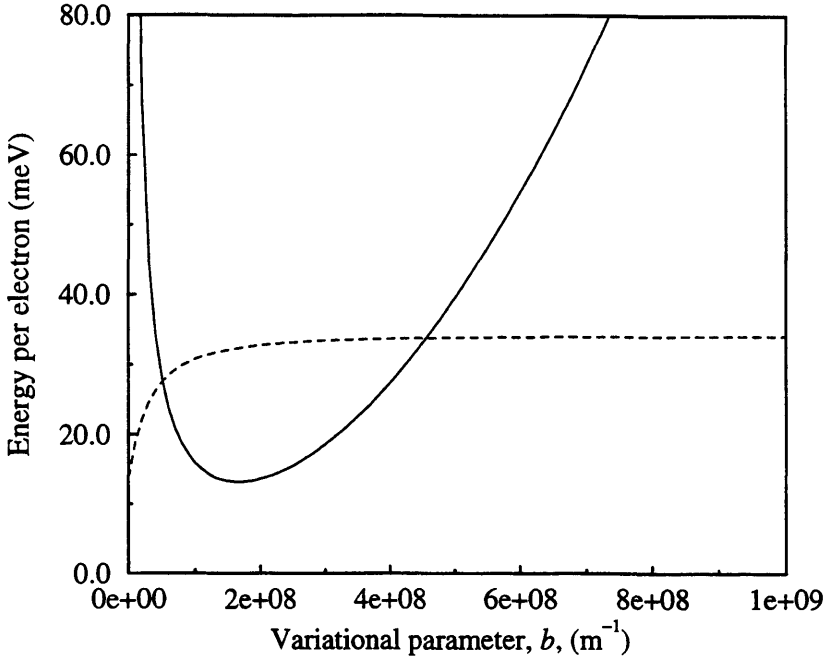

Figure 4.15: Energy as a function of the variational parameter, b. The solid curve shows the total energy as a function of b, while the dashed curve shows the total energy without the contribution due to the single electron energy perpendicular to the plane as a function of b.

single electron energy perpendicular to the plane, thus

$$\frac{\hbar^2 b}{4m^*} - \frac{3e^2 N_{2\text{DEG}}}{\epsilon\epsilon_o b^2} = 0. \tag{4.33}$$

Therefore the variational parameter, b, that minimises the energy can be shown to be

$$b = \left(\frac{12m^* e^2 N_{2\text{DEG}}}{\hbar^2 \epsilon\epsilon_o}\right)^{\frac{1}{3}}. \tag{4.34}$$

Using the value of $N_{2\text{DEG}}$ already given, the variational parameter that minimises the energy is $b = 0.167 \times 10^9$ m^{-1}. This corresponds to an average width in the perpendicular direction of roughly 18 nm.

4.6.5 Results

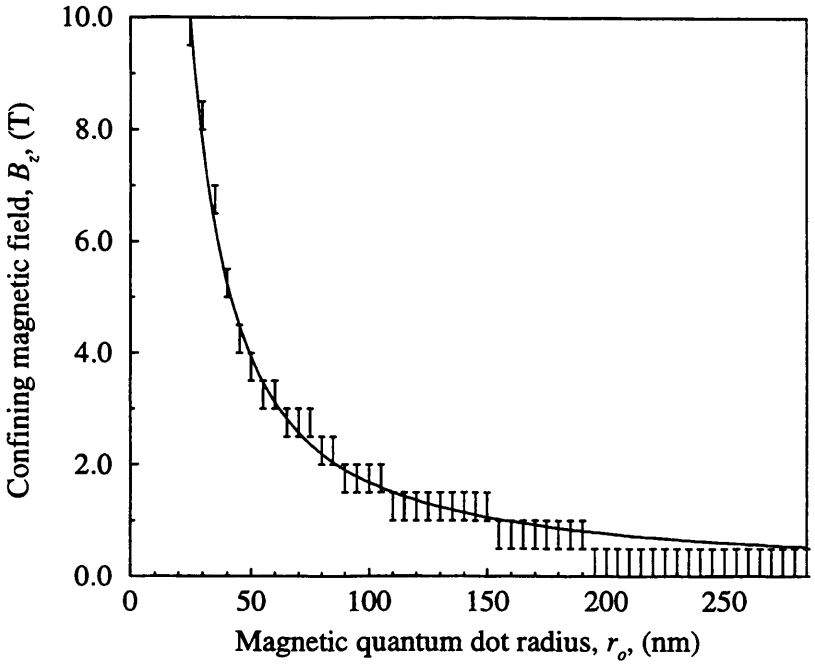

Figure 4.16: Stability as a function of the system parameters for a GaAs system without a magnetic field overshoot at r_o, with an electron layer of finite thickness. The solid curve is the result of a least squares fit to the data.

In this section the stability of a GaAs system without a magnetic field overshoot at r_o, with an electron layer of finite thickness, and the stability of the equivalent system with an electron layer of infinitely small thickness are compared. In figure 4.16 the stability boundary for a GaAs system without a magnetic field overshoot at r_o, with an electron layer of finite thickness is shown. The solid curve in the figure is the result of a least squares fit to the data given by the error bars. Again, seventeen Landau levels are included in the numerical diagonalisation calculation to obtain energies accurate to better than 4%. From the figure it is seen that the fit (shown by the solid curve) is excellent throughout the range of the data, and deviates only slightly from the data for a system with small

confining magnetic field and large magnetic quantum dot radii. This deviation is thought to be a result of the low resolution of the confining magnetic field points.

The solid curve is shown, along with the result of the least squares fit to the data calculated for the system with an electron layer of infinitely small thickness in figure 4.17. The dark shaded region indicates a system that is stable, while the unshaded region indicates a system that is unstable. The light shaded region indicates a system that is stable only if an electron layer of finite thickness is considered. The error bars are omitted from the figure to avoid confusion from overlaying points. From the figure it is seen the system with an electron layer of finite thickness is more stable than the equivalent system with an electron layer of infinitely small thickness. The figure shows that the stability of the system with an electron layer of finite thickness is enhanced slightly, and no enhancement of the stability is predicted for systems with large radii. The reason for the enhanced stability is determined by comparing the Coulomb energies of the systems. First, the system with parameters $B_z = 9.5$ T and $r_o = 30$ nm is considered. This system is stable for both systems with an electron layer of infinitely small thickness and an electron layer of finite thickness. For the system with an electron layer of finite thickness, the Coulomb energy is found to be 3.64 meV, while the Coulomb energy for the system with an electron layer of infinitely small thickness is 3.74 meV, a change of roughly 2.7%. The additional contribution to the single electron energy, due to the finite thickness of the electron layer, is found to cancel on equating E and E_∞ to obtain the stability condition. Therefore the single electron energy of the system is not expected to affect the form of the stability curve. Hence the decrease in the Coulomb interaction energy increases the stability of the system.

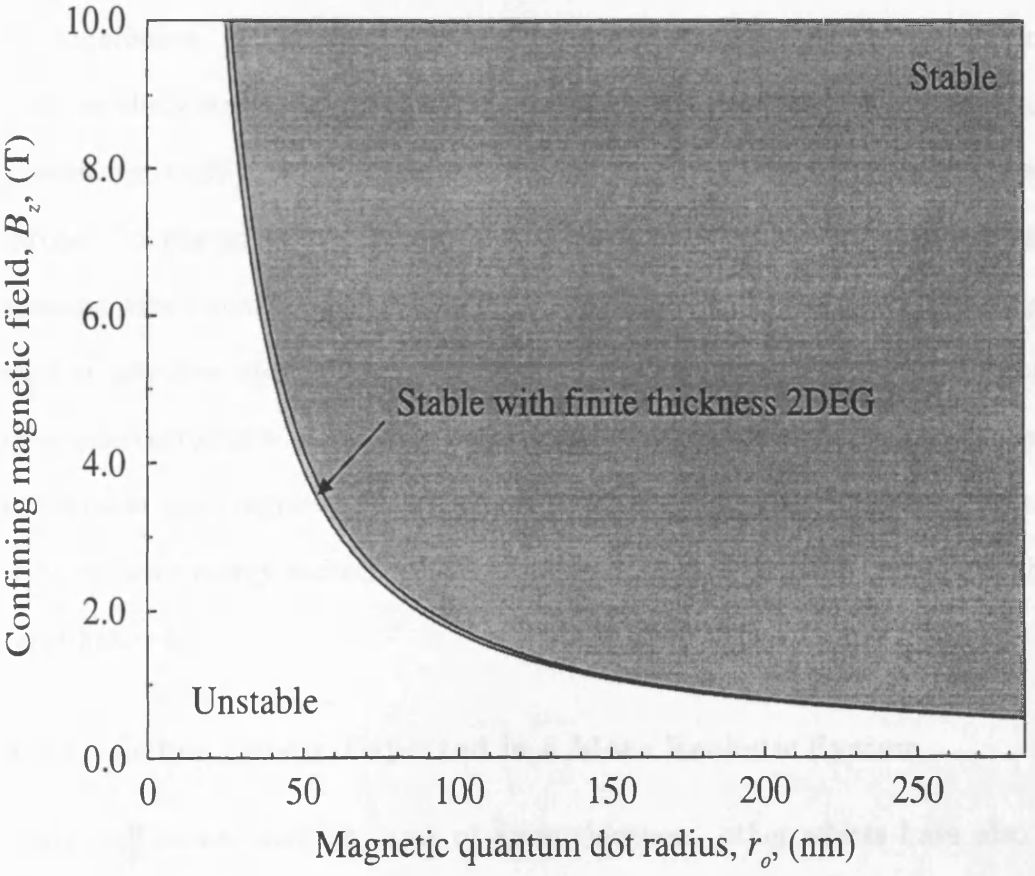

Figure 4.17: Stability as a function of the system parameters for a GaAs magnetic quantum dot without a magnetic field overshoot at r_o, with and without an electron layer of finite thickness.

From figure 4.17 it is seen that the stability of the system with an electron layer of finite thickness is not enhanced for systems with large magnetic radii. The reason for this is because as r_o increases, the electron separation tends to the in plane separation (roughly $2r_o$, if the electrons are diametrically opposite), and therefore the vertical separation of the electrons (roughly 18 nm) becomes less significant. Hence there is no enhancement of the stability of the system.

If the electrons in the magnetic quantum dot are confined in the z direction by a quantum well, it is expected that the stability of the system will be enhanced further. In the paper by Brey *et al* [45], the authors propose that quantum well systems with a thickness of greater than 2000 Å can be achieved. This is compared with an effective width of roughly 200 Å for a system in which the 2DEG is formed in a heterostructure. Therefore because the electrons in a quantum well are able to increase their separation to a distance greater than that in a heterostructure, the Coulomb energy should decrease further and the stability of the system should be enhanced.

4.6.6 Other Effects Expected in a More Realistic System

As well as an electron layer of finite thickness, other effects have also been predicted in more realistic systems. For example, electrons in electrostatic quantum dots induce charges on adjacent electrodes [46]. This influences the total energy of the system via two effects. First, there is a shift in the total energy of the system caused by the interaction of each electron with its own image charge, and second, the induced charges screen the Coulomb interaction between the electrons. The form of this screened potential has been shown to vary as $1/r^3$ [46] when the electron separation is large. It is possible that this

effect will also occur in a magnetic quantum dot, although the effect may be somewhat different due to the geometry of the magnetic quantum dot system. If this effect is included in the calculation to determine the stability of a system, it is expected that the stability of the system would be enhanced.

In a real system the confining magnetic field is known to be less than 0.5 T [47] if the system is fabricated by depositing a ferromagnetic material near a 2DEG. Therefore much of the stability curves shown in figure 4.6, figure 4.10, figure 4.11 and figure 4.16 can be probed experimentally. These stability curves show systems that are stable with a confining magnetic field of less than 0.5 T, and therefore a magnetic quantum dot radius of greater than roughly 100 nm. Fabrication of a device with these system parameters should be possible with current technology, thus allowing direct experimental verification of the theoretical predictions made in this chapter.

4.7 More Interacting Electrons

In this section the effect of adding a third electron to the magnetic quantum dot system is described. The system investigated is a GaAs magnetic quantum dot without a magnetic field overshoot at r_o. Unfortunately, a direct comparison of the stability boundary for a two electron system with the stability boundary for a three electron system is not possible, due to the large number of basis states required for a three electron calculation. It is found that the number of basis states grows rapidly with the number of Landau levels included in a numerical diagonalisation calculation. For example, it is estimated that for a calculation including seventeen Landau levels, the order of the matrix needed to be diagonalised, would be roughly 13000. This is compared with a matrix

with an order of approximately 1000 for a two electron calculation. The current numerical diagonalisation routine used to calculate the energy eigenvalues is capable of diagonalising matrices with a maximum order of roughly 5000, and it is found that the number of Landau levels that can be included in a three electron numerical diagonalisation calculation is restricted to a maximum of ten. Larger scale calculations are possible in principle but further time would be required to develop the necessary software.

Of course this restriction on the number of Landau levels included in a three electron numerical diagonalisation calculation has a consequence on the accuracy of the obtained results. For example, a calculation including nine Landau levels for a three electron system with $B_z = 6$ T, $r_o = 80$ nm, $S = 1/2$ and $J = 1$ yields results that are accurate to better than 6%. In order to obtain energy eigenvalues that are more accurate than this, results are obtained for systems with smaller magnetic quantum dot radii. Energy eigenvalues calculated for a system with a small magnetic quantum dot radius will require less basis states to become converged, and therefore the results will be more accurate. Because of this, systems with large confining magnetic fields are investigated, and consequently it is shown that a stability boundary exists and that these systems become stable for reasonably small values of the magnetic quantum dot radius.

4.7.1 Results

Although a direct comparison of the stability boundary for a two electron system with the stability boundary for a three electron system is not possible, individual systems can be compared. To determine the stability of a three electron system, a similar argument to that given in section 4.4.1 is used. The three

electron system is stable if the total energy of the electrons localised in the centre of the magnetic quantum dot, is less than the total energy of two electrons localised in the centre of the magnetic quantum dot and one electron localised at an infinite distance from the centre in the region with magnetic field. The system that is chosen for investigation is that with a confining magnetic field of $B_z = 10$ T. It is found that the ground state at finite J corresponds to a total spin quantum number of $S = 1/2$ and a total angular momentum quantum number of $J = 1$, this is also found to be the case for other systems with different system parameters. By analysing the stability of various systems with different magnetic quantum dot radii, it is found that this system becomes stable when $r_o \geq 50$ nm. The corresponding two electron system with $B_z = 10$ T becomes stable when $r_o \geq 30$ nm, so the addition of another electron to the system decreases the stability of the system. The reason for this can be determined by comparing the energy of the two electron system with the energy of the three electron system. For the two electron system with $B_z = 10$ T and $r_o = 50$ nm, the single electron energy per electron is 1.22 meV and the Coulomb energy is 1.23 meV, giving a total energy per electron of 2.45 meV. The single electron energy per electron of the corresponding three electron system is 1.81 meV, and the Coulomb energy is 2.60 meV, hence the total energy per electron for the three electron system is 4.41 meV. Therefore the total energy increases for the system with three electrons, and this is mainly a consequence of the increased Coulomb energy, hence the decrease in stability of the three electron system is caused by an increase in the total energy of the system.

The previous calculations confirm the existence of a stability boundary for the three electron system, but does this stability boundary follow the same general

trend as the stability boundary for the two electron system? The trend followed by the stability boundary of the two electron system is that as the confining magnetic field is increased, the system becomes stable at smaller values of the magnetic quantum dot radius. To determine if this also occurs for a system containing three electrons, the stability of a system with $B_z = 12$ T is investigated. Indeed, this is exactly what is found, and the system with $B_z = 12$ T becomes stable when $r_o \geq 40$ nm, compared with $r_o \geq 50$ nm for the system with $B_z = 10$ T.

To investigate the stable and unstable states of the three electron system, the electron density, the pair distribution and the pair correlation functions of the stable system with $B_z = 10$ T and $r_o = 50$ nm, are compared with the corresponding unstable system with $r_o = 30$ nm. Figure 4.18 shows the electron density as a function of the radial distance for a GaAs magnetic quantum dot without an overshoot, containing three interacting electrons. The solid curve in the figure shows results for the unstable system with $r_o = 30$ nm, while the dashed curve shows results for the stable system with $r_o = 50$ nm. From the figure it is seen that the electron density for the system with $r_o = 30$ nm has a better defined peak than the electron density for the system with $r_o = 50$ nm. The figure also shows that for the system with $r_o = 30$ nm, the electrons are localised more strongly towards the centre of the magnetic quantum dot, and therefore it is expected that the Coulomb energy of this system would be greater than the Coulomb energy of the system with $r_o = 50$ nm. Indeed, this is what is found. The Coulomb energy for the unstable system with $r_o = 30$ nm is found to be 3.40 meV, while the Coulomb energy of the stable system with $r_o = 50$ nm is 2.60 meV. Calculations also show that the single electron energy of the system with $r_o = 30$ nm is greater than that of the system with $r_o = 50$ nm. Therefore the

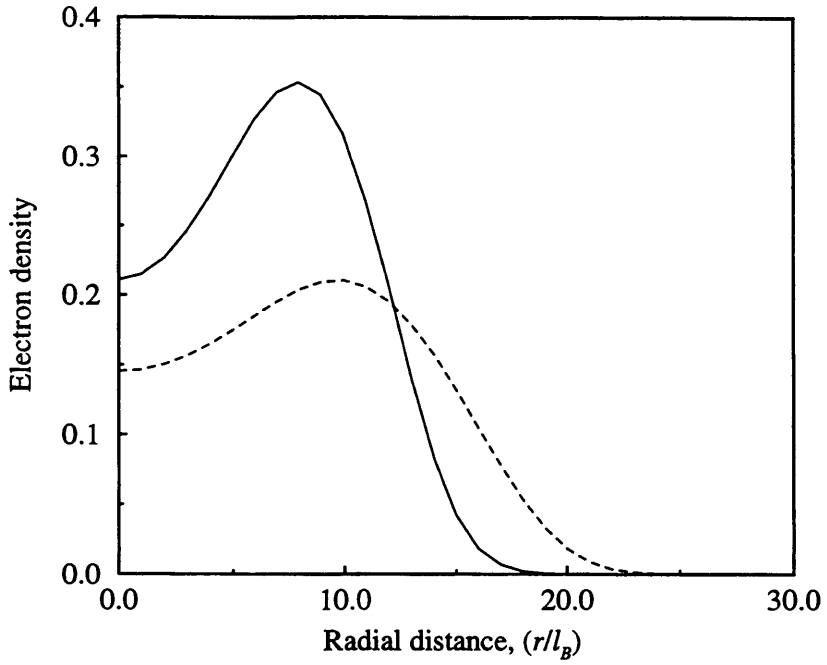

Figure 4.18: Electron density as a function of the radial distance for a GaAs magnetic quantum dot without overshoot containing three interacting electrons. The solid curve indicates the results obtained for an unstable system with $B_z = 10$ T and $r_o = 30$ nm, and the dashed curve indicates the results obtained for a stable system with $B_z = 10$ T and $r_o = 50$ nm.

system with $r_o = 30$ nm is less stable than the system with $r_o = 50$ nm because the total energy of the system is greater. Further interesting aspects of the three electron system can be seen by comparing the figure with the electron density of a magnetic quantum dot containing two electrons. Comparing figure 4.18 with figure 4.7 it is immediately seen that the spatial extent of the electron density function for the three electron system is greater than that of the two electron system. The electron density of the two electron system has a peak at roughly $r/l_B = 2$, while the electron density of the three electron system peaks at roughly $r/l_B = 10$. In the three electron system it is expected that the Coulomb force would be larger than in the two electron system, hence the Coulomb energy of

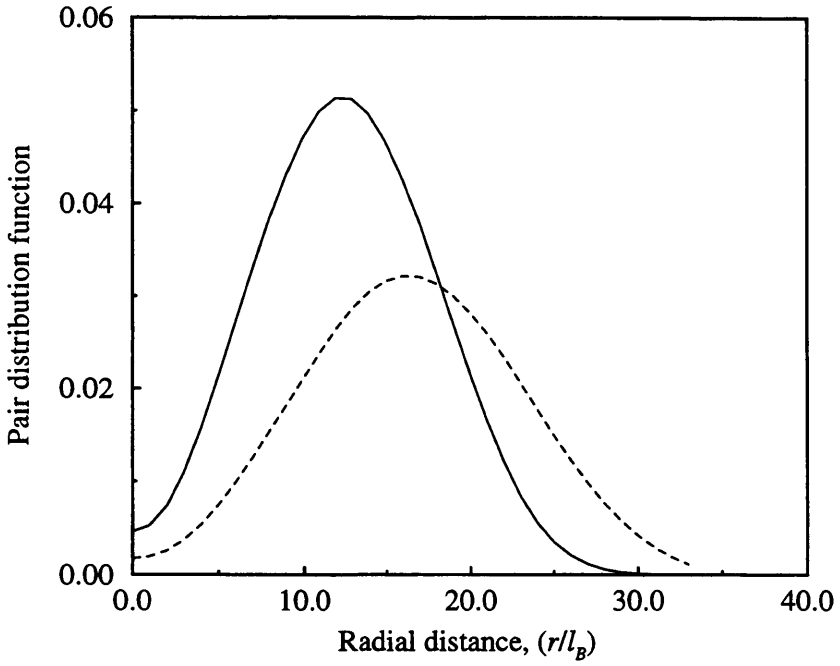

Figure 4.19: Pair distribution function as a function of the radial distance for a GaAs magnetic quantum dot without overshoot containing three interacting electrons. The solid curve indicates the results obtained for an unstable system with $B_z = 10$ T and $r_o = 30$ nm, and the dashed curve indicates the results obtained for a stable system with $B_z = 10$ T and $r_o = 50$ nm.

the three electron system is also larger. To reduce this the electrons maximise their separation. Therefore the spatial extent of the three electron wave function is greater than that of the two electron system.

The pair distribution function as a function of the radial distance for a GaAs system without an overshoot containing three interacting electrons is shown in figure 4.19. Again, the results are calculated for an unstable system with $B_z = 10$ T and $r_o = 30$ nm, and a stable system with $B_z = 10$ T and $r_o = 50$ nm. The solid curve in the figure indicates the results obtained for a system with $r_o = 30$ nm, while the dashed curve indicates the results obtained for the system with $r_o = 50$ nm. The figure shows that for the system with $r_o = 50$ nm, the

average interelectron separation is greater than for the system with $r_o = 30$ nm. This is expected and is due to the larger magnetic quantum dot radius in this system. Because the radius is greater, the electrons can increase their separation to a distance greater than that of the system with $r_o = 30$ nm, and, of course, because of this the Coulomb energy of the system with $r_o = 50$ nm is less. This is consistent with the decrease in the calculated Coulomb energy for the stable and unstable systems.

The pair correlation function for a GaAs system without an overshoot containing three interacting electrons is shown in figure 4.20. The top frame shows the pair correlation function for the unstable system with $B_z = 10$ T and $r_o = 30$ nm, and the bottom frame shows the pair correlation function for the stable system with $B_z = 10$ T and $r_o = 50$ nm. The axes for the pair correlation plots are graduated in steps of length $l_B/3$, with the origin at the centre of each plot. The black spots indicate the position of the fixed electron, $\mathbf{r}'$. The position, $\mathbf{r}'$, of the fixed electron is chosen to be the position of the maximum value of the electron density. Immediately it is seen from the figure that the pair correlation function for the system with $r_o = 30$ nm has a much more compact, sharp structure compared to that for the system with $r_o = 50$ nm. Again, this is what is expected, and is due to the greater magnetic quantum dot radius in the $r_o = 50$ nm system. This allows the three electron wave function to have a greater spatial extent and this is clearly seen in the figure. It is also interesting to observe the form of the electron configuration for the three electron system. Both the frames clearly show that the pair correlation function has well defined peaks, and that the electron configuration for the three electron system is roughly an equilateral triangle. This is expected, and the electrons are arranged

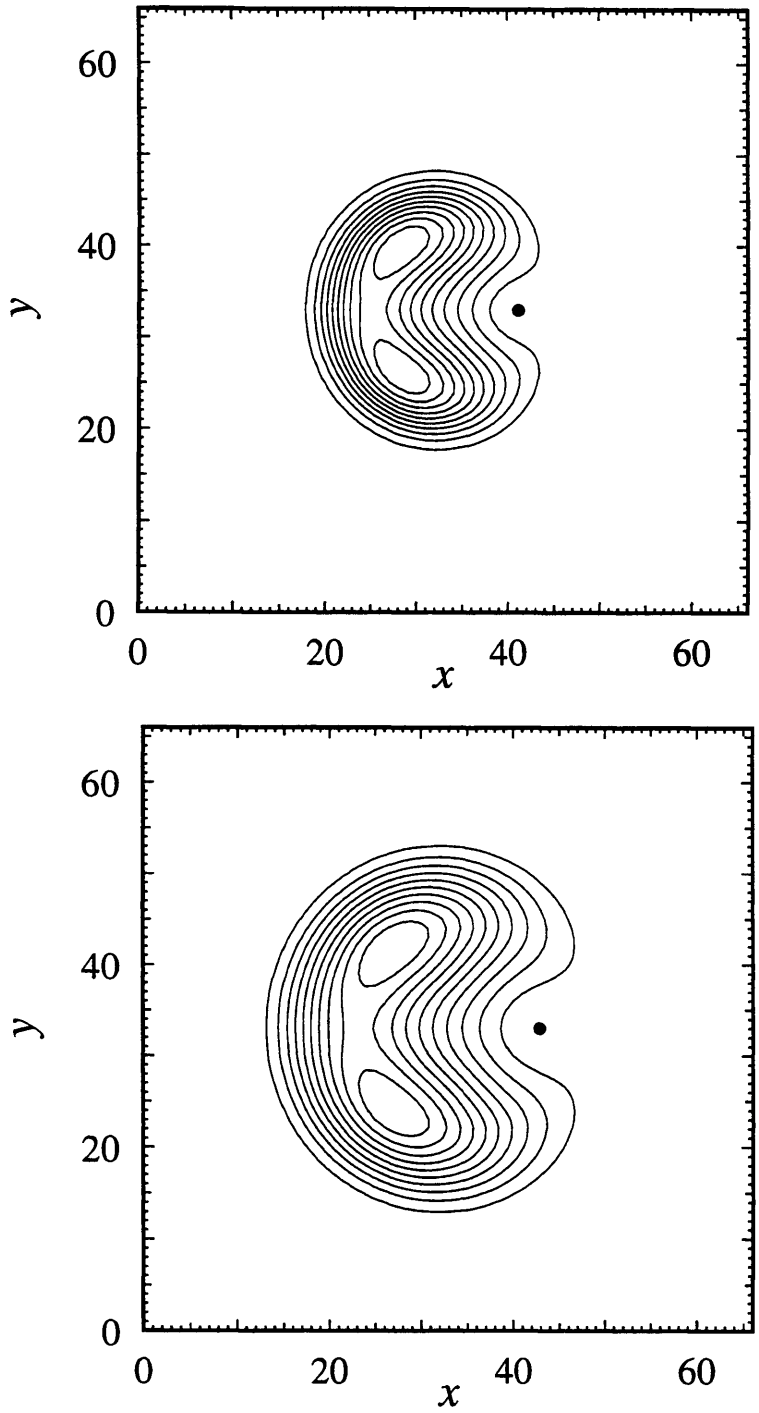

Figure 4.20: Pair correlation function for a GaAs magnetic quantum dot with overshoot containing three interacting electrons. The top frame shows the pair correlation function for an unstable system with $B_z = 10$ T and $r_o = 30$ nm, and the bottom frame shows the pair correlation function for a stable system with $B_z = 10$ T and $r_o = 50$ nm.

in this way to minimise the Coulomb energy of the system. In contrast, the Coulomb energy of the two electron system is minimised by the electrons being diametrically opposite.

Chapter 5

Far Infrared Absorption Spectra

In this chapter the far infrared (FIR) optical absorption spectra of a magnetic quantum dot containing up to two interacting electrons are investigated. FIR spectroscopy is one of many experimental techniques that are used to determine information about the electronic and optical properties of nanostructure devices. This technique is applicable to a wide range of low dimensional systems, including quantum dots, quantum wires and quantum wells.

This chapter is organised as follows. First, a brief overview of other work in this field is given and the generalised Kohn's theorem is discussed. In the following section the theoretical background required to perform an optical absorption calculation is given, and the optical matrix elements are calculated. Consequently the selection rules are determined. The FIR response as a function of the confining magnetic field is calculated for a GaAs and InSb magnetic quantum dot, containing one and two electrons. The FIR response as a function of an external homogeneous magnetic field is also calculated, and contrasts are made between the results for the FIR response as a function of the confining magnetic field. It is hoped that the results presented here will provide the motivation for experimental groups to fabricate and investigate this system.

5.1 Previous Work

FIR spectroscopy has been used to study the optical properties of electrostatic quantum dots. For example, Sikorski and Merkt [48] used FIR spectroscopy to investigate the electronic properties of an array of InSb quantum dots. Arrays of roughly 10^8 quantum dots were prepared on InSb surfaces with typical areas of 9 mm^2. They controlled the number of electrons in the quantum dots by adjusting the applied gate voltage. They found, that within experimental error, the FIR spectrum is independent of the number of electrons in the device, and therefore the experiments are insensitive to electron-electron interactions. These findings were also reported by Brey *et al* [45]. These authors studied the optical absorption of a parabolic GaAs quantum well theoretically and found that the absorption spectrum is independent of the electron-electron interaction, and also independent of the number of electrons in the quantum well.

Demel *et al* [49] used FIR spectroscopy to investigate the response of an array of GaAs quantum dot structures containing between 210 and 25 electrons per dot. Their results show that the FIR response consists of a set of resonances which split, in a magnetic field, into upper and lower branches. Further, they found that the upper branch of the FIR spectra exhibits anticrossing behaviour at low magnetic fields. Similar results were also obtained by Liu *et al* [50]. These authors investigated, theoretically and experimentally, the allowed optical transitions of a quantum dot in a magnetic field. They modelled the quantum dot theoretically assuming a parabolic confining potential. Using this model these authors predicted two transition energies as a function of the magnetic field (upper branch and lower branch) for the allowed optical transitions. They verified their theoretical predictions by experimentally obtaining the magnetotransmission

spectra of the system, and found that the experimental results agreed with the theoretical predictions for the energies of the upper branch.

There has been much debate as to the cause of the anticrossing reported by Demel *et al* [49]. These authors attribute this effect to plasma excitations in the system, while Chakraborty *et al* [51] suggested that a similar behaviour may result from the Coulomb interaction between neighbouring quantum dots. An alternative interpretation was given by Pfannkuche and Gerhardts [52]. They proposed that the anticrossing effect is due to deviations from a perfectly parabolic confining potential, therefore resulting in otherwise forbidden transitions. In the paper by Jacak *et al* [53] a theory is presented that describes a quantum dot that contains many electrons. In addition to the usual factors taken into account when describing a quantum dot, these authors included the spin-orbit interaction in their calculations. For a given fitting parameter, their results show that the FIR resonance energies obtained using their model agree well with the results reported by Demel *et al* [49]. To confirm the validity of their theory, Jacak *et al* [53] made a number of predictions, and predicted the critical magnetic field at which the anticrossing occurs and the resonance energy at the point of this anticrossing. It should be noted that the work performed by Jacak *et al* [53] has yet to be fully accepted by their peers, and the issue of what causes this anticrossing behaviour remains an open question.

The experiments performed by Sikorski and Merkt [48], Demel *et al* [49] and Liu *et al* [50] showed for the first time that in FIR spectroscopy measurements on quantum dot structures, the measured absorption energy is independent of the number of electrons in the device. In essence this is the generalised Kohn theorem [54] and this is discussed more thoroughly in the following section.

5.2 The Generalised Kohn Theorem

The consequence of the finding that the measured absorption energy is independent of the number of electrons, is that electron-electron interactions in the quantum dot do not influence the FIR spectra. Therefore, FIR spectroscopy cannot be used to probe electron-electron interaction effects in this system. These experimental results demonstrate a variation of Kohn's theorem [54]. Explicitly the theorem states that in a 2DEG, the cyclotron resonance is unaffected by electron-electron interactions.

The pioneering work of Maksym and Chakraborty [14] showed for the first time that Kohn's theorem could be applied to a system with parabolic confinement. These authors found that when the confining potential is quadratic in form, the centre of mass and relative motions of the electrons separate in the same way as for free electrons. Therefore the hamiltonian can be written as

$$H = \frac{1}{2M}(\mathbf{P} + Q\mathbf{A})^2 + \frac{1}{2}M\omega_o^2 R^2 + H_{\text{rel}}, \tag{5.1}$$

where $\mathbf{P} = \sum_i^N \mathbf{p}_i$ is the total electron momentum, $\mathbf{R} = \sum_i \mathbf{r}_i/N$ is the centre of mass coordinate and $M = Nm^*$ is the total electron mass, and $Q = Ne$ is the total electron charge. The last term in this equation is a function of only the relative coordinates, and contains all the effects of the electron-electron interaction. These authors considered the perturbation due to the electromagnetic radiation within the dipole approximation. This approximation is valid because of the relatively large wavelength of the incident far infrared radiation, compared with the size of a typical quantum dot. Far infrared radiation typically has a wavelength of 50 μm, while the size of a quantum dot is typically 100 nm, therefore the spatial variation of the incident radiation can be neglected, and the electric field, $\mathbf{E}_o$,

is independent of position within the quantum dot. The perturbing hamiltonian therefore has the form

$$H' = e\sum_{i}^{N} \mathbf{E}_o \cdot \mathbf{r}_i \exp(-i\omega t) = Q\mathbf{E}_o \cdot \mathbf{R}\exp(-i\omega t). \tag{5.2}$$

From this equation it is seen that the perturbing hamiltonian is expressed solely in terms of the centre of mass coordinates. Therefore the FIR radiation couples only to the centre of mass motion and does not affect the relative motion of the electrons, hence leading to an excitation spectrum that is identical to that of a single electron.

In other theoretical papers, several authors have considered electrostatic quantum dots with a non-parabolic confining potential [33, 35]. Pfannkuche *et al* [33] investigated the FIR response of an electrostatic quantum dot containing two interacting electrons. These authors considered deviations from the parabolic confining potential, and showed that the centre of mass and relative motions of the electrons no longer decouple. As a consequence, the generalised Kohn theorem no longer holds and Pfannkuche *et al* [33] found new resonances in the FIR spectra. Bruce and Maksym [35] investigated the FIR response of a realistic three dimensional electrostatic quantum dot containing three interacting electrons. The confining potential in the device was calculated numerically. These authors found that Kohn's theorem is violated, not only as a consequence of the non-parabolicity of the confining potential, but also as a consequence of the motion of the electrons in the third dimension.

Imamura *et al* [55] studied the ground state and excited state properties of vertically coupled quantum dots in a magnetic field. These authors assume that the confining potential of the quantum dots is parabolic in form. The generalised Kohn theorem does not hold for two vertically coupled quantum dots with

different confining potentials even when they are both parabolic. Consequently Imamura *et al* [55] found a one-to-one correspondence between the magnetic field at which the absorption line jumps and the magnetic field at which the total angular momentum quantum number and/or the total spin of the ground state changes from one "magic" number state to another. Imamura *et al* [55] predict that these jumps are of the order of tenths of meV, and should be experimentally observable.

Reijniers *et al* [10] have calculated the optical absorption spectrum of a magnetic quantum dot containing a single electron. From their analysis, they found that the selection rule for the radial quantum number is not the same as for an electrostatic quantum dot with parabolic confinement. Consequently, their results show that the absorption spectrum consists of many additional transitions. These authors attribute these transitions to a violation of Kohn's theorem, due to a coupling of the centre of mass motion and other degrees of freedom. However, their interpretation of the results is questionable. For the single electron system the centre of mass motion is the same as the position of the electron, and therefore there are no other degrees of freedom to couple to!

5.3 Theoretical Treatment

In this section the theoretical background needed to perform a many electron optical absorption calculation is given. First, the single electron case is dealt with, then this is generalised to calculate the many electron optical absorption. In order to calculate the transition probabilities, the dipole approximation is used.

To calculate the single electron dipole matrix elements, it is assumed that the incident radiation is circularly polarised. The single electron functions are chosen

to be the Fock-Darwin states, and these are given by Eq. 2.13. Within this framework, the transition probability of a single electron being excited from an initial single electron state ψ_{nl} to a final single electron state $\psi_{n'l'}$, is proportional to $|d_{nl,n'l'}|^2$ [56, 57], where

$$d_{nl,n'l'} = \langle \psi_{nl} | r e^{\pm i\phi} | \psi_{n'l'} \rangle \tag{5.3}$$

is the dipole matrix element, and ψ_{nl} has the form given by Eq. 2.13. Substituting the explicit form for the Fock-Darwin states into Eq. 5.3, the single electron dipole matrix element becomes

$$\begin{aligned} d_{nl,n'l'} &= N_{nl} N_{n'l'} \int_0^{2\pi} \int_0^{\infty} e^{-r^2/2l_B^2} \left(\frac{r^2}{2l_B^2}\right)^{\frac{|l|+|l'|}{2}} \\ &\times L_n^{|l|}\left(\frac{r^2}{2l_b^2}\right) L_{n'}^{|l'|}\left(\frac{r^2}{2l_b^2}\right) r^2 e^{i\phi(l-l')} e^{\pm i\phi} dr d\phi. \end{aligned} \tag{5.4}$$

Performing the integral over ϕ gives $2\pi\delta_{l-l',\pm 1}$. As a consequence of the Kronecker delta, $\delta_{l-l',\pm 1}$, the angular momentum quantum number for the initial and final states can only differ by one, thus leading to the selection rule $\Delta l = l' - l = \pm 1$. To evaluate the integral over r, the substitution $x = r^2/2l_B^2$ is made, giving

$$d_{nl,n'l'} = (\sqrt{2} l_B)^3 \pi N_{nl} N_{n'l'} \int_0^{\infty} e^{-x} x^{(|l|+|l'|+1)/2} L_n^{|l|}(x) L_{n'}^{|l'|}(x) dx. \tag{5.5}$$

This integral is evaluated using standard methods [58] and different results are obtained depending on whether $l' = l+1$, $l' = l-1$, $l > 0$, $l < 0$ and $l = 0$. It is found that for $l = 0$

$$d_{n0,n'\pm 1} = \sqrt{2} l_B \left[\sqrt{(n+1)}\delta_{n',n} - \sqrt{n}\delta_{n',n-1}\right], \tag{5.6}$$

for $l' = l + 1$

$$d_{nl,n'l+1} = \begin{cases} \sqrt{2} l_B \left[\sqrt{(n+|l|+1)}\delta_{n',n} - \sqrt{n}\delta_{n',n-1}\right] & \text{for } l > 0, \\ \sqrt{2} l_B \left[\sqrt{(n+|l|)}\delta_{n',n} - \sqrt{n+1}\delta_{n',n+1}\right] & \text{for } l < 0, \end{cases} \tag{5.7}$$

and for $l' = l - 1$

$$d_{nl,n'l-1} = \begin{cases} \sqrt{2}l_B \left[\sqrt{(n+|l|)}\delta_{n',n} - \sqrt{n+1}\delta_{n',n+1}\right] & \text{for } l > 0, \\ \sqrt{2}l_B \left[\sqrt{(n+|l|+1)}\delta_{n',n} - \sqrt{n}\delta_{n',n-1}\right] & \text{for } l < 0. \end{cases} \tag{5.8}$$

These equations are the single electron dipole matrix elements. The calculation of the single electron dipole matrix element has been performed previously and similar equations to these are given in the literature [36].

To calculate the optical absorption intensities of the many electron system, Eq. 5.3 is written in second quantised form, thus

$$D_{i,j} = \sum_{i,j} d_{i,j} c_i^\dagger c_j, \tag{5.9}$$

where $c_i^\dagger$ and c_j are the usual creation and destruction operators, i and j are single electron states, and $d_{i,j}$ is a single electron dipole matrix element given by Eq. 5.6, Eq. 5.7 or Eq. 5.8 depending on l and l'. To calculate the many electron absorption spectra, matrix elements of $D_{i,j}$ are taken between the numerically calculated ground state and all the excited states. Therefore all possible transitions out of the ground state are considered.

5.4 FIR Response as a Function of the Confining Magnetic Field

In this section results are presented showing the FIR response of various magnetic quantum dot systems. First, results showing the FIR response as a function of the confining magnetic field, B_z, are presented. It is shown that the FIR spectrum of a GaAs and an InSb system containing two interacting electrons is markedly different from that of the equivalent system containing one electron. Subsequently this difference is shown to be a direct consequence of the electron-electron interaction in the two electron system.

5.4.1 FIR Response of a GaAs Magnetic Quantum Dot

The top frame of figure 5.1 shows the FIR spectra of a GaAs magnetic quantum dot containing one electron. Eleven Landau levels are included in the numerical diagonalisation calculation to obtain energies that are accurate to approximately 0.001%. The frame shows the transition energies and calculated absorption intensities as a function of the confining magnetic field for a magnetic quantum dot radius of $r_o = 40$ nm. The ground state quantum numbers for this particular system are $l = 0$ and $S = 1/2$ throughout the confining magnetic field range. The results shown by the upper branch in the frame are the energies of the $\Delta l = -1$ transition, and the results shown by the lower branch are the energies of the $\Delta l = 1$ transition. The diameters of the filled circles are proportional to the calculated absorption intensities. It is seen that the calculated absorption intensities of the upper and lower branch are very similar, and no discernible difference is predicted throughout the confining magnetic field range. Additionally, it is seen that the transition energy of the upper branch for B_z=6 T is roughly 1.75 meV, while the equivalent transition energy of the lower branch is approximately 1.25 meV. As the confining magnetic field increases, the energy difference between the $\Delta l = -1$ transition and the $\Delta l = 1$ transition decreases. This is expected, and is because in the large confining magnetic field regime $l_B \ll r_o$, most of the electron wave function is localised inside the magnetic quantum dot. The energies of the system in this large field regime are then similar to those of the single electron in a circular dot in the absence of a magnetic field, and these are determined by the zeros of the Bessel function, $J_{|l|}(kr)$ [10].

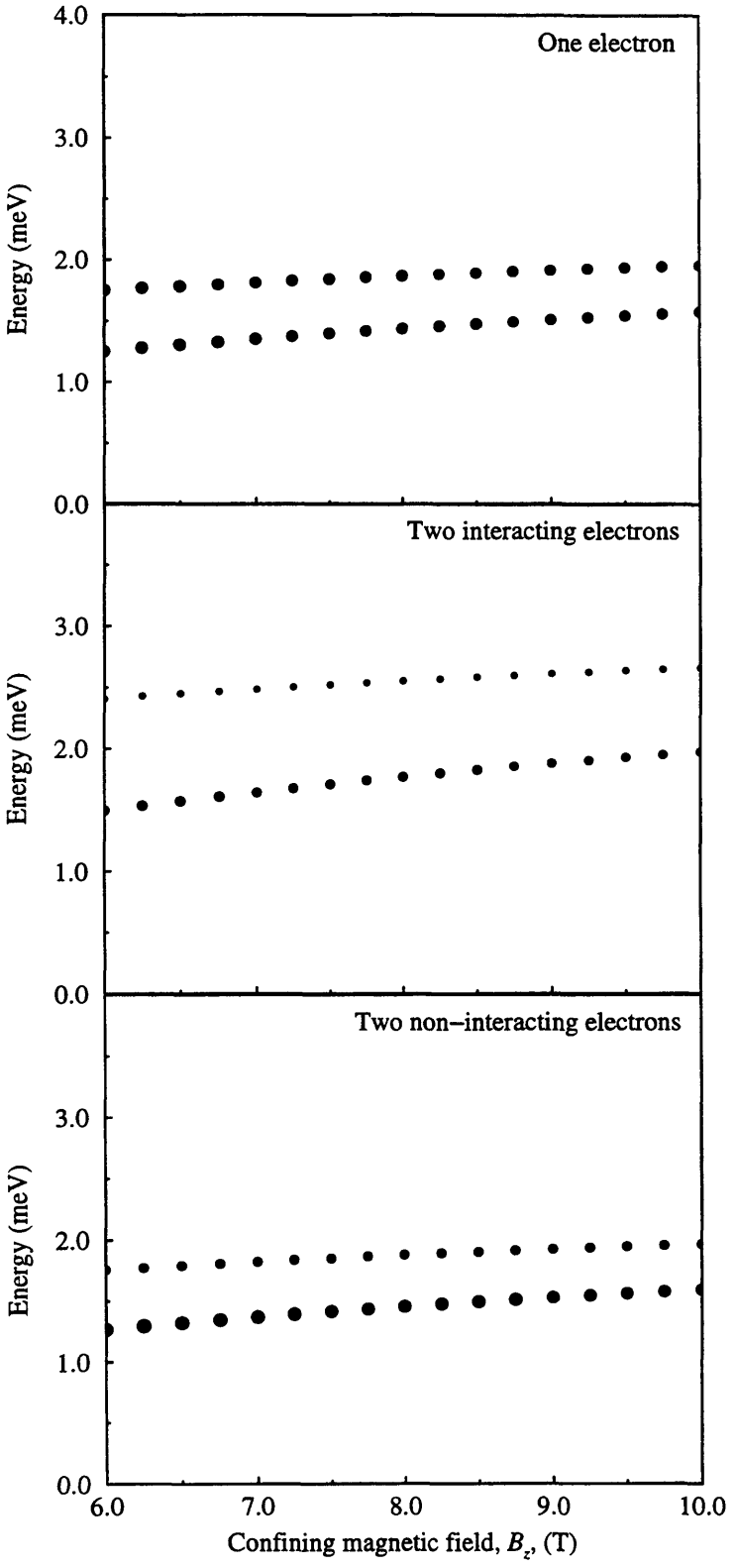

Figure 5.1: Dipole allowed optical absorption energies and intensities of a GaAs magnetic quantum dot with r_o = 40 nm. The diameters of the filled circles are proportional to the calculated absorption intensities.

In the centre frame of figure 5.1 the transition energies and calculated absorption intensities of a GaAs magnetic quantum dot containing two interacting electrons, as a function of the confining magnetic field are presented. Eleven Landau levels are included in the numerical diagonalisation calculation to obtain energies that are accurate to roughly 0.5%, and the results are calculated for a system with a magnetic quantum dot radius of $r_o = 40$ nm. Because this is a two electron system, the ground state quantum numbers do not necessarily coincide with those of the one electron system. Therefore for each confining magnetic field value at which the FIR response of the system is calculated, the ground state quantum numbers are determined. The system is found to be stable for all the values of the confining magnetic field for which the FIR response has been calculated, and the ground state quantum numbers are $J = 0$ and $S = 0$. The results shown by the upper branch in the frame are the energies of the $\Delta J = -1$ transition, and the results shown by the lower branch are the energies of the $\Delta J = 1$ transition. The diameters of the filled circles are proportional to the calculated absorption intensities. It is seen that the transition energies of the upper and lower branches are dissimilar to those shown in the upper frame of the figure. The transition energy of the upper branch for B_z=6 T is now roughly 2.5 meV, while the equivalent transition energy of the lower branch is roughly 1.5 meV. Also it is seen that the calculated absorption intensities for the upper branch are less than those for the lower branch. The fact that the two electron FIR spectra is not identical to the one electron FIR spectra suggests that Kohn's theorem is violated in the case of the magnetic quantum dot, and this has already been reported by Reijniers *et al* [10]. This result is not unexpected, and is due to coupling of the centre of mass and relative motion of the electrons in this system.

Unlike the FIR response of an electrostatic quantum dot, the FIR response of magnetic quantum dot containing two interacting electrons is markedly different to that of the equivalent one electron system. This, in principle, allows electron-electron interaction effects to be probed in a magnetic quantum dot. To be certain that this difference is caused by the electron-electron interaction in the two electron system, additional calculations are performed. By intentionally setting the dielectric constant, ϵ, to a large number, the effect of the electron-electron interaction on the FIR response of the system should become less.

The bottom frame of figure 5.1 shows the transition energies and calculated absorption intensities for a GaAs magnetic quantum dot containing two interacting electrons. The results are calculated for a system with a magnetic quantum dot radius of $r_o = 40$ nm, and the ground state quantum numbers are found to be $J = 0$ and $S = 0$ for all values of the confining magnetic field. The results shown by the upper branch and lower branch in the frame are the energies of the $\Delta J = -1$ and $\Delta J = 1$ transition respectively. The diameters of the filled circles are proportional to the calculated absorption intensities. The only difference between the results shown in this frame and the results shown in the centre frame of the figure is that the dielectric constant, $\epsilon = 10000$. It is seen that the FIR response of this system is very similar to that calculated for the one electron system (see the top frame of figure 5.1). The transition energy of the upper branch at $B_z = 6$ T is roughly 1.25 meV, and the equivalent transition energy of the lower branch is roughly 1.75 meV. Additionally, it is seen that the calculated absorption intensities for the upper branch are less than those for the lower branch. This is probably a result of the small, but nevertheless finite effect of the electron-electron interaction in this system.

5.4.2 FIR Response of an InSb Magnetic Quantum Dot

The upper frame of figure 5.2 shows the transition energies and the calculated absorption intensities of an InSb magnetic quantum dot containing one electron. The results are obtained for a system with a magnetic quantum dot radius of $r_o =$ 40 nm, and eleven Landau levels are included in the numerical diagonalisation calculation to obtain results that are accurate to roughly 0.001%. The ground state quantum numbers for this system are found to be $l = 0$ and $S = 1/2$ throughout the confining magnetic field range. The results shown by the upper branch and lower branch in the frame are the energies of the $\Delta l = -1$ transition, and of the $\Delta l = 1$ transition respectively. The diameters of the filled circles are proportional to the calculated absorption intensities. It is seen that the form of the transition energies for both the upper and lower branch, are similar to those calculated for the equivalent GaAs system. However, it is noticed that the energy difference between the two branches is roughly 4 meV, in contrast to an energy difference of roughly 0.5 meV for the GaAs system. This is thought to be a result of the reduced effective mass in the InSb system.

The FIR response of the equivalent system containing two interacting electrons is shown in the lower frame of figure 5.2. Again, eleven Landau levels are included in the numerical diagonalisation calculation to obtain results that are accurate to roughly 0.7%. The system is found to be stable for all the values of the confining magnetic field at which the FIR optical absorption has been calculated. As in the previous two electron calculation, the ground state quantum numbers are determined for each confining magnetic field value, and they are found to be $J = 1$ and $S = 1$ for all values of the confining magnetic field. The results shown by the upper branches in the frame are the energies of the $\Delta J = -1$ transition, and

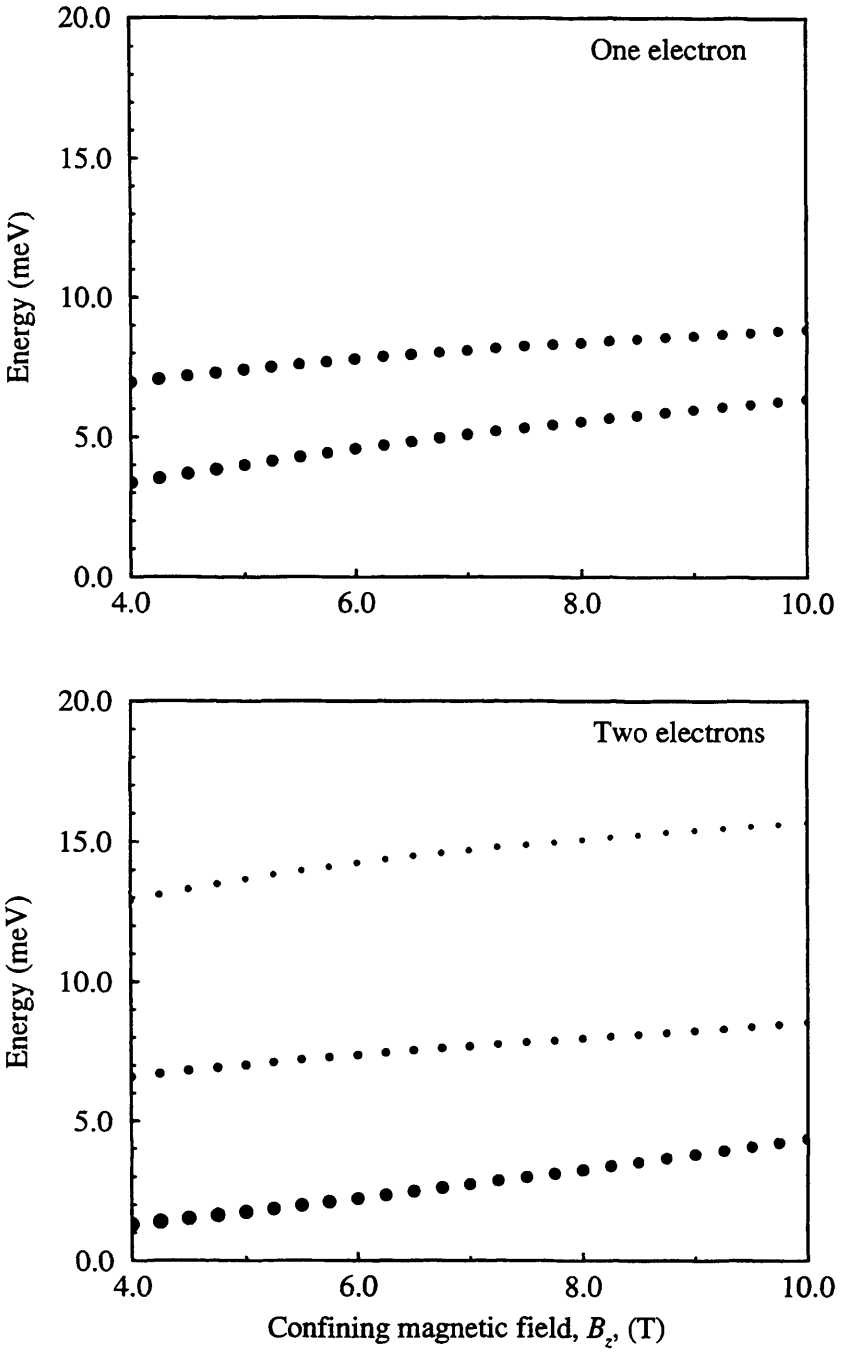

Figure 5.2: Dipole allowed optical absorption energies and intensities of an InSb magnetic quantum dot with r_o = 40 nm, containing one electron (upper frame), and two interacting electrons (lower frame). The diameters of the filled circles are proportional to the calculated absorption intensities.

the results shown by the lower branch are the energies of the $\Delta J = 1$ transition. The diameters of the filled circles are proportional to the calculated absorption intensities. It is noticed from the frame that there is a large splitting of the upper branch.

It is conjectured that this splitting is due to a combination of effects involving the ground state quantum numbers and the coupling of the centre of mass and relative motion of the electrons. Indeed, further calculations were performed during the course of this work to investigate the FIR response of a similar system to the previous, but with $r_o = 0.01$ nm. For such a small magnetic quantum dot radius the system effectively consists of electrons in an homogeneous magnetic field, and hence the centre of mass and relative motion of the electrons decouple. From the results it is found that there are two transitions from the $J = 1$ state to the $J = 0$ state, however, both transitions are found to have the same energy. To investigate these transitions further, an analysis of the quantum numbers of the initial and final states is undertaken. The centre of mass and relative motion of the electrons decouple, and therefore the centre of mass angular momentum quantum number, $J_{\rm CM}$, and the relative motion angular momentum quantum number, $J_{\rm RM}$, are good quantum numbers, and $J = J_{\rm CM} + J_{\rm RM}$. For this system, the ground state total angular momentum quantum number is $J = 1$, and because $J_{\rm CM} = 0$ for the ground state of the two electron system [59], $J_{\rm RM} = 1$. From the single electron dipole matrix element (Eq. 5.6), it is found that two transitions are permitted, one $\Delta J = -1$ transition resulting in the final state quantum numbers $J_{\rm CM} = -1$ and $J_{\rm RM} = 1$, and one $\Delta J = 1$ transition resulting in the final state quantum numbers $J_{\rm CM} = 1$ and $J_{\rm RM} = 1$. This, however, contradicts the obtained results, that show two distinct transitions for $\Delta J = -1$. To resolve this contradiction

it is noted that the state with $J_{\rm CM} = -1$ and $J_{\rm RM} = 1$ is degenerate with the state $J_{\rm CM} = 1$ and $J_{\rm RM} = -1$ (see Pfannkuche *et al* [33]). In the presence of an inhomogeneous magnetic field, it is conjectured that these states become coupled, and their degeneracy is lifted, thus explaining the splitting of the upper branch in the lower frame of figure 5.2.

Further calculations verify this hypothesis, and show a splitting of the upper branch that increases with the magnetic quantum dot radius. Figure 5.3 shows the FIR response of an Insb magnetic quantum dot containing two interacting electrons for various magnetic quantum dot radii. All the frames in the figure show the results of the $\Delta J = -1$ transition only, and the diameters of the filled circles are proportional to the calculated absorption intensities. The top frame of the figure shows results for a magnetic quantum dot with $r_o = 1$ nm, the centre frame shows results for a magnetic quantum dot with $r_o = 5$ nm, and the bottom frame shows results for a magnetic quantum dot with $r_o = 9$ nm. It is seen that as the radius of the magnetic quantum dot increases, the splitting of the branch correspondingly increases. For example, a system with $r_o = 1$ nm and $B_z = 4$ T has negligible splitting. As the radius of the magnetic quantum dot increases to $r_o = 5$ nm, the splitting is equal to roughly 2 meV, and for $r_o = 9$ nm the splitting increases to roughly 5 meV.

The reason why no splitting is observed in the case of the GaAs magnetic quantum dot containing two interacting electrons is because the ground state angular momentum of this system is $J = 0$. Again for explanatory purposes, the limit of small r_o is taken. In this regime the centre of mass and relative motion decouple, and therefore $J = J_{\rm CM} + J_{\rm RM}$. The ground state total angular momentum value for the GaAs system is $J = 0$, and hence $J_{\rm CM} = 0$ and $J_{\rm RM} = 0$.

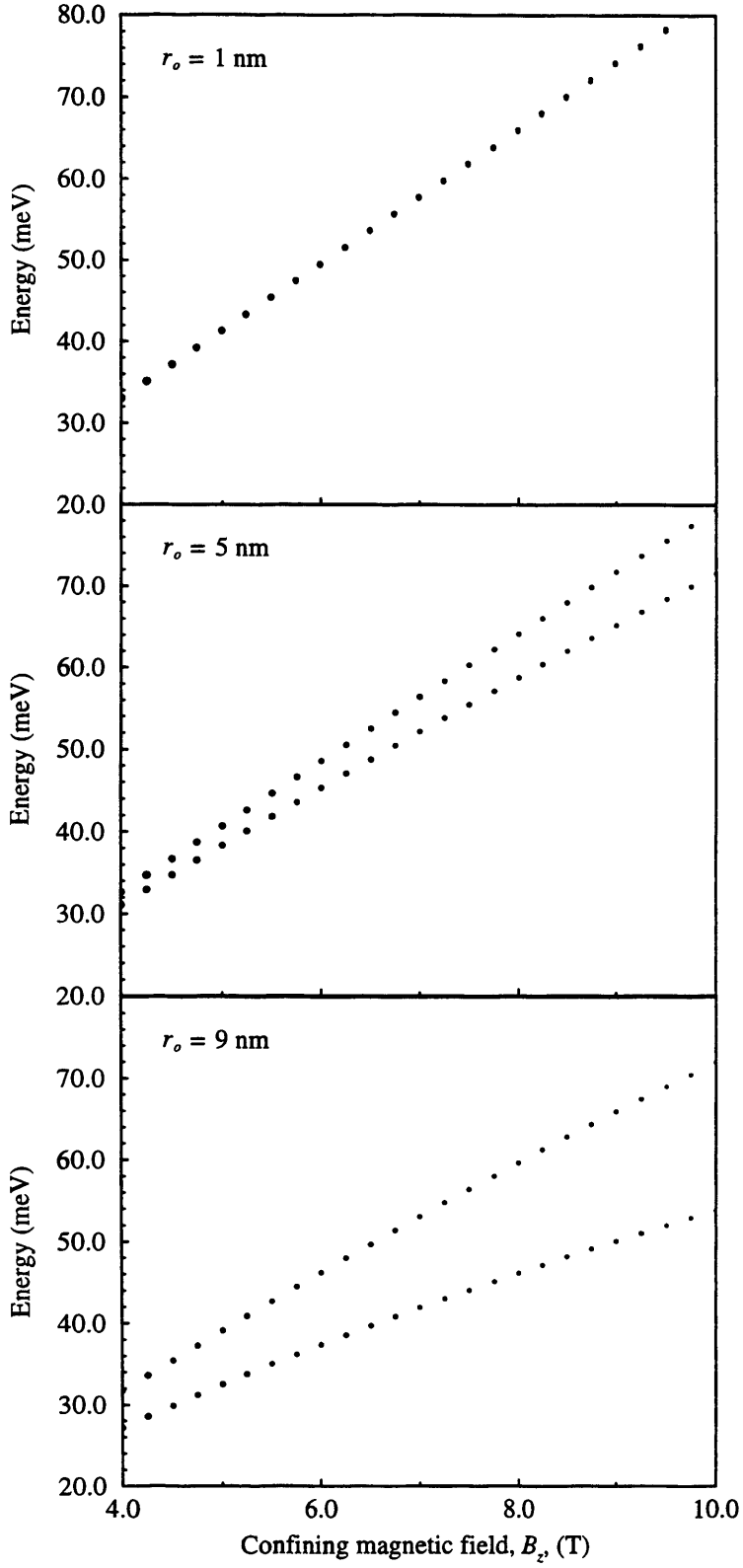

Figure 5.3: Dipole allowed optical absorption energies and intensities of an Insb magnetic quantum dot with various r_o. The diameters of the filled circles are proportional to the calculated absorption intensities.

From the single electron dipole matrix element (Eq. 5.6), it is found that two transitions are permitted, one $\Delta J = -1$ transition resulting in the final state quantum numbers $J_{\rm CM} = -1$ and $J_{\rm RM} = 0$, and one $\Delta J = 1$ transition resulting in the final state quantum numbers $J_{\rm CM} = 1$ and $J_{\rm RM} = 0$. Neither of these states are degenerate, and therefore no splitting is observed as the confining magnetic field increases and the centre of mass and relative motion become coupled.

5.5 FIR Response as a Function of an External Magnetic Field

In this section results are presented showing the FIR response of an InSb and a GaAs magnetic quantum dot containing one electron as a function of an applied external magnetic field, $B_{\rm ext}$. These results are shown to be similar to the FIR spectra of an electrostatic quantum dot with a parabolic confining potential. The FIR response of the equivalent two electron systems is calculated. These are shown to contain interesting structure that is absent from the single electron results, and explanations for these differences are given.

5.5.1 FIR Response of an InSb Magnetic Quantum Dot

The upper frame of figure 5.4 shows the FIR response of a magnetic quantum dot containing one electron as a function of a homogeneous external magnetic field. Eleven Landau levels are included in the numerical diagonalisation calculation to obtain energies that are accurate to approximately 0.001%. The frame shows the transition energies and calculated absorption intensities of an InSb magnetic quantum dot as a function of the external magnetic field for a magnetic quantum dot radius of $r_o = 100$ nm and a confining magnetic field of $B_z = 1$ T. The ground state quantum numbers for this particular system are

found to be $l = 0$ and $S = 1/2$ throughout the external magnetic field range. The results shown by the upper branch in the frame are the energies of the $\Delta l = -1$ transition, and the results shown by the lower branch are the energies of the $\Delta l = 1$ transition. The diameters of the filled circles are proportional to the calculated absorption intensities. It is seen that the form of the FIR spectrum as a function of the external magnetic field is very different from the form as a function of the confining magnetic field shown in section 5.4.1 and section 5.4.2. As the external magnetic field increases the transition energies of the lower branch in the frame tend to zero very rapidly, while the transition energies of the upper branch tend to a linear function of the external magnetic field. The reason is that for a large external magnetic field, the confining magnetic field is relatively small and therefore the system behaves essentially as a single electron in a homogeneous magnetic field. The energies of the system then tend to the energies of the Landau levels, and therefore the transition energies of the lower and upper branch tend to zero and $\hbar\omega_c$ respectively. For small values of the external magnetic field, the transition energies approach a value greater than zero. This is because in this regime the confining magnetic field is of the same magnitude as the external magnetic field, and hence the inhomogeneity of the confining magnetic field is noticeable and cannot be neglected. Additionally, it is seen that there is a non-zero splitting of the upper and lower branch at zero external magnetic field.

For comparison, the lower frame of figure 5.4 shows the transition energies and calculated absorption intensities of an electrostatic quantum dot containing one electron. The results are for a system with a confinement energy of $\hbar\omega_o = 1$ meV, and again the ground state quantum numbers are found to be $l = 0$ and $S = 1/2$ for all values of the magnetic field. The results shown by the upper branch in

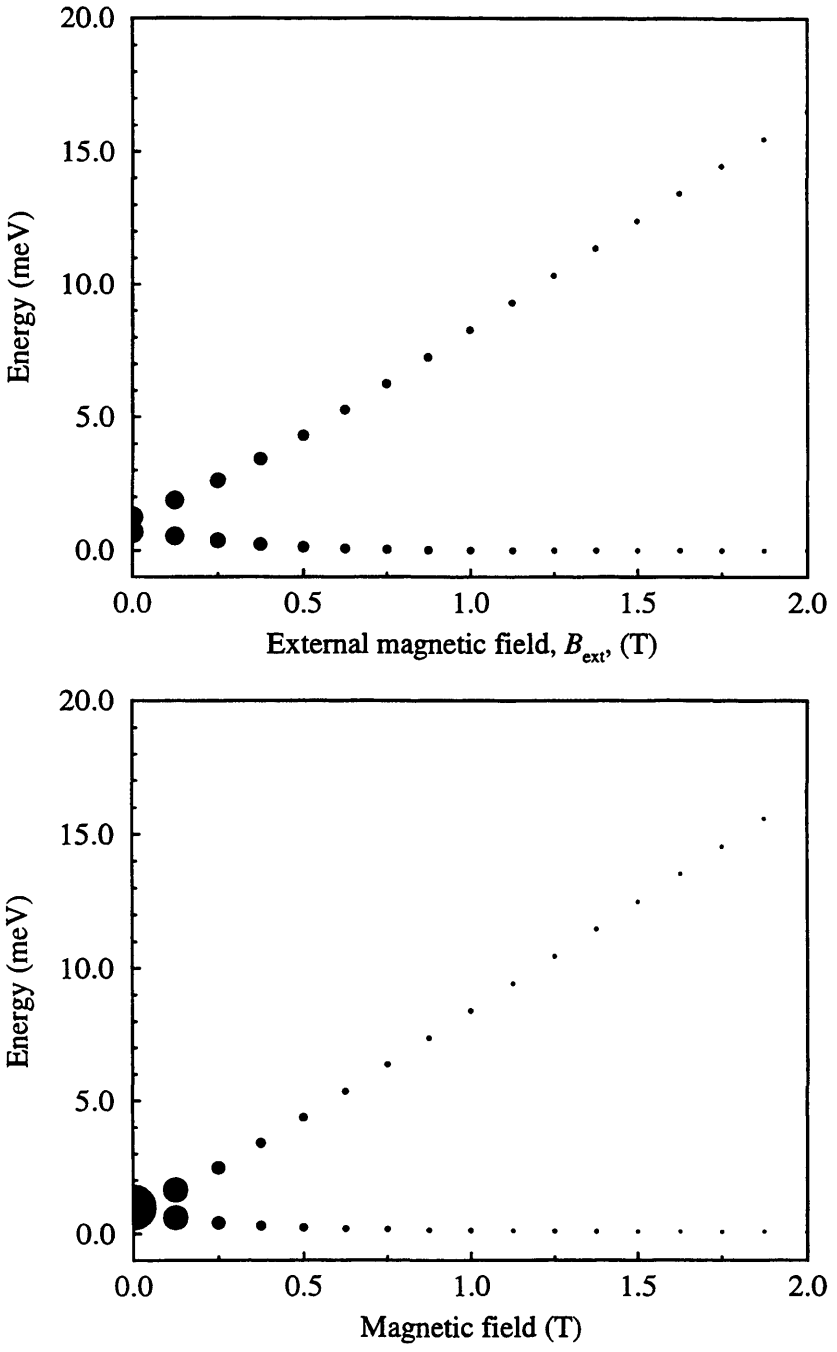

Figure 5.4: Dipole allowed optical absorption energies and intensities of an InSb magnetic quantum dot with $r_o = 100$ nm and $B_z = 1$ T (upper frame), and an electrostatic quantum dot with confining energy, $\hbar\omega_o = 1$ meV (lower frame), containing one electron. The diameters of the filled circles are proportional to the calculated absorption intensities.

the frame are the energies of the $\Delta J = -1$ transition, and the results shown by the lower branch are the energies of the $\Delta J = 1$ transition. The diameters of the filled circles are proportional to the calculated absorption intensities. The form of the FIR spectrum is very similar to that shown in the upper frame of the figure. The reason for this can be understood by investigating the form of the transition energies for an electrostatic quantum dot. The transition energies are given by $\Delta E_{\pm} = \hbar\Omega \pm \hbar\omega_c/2$ [36], where $\Omega^2 = \omega_o^2 + \omega_c^2/4$ and the $+(-)$ sign corresponds to left (right) circular polarisation. Because the confining energy, $\hbar\omega_o$, is small compared with the cyclotron energy, $\hbar\omega_c$, for much of the FIR spectrum (shown in the lower frame of figure 5.4), the approximation $\Omega = \omega_c/2$ can be made. Within this approximation the transition energies for the electrostatic quantum dot are $\Delta E_{\pm} = \hbar\omega_c/2 \pm \hbar\omega_c/2$, and therefore the transition energies of the lower and upper branch tend to zero and $\hbar\omega_c$ respectively as the magnetic field increases. These are the same transition energies as in the case of a magnetic quantum dot in an external magnetic field, and hence the two FIR spectra are very similar. In contrast to the FIR response of the magnetic quantum dot, it is seen that at zero external magnetic field the splitting of the upper and lower branch is zero.

Figure 5.5 (upper frame) shows the the FIR response of a magnetic quantum dot containing two interacting electrons as a function of an external magnetic field. Ten Landau levels are included in the numerical diagonalisation calculation to obtain energies that are accurate to approximately 1%. The frame shows the transition energies and calculated absorption intensities of an InSb magnetic quantum dot as a function of the external magnetic field for a magnetic quantum dot radius of $r_o = 100$ nm and a confining magnetic field of $B_z = 1$ T. This system is stable even in the absence of an homogeneous external magnetic field.

As in the previous two electron calculation, the ground state quantum numbers are determined for each magnetic field value, and it is found that the ground state angular momentum quantum number increases with the external magnetic field. The lower frame of the figure shows how the ground state total angular momentum quantum number changes with external magnetic field. The total spin quantum number is found to be $S = 1$ for all values of the external magnetic field. The results shown by the upper branch and lower branch in the upper frame of the figure are the energies of the $\Delta J = -1$ transition, and of the $\Delta J = 1$ transition respectively. The diameters of the filled circles are proportional to the calculated absorption intensities.

From the upper frame of the figure it is seen that the general form of the FIR spectrum is similar to that of the single electron FIR spectrum (shown in figure 5.4). Again, as the external magnetic field increases, the transition energies of the lower branch tend to zero, and the transition energies of the upper branch tend to the cyclotron energy. However, it is seen that there is interesting structure to the upper branch. There is a splitting of the upper branch, which generally decreases with increasing magnetic field. For a system with no external magnetic field, the magnetic field in the system is given by the inhomogeneous magnetic field inherent to the ferromagnetic material deposited upon the heterostructure. The reason for the splitting can then be understood by the argument given in section 5.4.2, and is due to a coupling between the centre of mass and relative motion states of the electrons. Due to this coupling the degeneracy of these states is lifted, resulting in the two distinct transition energies shown in the upper branch of the figure. As the external magnetic field increases, the effect of the inhomogeneity due to the inherent magnetic field associated with the

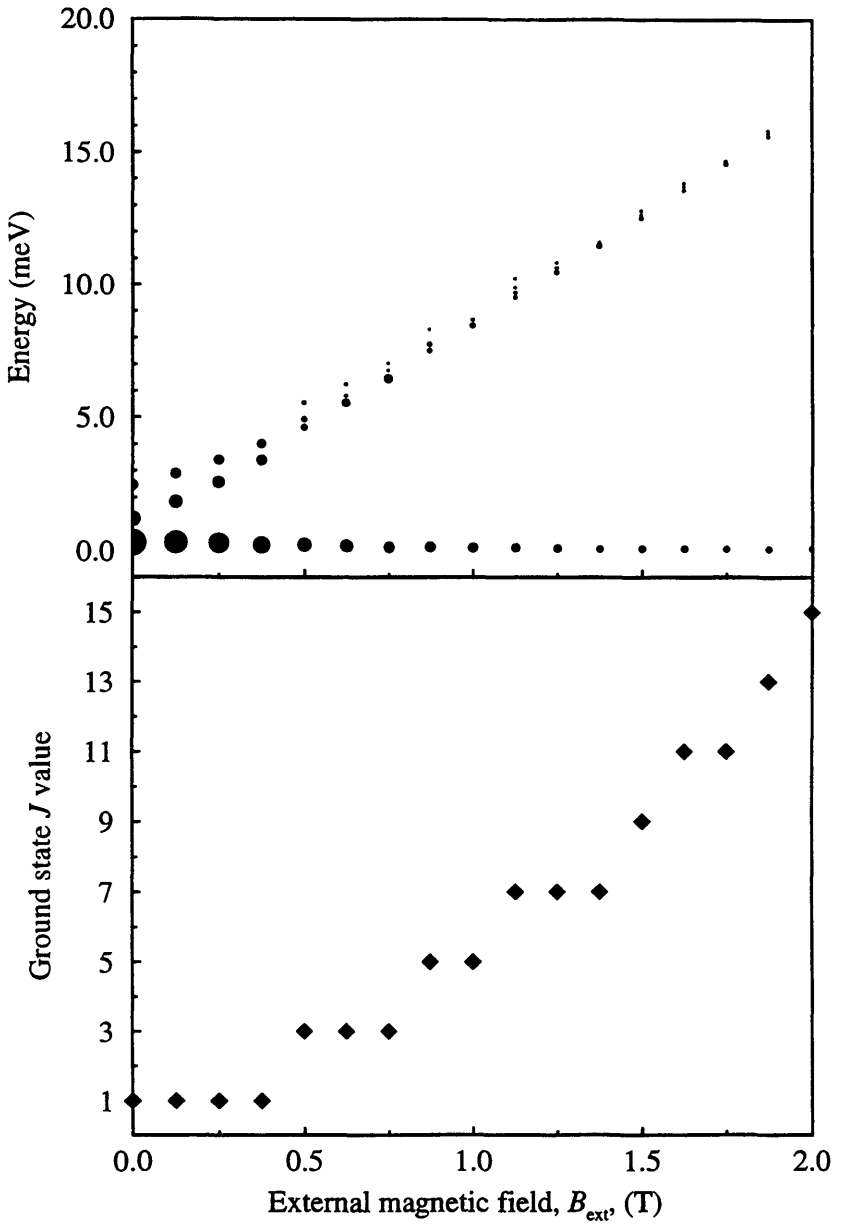

Figure 5.5: The upper frame shows the dipole allowed optical absorption energies and intensities of an InSb magnetic quantum dot with r_o = 100 nm and B_z = 1 T, containing two interacting electrons. The diameters of the filled circles are proportional to the calculated absorption intensities. The lower frame shows the ground state total angular momentum quantum number as a function of the external magnetic field

ferromagnetic material becomes less, and the coupling between the centre of mass and relative motion of the electrons becomes weaker, therefore resulting in a smaller splitting. The system is essentially two interacting electrons in a homogeneous magnetic field when the external magnetic field is large, and in this regime the centre of mass and relative motion of the electrons decouple, and therefore no splitting is observed.

Further interesting features of the FIR spectrum are noticed when viewed in conjunction with the lower frame of the figure. It is seen that there is a direct correlation between changes in the ground state total angular momentum quantum number and the structure of the splitting seen in the upper frame of the figure. For example, the ground state total angular momentum quantum number of a system with $B_{\text{ext}} = 0 - 0.375$ T is found to be $J = 1$. From the figure this corresponds to two strong transitions in the upper branch. As the external magnetic field increases ($B_{\text{ext}} = 0.5 - 0.75$ T), the ground state total angular momentum quantum number increases to $J = 3$, and the structure of the splitting changes. It is seen that, rather than two transitions in the upper branch (as is the case when $J = 1$) there are now three transitions. As the external magnetic field increases further, the correlations between the ground state total angular momentum quantum number and the structure of the splitting become less discernible. However, there do seem to be several oscillations from a doublet structure to a triplet structure in the upper branch.

5.5.2 FIR Response of a GaAs Magnetic Quantum Dot

The FIR response of a GaAs magnetic quantum dot containing two interacting electrons is shown in the upper frame of figure 5.6. Ten Landau levels are included

in the numerical diagonalisation calculation to obtain energies that are accurate to approximately 0.8%. The frame shows the transition energies and calculated absorption intensities of a GaAs magnetic quantum dot as a function of the external magnetic field for a magnetic quantum dot radius of $r_o = 50$ nm and a confining magnetic field of $B_z = 5$ T. The results shown by the upper branch and lower branch in the upper frame of the figure are the energies of the $\Delta J = -1$ transition, and of the $\Delta J = 1$ transition respectively. The diameters of the filled circles are proportional to the calculated absorption intensities. Again, because this is a two electron calculation the ground state quantum numbers are determined for each magnetic field value. It is found that the ground state angular momentum quantum number increases with the external magnetic field, and this is shown in the lower frame of the figure. In contrast to the InSb results (shown in figure 5.5), in which the total spin quantum number is $S = 1$ for all values of the external magnetic field, it is found that there is a total spin quantum number transition from $S = 0$ to $S = 1$ at roughly $B_{\text{ext}} = 0.3$ T. The inset in the upper frame of the figure shows the FIR response for $B_{\text{ext}} \leq 0.5$ T, and the consequence of this spin transition on the calculated results. It is seen that for $B_{\text{ext}} < 0.3$ T, the calculated absorption intensities are relatively small. For $B_{\text{ext}} \geq 0.3$ T there is a sudden increase in the calculated absorption intensity.

As with the InSb results (figure 5.5) it is seen that there is interesting structure to the upper branch. There is a splitting of the upper branch, which generally decreases with increasing magnetic field. An exception to this is the data calculated with $B_{\text{ext}} < 0.3$ T. In this regime no splitting of the upper branch is predicted, and the reason for this is given in latter part of section 5.4.2, and is due to the ground state of the system having quantum numbers $S = 0$ and $J = 0$.

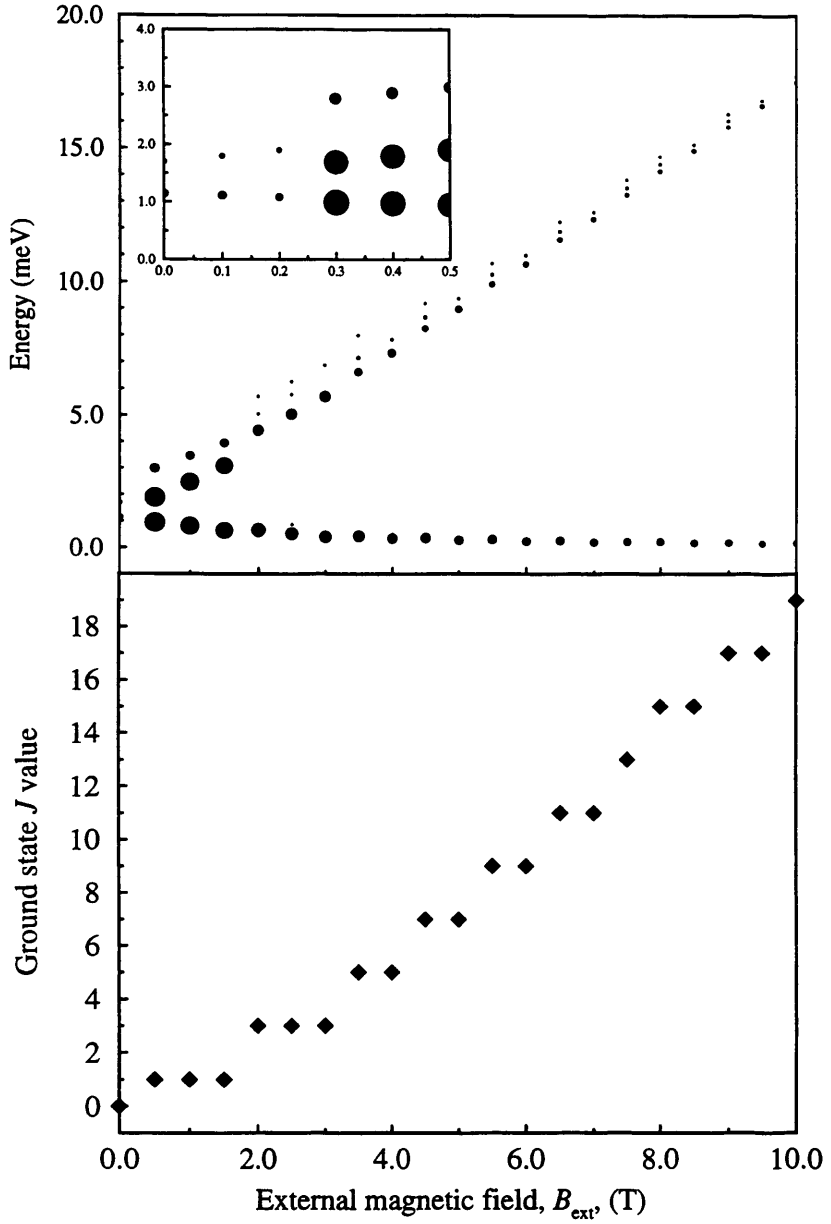

Figure 5.6: The upper frame shows the dipole allowed optical absorption energies and intensities of a GaAs magnetic quantum dot with r_o = 50 nm and B_z = 5 T, containing two interacting electrons. The diameters of the filled circles are proportional to the calculated absorption intensities. The inset shows the effect of the spin transition on the calculated data. The lower frame shows the ground state total angular momentum quantum number as a function of the external magnetic field

For the calculated data with $B_{\text{ext}} \geq 0.3$ T, the results show a similar trend to those calculated and presented in figure 5.5. The explanation of the splitting is given in the previous section, and is due to a coupling between centre of mass and relative motion states.

When viewed in conjunction with the lower frame of the figure, it is seen that a direct correlation exists between changes in the ground state total angular momentum quantum number and the structure of the splitting seen in the upper frame of the figure. For $B_{\text{ext}} = 0$ T, $J = 0$ and this corresponds to a weak transition in the upper branch. As B_{ext} increases upto 1.5 T, the ground state angular momentum of the system changes from $J = 0$ to $J = 1$. This corresponds to two strong transitions in the upper branch. As B_{ext} increases further, J also increases, and consequently subtle changes of the structure of the splitting are observed. Furthermore, observing the slopes of the upper and lower branches, it is just possible to see changes in the gradient of these branches that are correlated with the structural changes of the splitting.

5.6 Scope for Future Experiments

Many of the theoretical results presented in this chapter should be experimentally verifiable with near or existing technology. The single electron results calculated for the GaAs and InSb magnetic quantum dot as a function of the confining magnetic field should pose little or no problems to acquire experimentally. To obtain the relatively high confining magnetic fields used to obtain these results, it is suggested that the systems could be fabricated by depositing a superconducting material near to a 2DEG. The confining magnetic field is then the external magnetic field applied to the system, and these high

magnetic fields should be relatively easy to attain. The single electron results for the GaAs magnetic quantum dot as a function of the external magnetic field may prove more difficult to obtain. Because the confining magnetic field is constant, while the external magnetic field varies, the system must be fabricated by depositing a ferromagnetic material near to a 2DEG. The ferromagnetic material then provides the constant confining magnetic field. As discussed in chapter 4, a typical confining magnetic field produced by the ferromagnetic material is $B_z = 0.5$ T. For the results calculated and presented in the upper frame of figure 5.4 the confining magnetic field is $B_z = 1$ T, and this may just be out of reach with current experimental capabilities. However, it is thought that the results would not differ greatly with $B_z = 0.5$ T.

With the parameters used to obtain the two electron results for the GaAs magnetic quantum dot as a function of the confining magnetic field, the system should be able to be fabricated experimentally with existing technology. Again, to obtain the high confining magnetic fields it is suggested that the system is fabricated by depositing a superconducting material near to a 2DEG. For all the parameters used, the system is stable and therefore the magnetic quantum dot always confines the two interacting electrons. This is also the case for the results obtained for the equivalent InSb magnetic quantum dot. This is encouraging, because it should therefore be possible to verify experimentally the predicted large splitting of the upper branch shown in the lower frame in figure 5.2.

The FIR response of the two electron systems as a function of the external magnetic field may be difficult to obtain experimentally. These results are arguably the most interesting due to the correlations between the structure of the splitting and the changes in the ground state quantum numbers. Potential

experimental difficulties arise because the relatively large confining magnetic fields used to obtain the theoretical results are currently unattainable. Such large confining magnetic fields were chosen primarily to ease computation of the results. For example, the results shown in figure 5.5 are calculated with $r_o = 100$ nm and $B_z = 1$ T. With these parameters the system is stable even in the absence of the external magnetic field. If the confining magnetic field is decreased, the magnetic quantum dot radius at which the system becomes stable increases. Therefore more Landau levels must be included in the numerical diagonalisation calculation to obtain converged energy eigenvalues, and hence the computational time required to obtain the results increases. However, it is seen that both figure 5.5 and figure 5.6 show results of a similar trend, with a splitting of the upper branch, and it is likely that this trend will continue as the confining magnetic field is decreased to experimentally attainable values. Therefore the splitting of the upper branch predicted in these figures, which is the order of 1 meV for low external magnetic fields, should exist for $B_z = 0.5$ T, and hence should be experimentally detectable with current technology.

Chapter 6

Summary and Conclusions

The analysis that has been undertaken during the course of this work has led to much interesting and novel physics, and many new discoveries have been made. The properties of the magnetic quantum dot have been investigated with numerical and semi-analytic techniques such as exact numerical diagonalisation and wave function matching. These have enabled the single electron system, which forms the majority of the existing work in this field, to be examined thoroughly. Using new methods devised in this work, it is now possible to apply the wave function matching technique successfully to this system when it has a magnetic field overshoot. However, the primary focus of this thesis is concerned with understanding the physics of the many electron system. This system has not been subject to previous investigation. It has been shown in this thesis that the electron-electron interaction strongly affects the electronic and optical properties of the magnetic quantum dot. This is primarily due to the unusual form of the confinement in this system, and many of the results presented in chapter 4 and chapter 5 follow from this. It is believed that the work contained in these chapters, and indeed the whole of this thesis, will serve as a basis for any future work in this field.

The initial part of this thesis has been concerned with formulating a theoretical model of the magnetic quantum dot. This model provides an accurate, yet simple, description of the magnetic quantum dot, and one of the reasons for this is that it is independent of the z coordinate. This theoretical model is formulated in chapter 2 following an investigation of how the various magnetic field profiles associated with the magnetic quantum dot arise. Much of this work is a continuation from the work of Peeters *et al* [9]. This model of the magnetic quantum dot has been used in all subsequent chapters, and in chapter 3 has been used to investigate the electronic properties of a magnetic quantum dot containing a single electron. This system has been investigated using exact numerical diagonalisation and the wave function matching technique to obtain the eigenstates and energy eigenvalues. The main development in chapter 3 has been the application of the wave function matching technique to the system with a magnetic field overshoot. During this work several analytic and numerical problems have been overcome. By evaluating the ratio of the hypergeometric functions rather than the divergent individual hypergeometric functions, the energy of this system has been calculated for the first time using the wave function matching method. The ratio, R, has been evaluated by solving a first order differential equation which has the form of a Riccati equation. Depending on the magnitude of R, a differential equation for R or $1/R$ is solved. This is because numerical problems due to singularities in R are encountered. This work is an important extension to the existing work in this field, and completes the work on the single electron system. It is believed that the advantages of using this method, namely computational ease, make it worthwhile, and outweigh any disadvantages arising from its complexity.

The plots showing the single electron energy as a function of the angular

momentum quantum number presented in chapter 3 for the system without the magnetic overshoot are mainly intuitive. One would expect the energy of an electron to increase and then become constant as the angular momentum quantum number increased. However, the results obtained for the system with a magnetic field overshoot can not be explained in such simple terms. It is difficult to imagine how the peak in the energy versus angular momentum quantum number arises. Although Peeters *et al* [9] obtain similar results, they fail to give a satisfactory explanation for this phenomenon. In this work this effect has been analysed in terms of the effective potential. This analysis results in a simple, comprehensible explanation that is supported with results for the electron density.

The second method used to investigate the single electron system is exact numerical diagonalisation. This method has been shown to be a very efficient way of obtaining results. However, it is believed that the wave function matching technique is more suited to the single electron system due to the greater programming effort required to write the numerical diagonalisation routine. The advantage of the numerical diagonalisation method is that it is readily adapted to include more electrons. A fact which has been exploited in chapter 4 and chapter 5. In chapter 4 the electronic properties of the magnetic quantum dot containing interacting electrons have been investigated. In order to calculate the results presented in chapter 4, new methods to evaluate the Coulomb matrix elements have been devised. These new methods are required because of the roundoff errors which arise on attempting to calculate the matrix elements with large quantum numbers. These errors accumulate due to the cancellation of successive terms with alternating sign, and can swamp the desired result. The new methods that have been devised, while being more numerically stable, are

also more CPU intensive. Therefore, the fastest routine that is stable is used to evaluate the Coulomb matrix elements. The main emphasis of the work contained in chapter 4 follows from the fact that the magnetic quantum dot is able to confine interacting electrons, and this is one of the main conclusions resulting from this thesis. From this follows the concept of stability, which is paramount in all of the subsequent work. Stability diagrams for a particular system, provide a way of depicting whether a system is stable or unstable as a function of the system parameters. The analytical form of the stability curves have been determined from a dimensional analysis of the hamiltonians. This enables the position of the stability boundary to be predicted to a reasonable accuracy. This stability condition has been used in chapter 4 to explain why various systems are stable or unstable, and these predictions are supported and verified with numerical values for the energies of the stable and unstable systems.

The effect of the material parameters on the stability has been investigated. The main conclusion resulting from this work is that the InSb system is more stable than the equivalent GaAs system. The reason for this is mainly due to the smaller effective mass in the InSb system, and this result can be obtained quite simply from the stability condition. Other systems have also been investigated in chapter 4. Arguably, some of the more interesting results are obtained when a homogeneous external magnetic field is applied to the system. The introduction of another magnetic field to the system enables several possible forms for the single particle basis function. However, with a convergence analysis, the optimum basis function has been determined. This system has been shown to have enhanced stability, and this is due to the energy of the electrons inside the magnetic quantum dot being decreased. This fact is supported with numerical values for

the energy and also by the analytic stability condition. The stability of a realistic system with a 2DEG of finite thickness has been investigated. The Fang-Howard states are used to describe the motion of the electrons in the z direction, and the variational parameter has been calculated explicitly. To determine this a simple approximation has been introduced, and it is shown that the form factor results in a modified Coulomb energy that is roughly constant as a function of this variational parameter. This proves to be a crucial result as it enables the variational parameter to be evaluated quite simply. The stability of this system has been shown to be enhanced. This result is intuitive and is a direct consequence of the extra separation of the electrons, resulting in the energy of the electrons decreasing. The work that concludes chapter 4 is the investigation of a magnetic quantum dot containing three interacting electrons. This work is very important as it shows that more electrons can be confined in the magnetic quantum dot. In order to confine three electrons it has been shown that the radius and the confining magnetic field of the dot are required to be greater than those of the equivalent two electron system. This is a consequence of the greater Coulomb energy in the three electron system. Many of the results in chapter 4 are supported with plots of the electron density, pair distribution and pair correlation functions. These provide a more pictorial explanation of the differences in stability, and clarify the electron positions and separations within the various systems.

The treatment of an experimentally realisable system is crucial if reliable comparisons with experiments are to be made. In chapter 5, the FIR response of several experimentally realisable magnetic quantum dot systems has been investigated. The intensity of a particular transition has been calculated from the dipole matrix elements between a numerically calculated ground state and

all the excited states. The final states have been determined using the selection rules, which follow from the dipole matrix element calculation. In chapter 5 the FIR response of GaAs and InSb magnetic quantum dots containing one and two electrons as a function of the confining magnetic field and an external magnetic field has been investigated. It has been shown that Kohn's theorem is violated, and this is found to be a consequence of coupling between the centre of mass and relative motion of the electrons. The importance of this result can not be overstated. Because Kohn's theorem is violated, the effect of electron-electron interactions in this system can be probed by optical experiments. The FIR response of a GaAs system containing two interacting electrons has been shown to be markedly different to that of the equivalent InSb system. A large splitting in the upper branch of the FIR response of the InSb system has been predicted. A possible explanation for this interesting result is offered. It has been conjectured that the effect is due to a combination of the ground state angular momentum quantum number value and the coupling of the centre of mass and relative motion states of the electrons. The FIR response as a function of the external magnetic field provides more insight into these novel systems. The single electron results have shown that the response is very similar to that of the electrostatic quantum dot. However, it is the results for the two electron systems that are most interesting. Both the GaAs and InSb systems show similar features. For low external magnetic fields a splitting of 1 meV is predicted in the upper branches. This splitting has been explained in terms of the coupling of the centre of mass and relative motion states of the electrons. The magnitude and structure of this splitting has been shown to be directly correlated to changes in the ground state angular momentum quantum number.

6.1 Future Work

In spite of the numerical diagonalisation program being an efficient method to obtain the quantum states of a magnetic quantum dot, several limitations of the current method should be pointed out. The technique is best when used to calculate the states of a system with a small magnetic quantum dot radius, containing one or two electrons. Deviations from these ideal conditions result in calculations that become increasingly difficult to perform. Additionally, if many Landau levels are included in a calculation, this problem is compounded by the fact that two of the routines to evaluate the Coulomb matrix elements are significantly more computationally expensive than the original routine. It should be possible to ease these problems by making several modifications to the current program. Because, in many calculations, the majority of the CPU time is spent calculating the Coulomb matrix elements, modifications to these routines seem the obvious choice. During the course of this work great effort has been taken to ensure that highly efficient algorithms have been devised, and it is thought that improving the efficiency would prove difficult. Nevertheless, if more efficient versions of these algorithms could be constructed, the CPU time should decrease dramatically, thus allowing larger scale calculations to be performed. A further option could be to attempt to use the correct single particle eigenstates of a magnetic quantum dot to represent the single particle functions. This should increase the accuracy of the results, thus enabling less basis states to be included in a calculation, although it is expected that many analytic and numerical difficulties would be encountered if this was attempted. The investigation of systems containing more than three electrons may prove difficult. In this regime the size of the hamiltonian matrix becomes the dominant problem. However,

this problem may be relieved somewhat by storing only non-zero elements of the matrix to save computer memory. Additionally, using an iterative method to determine only a few low-lying eigenstates of the matrix, such as the Lanczos method [25], instead of the whole spectrum would also improve computational time and save on memory usage. Therefore, in principle, the limitations of the current program could be largely removed, resulting in a much wider range of applications.

With these modifications, it is possible that much more fascinating physics may be discovered. For example, the investigation of systems with more electrons could potentially lead to more novel effects. It is predicted that with more interacting electrons, the system would require an ever increasing confining magnetic field, or magnetic quantum dot radius to confine the electrons in the magnetic quantum dot region. Whether a stability boundary is a generic characteristic of a magnetic quantum dot system remains an open question, and studies of a system with more than three interacting electrons could go some way to addressing this. Possible experimental studies include transport spectroscopy, electron capacitance spectroscopy and the investigation of laterally and vertically coupled magnetic quantum dots. All of these aspects have been studied experimentally and theoretically for the case of the electrostatic quantum dot [51, 55, 60, 61, 62, 63, 64, 65, 66, 67, 68, 69, 70], and they have already yielded many fascinating results. Perhaps similar novel physics exists for the case of the magnetic quantum dot.

APPENDIX A

Calculation of the Coulomb Matrix Elements

To perform the exact numerical diagonalisation calculation described in chapter 2, the Coulomb matrix elements must be evaluated. In this appendix three ways of evaluating the Coulomb matrix elements are given. The underlying method by which the Coulomb matrix elements are calculated is the same for each each of the three ways, and involves taking the Fourier transform of the interaction potential, $1/|\mathbf{r}|$.

Explicitly the Coulomb matrix element, which is present in Eq. 2.10 is given by

$$\langle ij|v|kl\rangle = \frac{e^2}{4\pi\epsilon\epsilon_o}\int \psi_i^*(\mathbf{r}_1)\psi_j^*(\mathbf{r}_2)\frac{1}{|\mathbf{r}_1-\mathbf{r}_2|}\psi_k(\mathbf{r}_2)\psi_l(\mathbf{r}_1)d\mathbf{r}_1 d\mathbf{r}_2 d\phi_1 d\phi_2, \qquad \text{(A.1)}$$

where $\psi_i(\mathbf{r})$ are the Fock-Darwin states, and these are given by Eq. 2.13. To proceed, the Fourier transform of $1/|\mathbf{r}|$ is taken, giving

$$\frac{1}{|\mathbf{r}_1-\mathbf{r}_2|} = \frac{1}{2\pi}\int \frac{e^{i\mathbf{q}\cdot(\mathbf{r}_1-\mathbf{r}_2)}}{|\mathbf{q}|}d\mathbf{q}. \qquad \text{(A.2)}$$

The exponential term in this equation can be expressed in scalar form as $e^{iqr_1\cos\phi_1}e^{-iqr_2\cos\phi_2}$, hence after substituting Eq. A.2 and Eq. 2.13 into Eq. A.1, the ϕ integrals take the form

$$\mathcal{I} = \int_0^{2\pi}\int_0^{2\pi} e^{iqr_1\cos\phi_1}e^{i(l_i-l_l)\phi_1}e^{-iqr_2\cos\phi_2}e^{i(l_j-l_k)\phi_2}d\phi_1 d\phi_2. \qquad \text{(A.3)}$$

Using the relation

$$e^{iqr\cos\phi} = \sum_{\lambda=-\infty}^{\infty} J_\lambda(qr) i^\lambda e^{i\lambda\phi}, \tag{A.4}$$

where $J_\lambda(qr)$ is a Bessel function of order λ, the integrals over ϕ given by Eq. A.3 reduce to the following

$$\mathcal{I} = 4\pi^2 J_{l_l - l_i}(qr_1) J_{l_k - l_j}(-qr_2) i^{l_l - l_i + l_k - l_j}. \tag{A.5}$$

Due to the conservation of angular momentum $l_i + l_j = l_k + l_l$, and therefore $i^{l_l - l_i + l_k - l_j} = 1$. Using the identity, $J_{-n}(-x) = J_n(x)$ [29], the Bessel function with the negative argument in Eq. A.5 reduces to $J_\lambda(qr_2)$, where $\lambda = l_l - l_i = l_j - l_k$. Substituting $\mathcal{I}$ back into Eq. A.1 and introducing the dimensionless variable $x^2 = r^2/2l_B^2$ gives

$$\begin{aligned}
\langle ij|v|kl\rangle &= \frac{(4e\pi l_B^2)^2}{4\pi\epsilon\epsilon_o} N_{n_i l_i} N_{n_j l_j} N_{n_k l_k} N_{n_l l_l} \int_0^\infty dq \\
&\times \int_0^\infty x_1^{|l_i|+|l_l|+1} e^{-x_1^2} L_{n_i}^{|l_i|}(x_1^2) L_{n_l}^{|l_l|}(x_1^2) J_\lambda(\sqrt{2}qx_1) dx_1 \\
&\times \int_0^\infty x_2^{|l_j|+|l_k|+1} e^{-x_2^2} L_{n_j}^{|l_j|}(x_2^2) L_{n_k}^{|l_k|}(x_2^2) J_\lambda(\sqrt{2}qx_2) dx_2.
\end{aligned} \tag{A.6}$$

This equation is the result given in chapter 3 by Eq. 4.6 and is also the common starting point used in the other two methods to derive the Coulomb matrix elements.

The first of the other methods follows from the work of Maksym [24] and involves writing the associated Laguerre polynomials in Eq. A.6 as a power series, thus giving

$$L_{n_i}^{|l_i|}(x^2) = \sum_{\alpha=0}^{n_i} (-1)^\alpha \binom{n_i + |l_i|}{n_i - \alpha} \frac{x^{2\alpha}}{\alpha!}. \tag{A.7}$$

Substituting this form for the associated Laguerre polynomials in Eq. A.6, allows the integrals over x_1 and x_2 to be evaluated [58]. Therefore the final result for

the Coulomb matrix element is found to be

$$\begin{aligned}\langle ij|v|kl\rangle &= \frac{(2e\pi l_B^2)^2}{4\pi\epsilon\epsilon_o} N_{n_i l_i} N_{n_j l_j} N_{n_k l_k} N_{n_l l_l} \sum_{\alpha=0}^{n_i}\sum_{\beta=0}^{n_l}\sum_{\gamma=0}^{n_j}\sum_{\delta=0}^{n_k} \frac{(-1)^{\alpha+\beta+\gamma+\delta}}{\alpha!\beta!\gamma!\delta!} \\ &\times \binom{n_i+|l_i|}{n_i-\alpha}\binom{n_l+|l_l|}{n_l-\beta}\binom{n_j+|l_j|}{n_j-\gamma}\binom{n_k+|l_k|}{n_k-\delta} A!B! \\ &\times \int_0^\infty e^{-q^2 l_B^2}\left(\frac{q^2 l_B^2}{2}\right)^{|\lambda|} L_A^{|\lambda|}\left(\frac{q^2 l_B^2}{2}\right) L_B^{|\lambda|}\left(\frac{q^2 l_B^2}{2}\right) dq, \end{aligned} \tag{A.8}$$

where

$$A = \left(\alpha+\beta+\frac{1}{2}\left[|l_i|+|l_l|-|\lambda|\right]\right) \tag{A.9}$$

and

$$B = \left(\gamma+\delta+\frac{1}{2}\left[|l_j|+|l_k|-|\lambda|\right]\right), \tag{A.10}$$

and this is the result in chapter 3 given by Eq. 4.2.

A further method to evaluate the Coulomb matrix elements is also due to Maksym [24]. Again, Eq. A.6 is the starting point. Rewriting the x integrals in Eq. A.6 in terms of three associated Laguerre polynomials. To begin, the Bessel functions in Eq. A.6 are substituted with the following expression obtained from Magnus *et al* [26]

$$J_\lambda(2\sqrt{qx}) = e^{-q}(xq)^{\frac{\lambda}{2}} \sum_{n=0}^{\infty} \frac{L_n^\lambda(x) q^n}{(n+\lambda)!}. \tag{A.11}$$

The integral over x_1 then takes the form

$$\frac{q^\lambda e^{-q^2}}{2} \sum_{n=0}^{\infty} \frac{q^{2n}}{(n+\lambda)!} \int_0^\infty dx_1 e^{-x_1} x_1^{(|l_i|+|l_l|+\lambda)/2} L_{n_i}^{|l_i|}(x_1) L_{n_l}^{|l_l|}(x_1) L_n^\lambda(x_1), \tag{A.12}$$

where a change of variable from x_1^2 to x_1 has been made. A similar expression to this is also obtained for the integral over x_2. Introducing the constant $s = (|l_i| + |l_l| - \lambda)/2$, it is seen that $x^s L_{n_i}^{|l_i|}(x_1) L_{n_l}^{|l_l|}(x_1)$ is a polynomial of order $s + n_i + n_l$, and therefore must have an expansion of the form

$$\sum_{m=0}^{s+n_i+n_l} a_m L_m^k(x_1). \tag{A.13}$$

Substituting this expression along with $s = (|l_i| + |l_l| - \lambda)/2$ into Eq. A.12, results in the orthogonality integral for the associated Laguerre polynomial, and hence the integral over x_1 is found to take the form

$$\frac{q^\lambda e^{-q^2}}{2} \sum_{m=0}^{s+n_i+n_l} \frac{a_m q^{2m}}{m!}. \tag{A.14}$$

The a_m in this expression are obtained from Eq. A.13, and using the orthogonality condition for the associated Laguerre polynomial they are found to be

$$a_m = \frac{m!}{(m+\lambda)!} \int_0^\infty dx_1 e^{-x_1} x_1^{s+\lambda} L_m^\lambda(x_1) L_{n_i}^{|l_i|}(x_1) L_{n_l}^{|l_l|}(x_1). \tag{A.15}$$

Therefore substituting this into Eq. A.14 it is found that an expression similar to Eq. A.12 is obtained, except the sum over n is restricted. By repeating this procedure for the integral over x_2, the final form for the Coulomb matrix element is found to be

$$\begin{aligned} \langle ij|v|kl\rangle &= \frac{(2e\pi l_B^2)^2}{4\pi\epsilon\epsilon_o} N_{n_i l_i} N_{n_j l_j} N_{n_k l_k} N_{n_l l_l} \int_0^\infty dq\, q^{2\lambda} e^{-2q^2} \\ &\times \int_0^\infty dx_1 e^{-x_1} x_1^{s+\lambda} L_{n_i}^{|l_i|}(x_1) L_{n_l}^{|l_l|}(x_1) \sum_{m=0}^{s+n_i+n_l} \frac{q^{2m} L_m^\lambda(x_1)}{(m+\lambda)!} \\ &\times \int_0^\infty dx_2 e^{-x_2} x_2^{t+\lambda} L_{n_j}^{|l_j|}(x_2) L_{n_k}^{|l_k|}(x_2) \sum_{p=0}^{t+n_j+n_k} \frac{q^{2p} L_p^\lambda(x_2)}{(p+\lambda)!}, \end{aligned} \tag{A.16}$$

and this is the result given in chapter 3 by Eq. 4.5.

Bibliography

[1] F. M. Peeters, *Physics World* (October 1995) 24.

[2] L. Landau, *Z. Phys* **64** (1930) 629.

[3] H. A. Carmona, A. K. Geim, A. Nogaret, T. J. Foster, P. C. Main, S. P. Beaumont and M. G. Blamire, *Phys. Rev. Lett.* **74** (1995) 3009.

[4] R. Yagi and Y. Iye, *J. Phys. Soc. Japan* **62** (1993) 1279.

[5] S. Izawa, S. Katsumoto, A. Endo and Y. Iye, *J. Phys. Soc. Japan* **64** (1995) 706.

[6] P. D. Ye, D. Weiss, R. R. Gerhardts, M. Seeger, K. von Klitzing, K. Eberl and H. Nichel, *Phys. Rev. Lett.* **74** (1995) 3013.

[7] L. Solimany and B. Kramer, *Solid State Comm.* **96** (1995) 471.

[8] I. S. Ibrahim and F. M. Peeters, *Phys. Rev. B* **52** (1995) 17321.

[9] F. M. Peeters, A. Matulis and I. S. Ibrahim, *Physica B* **227** (1996) 131.

[10] J. Reijniers, F. M. Peeters and A. Matulis, *Phys. Rev. B* **59** (1999) 2817.

[11] Heung-Sun Sim, K. -H. Ahn, K. J. Chang, G. Ihm, N. Kim and S. J. Lee, *Phys. Rev. Lett.* **80** (1998) 1501.

[12] C. S. Kim and O. Olendski, *Phys. Rev. B* **53** (1996) 12917.

[13] P. A. Maksym and T. Chakraborty, *Phys. Rev. Lett.* **45** (1992) 1947.

[14] P. A. Maksym and T. Chakraborty, *Phys. Rev. Lett.* **65** (1990) 108.

[15] L. E. Schiff, "*Quantum Mechanics*" (McGraw-Hill, New York 1955).

[16] F. M. Peeters and P. Vasilopoulos, *Phys. Rev. B* **47** (1993) 1466.

[17] D. Weiss, K. von Klitzing, K. Ploog and G. Weiman, *Europhys. Lett.* **8** (1989) 179.

[18] V. Kubrak, F. Rahman, N. Overend, B. L. Gallagher, P. C. Main, J. DeBoeck, M. Behest, C. H. Marrows and M. A. Howson, *Physica B* **258** (1998) 380.

[19] N. Overend, A. Nogaret, B. L. Gallagher, P. C. Main, M. Henini, C. H. Marrows, M. A. Howson, S. P. Beaumont, *Appl. Phys. Lett.* **72** (1998) 1724.

[20] F. M. Peeters and A. Matulis, *Phys. Rev. B* **48** (1993) 15166.

[21] J. H. Davies and I. A. Larkin, *Phys. Rev. B* **49** (1994) 4800.

[22] V. Fock, *Z. Phys.* **47** (1928) 446.

[23] C. G. Darwin, *Proc. Camb. Philos. Soc.* **27** (1930) 86.

[24] P. A. Maksym, Private communication.

[25] W. H. Press, B. P. Flannery, S. A. Teukolsky and W. T. Vetterling, "*Numerical Recipes, The Art of Scientific Computing*" (Cambridge University Press, 1989).

[26] W. Magnus, F. Oberhettinger and R. P. Soni, "*Formulas and Theorems for the Special functions of Mathematical Physics*" (Springer-Verlag, Berlin · Heidelberg, 1966).

[27] P. A. Maksym, *Physica B* **184** (1993) 385.

[28] Y. L. Luke, "*The Special Functions and their Approximations*" (Academic Press, New York and London, 1969).

[29] M. Abramowitz and I. A. Stegun, "*Handbook of Mathematical Functions*" (Dover Publications, Inc. 1965).

[30] E. L. Ince, "*Ordinary Differential Equations*" (Longmans, Green and Co. Ltd. 1927).

[31] G. W. Bryant, *Phys. Rev. Lett.* **59** (1987) 1140.

[32] E. P. Wigner, *Phys. Rev.* **46** (1934) 1002.

[33] D. Pfannkuche, R. R. Gerhardts, P. A. Maksym and V. Gudmundsson, *Physica B* **189** (1993) 6.

[34] M. Wagner, U. Merkt and A. V. Chaplik, *Phys. Rev. B* **45** (1992) 1951.

[35] N. A. Bruce and P. A. Maksym, submitted to *Phys. Rev. B.*

[36] T. Chakraborty, "*Quantum Dots: A survey of the Properties of Artificial Atoms*", to be published.

[37] S. M. Girvin and T. Jach, *Phys. Rev. B* **28** (1983) 4506.

[38] M. Stone, H. W. Wyld and R. L. Schult, *Phys. Rev. B* **45** (1992) 14156.

[39] D. Heitmann and J. P. Kotthaus, *Physics Today* **46** (1993) 56.

[40] P. A. Maksym, *Phys. Rev. B* **53** (1996) 10871.

[41] G. Appold, H. Pascher, R. Ebert, U. Steigenberger and M. von Ortenberg, *Phys. Stat. Sol. B* **86** (1978) 557.

[42] F. F. Fang and W. E. Howard, *Phys. Rev. Lett.* **16** (1966) 797.

[43] T. Ando, A. B. Fowler and F. Stern, *Rev. Mod. Phys.* **54** No 2 (1982) 437.

[44] J. H. Davies, "*The Physics of Low-Dimensional Semiconductors, an Introduction*" (Cambridge University Press, 1998).

[45] L. Brey, N. F. Johnson and B. I. Halperin, *Phys. Rev. B* **40** (1989) 10647.

[46] L. D. Hallam, J. Weis and P. A. Maksym, *Phys. Rev. B* **53** (1996) 1452.

[47] V. Kubrak, Private communication.

[48] Ch. Sikorski and U. Merkt, *Phys. Rev. Lett.* **62** (1989) 2164.

[49] T. Demel, D. Heitmann, P. Grambow and K. Ploog, *Phys. Rev. Lett.* **64** (1990) 788.

[50] C. T. Liu, K. Nakamura, D. C. Tsui, K. Ismail, D. A. Antoniadis and H. I. Smith, *Appl. Phys. Lett.* **55** (1989) 168.

[51] T. Chakraborty, V. Halonen and P. Pietiläinen, *Phys. Rev. B* **43** (1991) 14289.

[52] D. Pfannkuche and R. R. Gerhardts, *Phys. Rev. B* **44** (1991) 13132.

[53] L. Jacak, J. Krasnyj and A. Wójs, *Physica B* **229** (1997) 279.

[54] W. Kohn, *Phys. Rev.* **123** (1961) 1242.

[55] H. Imamura, P. A. Maksym and H. Aoki, *Phys. Rev. B* **59** (1999) 5817.

[56] H. A. Bethe and E. E. Salpeter, "*Quantum Mechanics of One- and Two-electron atoms*" (Plenum, 1977).

[57] R. B. Dingle, *Proc. R. Soc.* A **211** (1952) 38.

[58] I. S. Gradshteyn and I. M. Ryzhik, "*Table of Integrals, Series and Products*" (Academic Press, New York and London, 1965).

[59] P. A. Maksym, *32nd Winter School of Theoretical Physics* (Karpacz, 1996).

[60] B. J. van Wees, L. P. Kouwenhoven, C. J. P. M. Harmans, J. G. Williamson, C. E. Timmering, M. E. I. Broekaart, C. T. Foxton and J. J. Harris, *Phys. Rev. Lett.* **62** (1989) 2523.

[61] P. L. McEuen, E. B. Foxman, U. Meirav, M. A. Kastner, Y. Meir, N. S. Wingreen and S. J. Wind, *Phys. Rev. Lett.* **66** (1991) 1926.

[62] P. L. McEuen, E. B. Foxman, J. Kinaret, U. Meirav, M. A. Kastner, N. S. Wingreen and S. J. Wind, *Phys. Rev. B* **45** (1992) 11419.

[63] A. T. Johnson, L. P. Kouwenhoven, W. de Jong, N. C. van der Vaart, C. J. P. M. Harmans and C. T. Foxon, *Phys. Rev. Lett.* **69** (1992) 1592.

[64] E. B. Foxman, P. L. McEuen, U. Meirav, N. S. Wingreen, Y. Meir, P. A. Belk, N. R. Belk, M. A. Kastner and S. J. Wind, *Phys. Rev. B* **47** (1993) 10020.

[65] K. Von Klitzing, *Physica Scripta* **T68** (1996) 21.

[66] Y. Hirayama and T. Saku, *Solid State Comm.* **73** (1990) 113.

[67] J. Weis, R. J. Haug, K. von Klitzing and K. Ploog, *Phys. Rev. Lett.* **71** (1993) 4019.

[68] R. C. Ashoori, H. L. Stormer, J. S. Weiner, L. N. Pfeiffer, K. W. Baldwin and K. W. West, *Phys. Rev. Lett.* **71** (1993) 613.

[69] R. C. Ashoori, H. L. Stormer, J. S. Weiner, L. N. Pfeiffer, S. J. Pearton, K. W. Baldwin and K. W. West, *Phys. Rev. Lett.* **68** (1992) 3088.

[70] R. C. Ashoori, *Nature* **379** (1995) 413.